Alma Mater Studiorum · Università di Bologna

**Scuola di Scienze**
**Corso di Laurea Magistrale in Fisica del Sistema Terra**

# Surface cloud radiative forcing from broadband radiation measurements on the Antarctic Plateau

**Relatore:**
**Prof. Tiziano Maestri**

**Presentata da:**
**Enrica Spadanuda**

**Correlatore:**
**Dott. Angelo Lupi**
**Dott. Maurizio Busetto**

**Sessione III**
**Anno Accademico 2014/2015**

*A*
*Sari, Chiara,*
*Lolly, Frenci, SaraP*

# Abstract

Surface based measurements systems play a key role in defining the ground truth for climate modeling and satellite product validation. The Italian-French station of Concordia is operative year round since 2005 at Dome C (75S, 123E, 3230 m) on the East Antarctic Plateau.

A Baseline Surface Radiation Network (BSRN) site was deployed and became operational since January 2006 to measure downwelling components of the radiation budget, and successively was expanded in April 2007 to measure upwelling radiation. Hence, almost a decade of measurement is now available and suitable to define a statistically significant climatology for the radiation budget of Concordia including eventual trends, by specifically assessing the effects of clouds and water vapor on SW and LW net radiation.

A well known and robust clear sky-id algorithm (Long and Ackerman, 2000) has been operationally applied on downwelling SW components to identify cloud free events and to fit a parametric equation to determine clear-sky reference along the Antarctic daylight periods (September to April).

A new model for surface broadband albedo has been developed in order to better describe the features the area.

A clear-sky LW parametrization, based on a-priori assumption about inversion layer structure, combined with daily and annual oscillations of the surface temperature, has been adopted and validated. The LW based method is successively exploited to extend cloud radiative forcing studies to nighttime period (winter).

Results indicated inter-annual and intra-annual warming behaviour, i.e. 13.70

$\pm$ 2.90 W/m$^2$ on the average, specifically approaching neutral effect in summer, when SW CRF compensates LW CRF, and warming along the rest of the year due prevalentely to CRF induced on the LW component.

# Contents

# List of Figures

# List of Tables

# Introduction

The radiation budget of the Earth-atmosphere system is considered to play a fundamental role in determining the thermal condition and the circulation of the atmosphere and the ocean, shaping the main characteristics of the Earth's climate. The irradiances at the Earth's surface are important to understand climate processes, especially in the polar areas, where snow-covered surfaces, ice sheets and glaciers typically reflect 75%-95% of the incoming solar radiation, (Carroll and Fitch, 1981); on the other hand, the snow high longwave emissivity (around 0.98) leads iced surface to effectively loose heat in form of term radiation, and during most part of the year to a pronounced radiation deficit at the surface. Compensating for this heat loss is an average turbulent transport of sensible heat from the atmosphere to the surface.

This makes the Antarctic ice sheet a major heat sink in the Earth's atmosphere (the antarctica polar cap emits more energy to space in the form of infrared radiation than they absorb from sunlight) and introduces a strong coupling between the radiation balance and near-surface climate (Dutton et al., 1991; Stanhill and Cohen, 1997). Therefore, not only small changes in irradiance at the Earth's surface may cause a profound change in climate, but also the amount of absorbed shortwave radiation, being proportional to the albedo, is very sensitive to small changes; so the simulation of the past and future climate changes, which would be induced by the change in radiation, is even more uncertain.

Moreover, clouds participate in two competing manners in the surface radiation budget: warming the surface through the emission of longwave

radiation and cooling the surface by shading the incident shortwave radiation. Clouds are especially important in the Antarctic longwave budget because of the dryness of the Antarctic atmosphere, relative to lower latitudes, which produces relatively less clear-sky atmospheric emission. Due to temperature inversions, Antarctic clouds often emit at temperatures that are warmer than the underlying surface. The role of clouds in the Antarctic shortwave budget is variable over the annual cycle due to the long polar summer and winter and the highly reflective surface. The balance of these shortwave and longwave effects is referred to as cloud radiative forcing with positive values indicating that clouds warm the surface relative to clear skies, and negative values indicating that clouds cool the surface.

Despite Antarcticas importance to climate, it is still a relatively poorly characterized continent, particularly in the interior: the lack of measurements capable of arriving at the required accuracy for climate research, was the background for the World Climate Research Programme (WCRP) to propose since the 1988 and then initiate the Baseline Surface Radiation Network (BSRN) network to support the research projects of the WCRP and other scientific programs.

In order to reduce some of above listed uncertainties, BSRN provides different goals: 1) measures of earths surface irradiances for validating satellite-based estimates of the surface radiation budget and radiation transfer through the atmosphere, 2) measures of the irradiances to validate and improve radiation codes of climate models, and 3) to monitor long-term changes in irradiances at the earths surface.

Aim of this thesis is to provides estimates of some key parameters of the Antarctic atmosphere. Measurements of broadband, both shortwave and longwave downwelling/upwelling radiative fluxes made at the Dome C since 2007 are presented, together with accurate estimation of surface albedo values, cloud presence and cloud effects on radiation, to learn how changes in cloud and surface properties affect the surface radiative budget in the Antarctic.

The structure of this thesis is the following:

- chapter 1 gives an overview of the theoretical bases of the radiative transfer processes involved in the analysed phenomena;

- chapter 2 describes the measurement site, with a survey of meteorological condition that characterize this peculiar polar site. Moreover a picture of the dataset used in the frame of BSRN network is illustrated;

- chapter 3 is devoted to the analysis of shortwave measurements, and the illustration and implementation of a method in order to assess a cloudless-sky radiative empirical model, to recognize and discriminate cloud presence;

- chapter 4 is devoted to model the surface albedo through a fitting model, in order to evaluate the component of radiative balance in the shortwave region;

- chapter 5 is characterize by description of longwave measurements, both downwelling either upwelling, and method to i) estimate the cloud presence only with baseline broadband measurements and ii) evaluation of cloud effect on longwave balance;

- the final chapter illustrates all the total cloud radiative forcing, besides with some comparison with literature data.

# Chapter 1

# An introduction to cloud radiative forcing

Solar radiation is the main energy source for the Earth. Radiation entering the Earth's atmosphere is partly absorbed, partly scattered, and partly reflected by atmospheric gases, aerosols and clouds. The portion of radiation reaching the surface is absorbed and reflected by land and oceans. Since solar energy governs the radiative balance of the Earths atmosphere and surface, an accurate estimation of the incoming radiation is a key requirement for climate monitoring.

Clouds modify the global energy balance by altering the absorption and scattering characteristics of the atmosphere. The role of clouds in the energetics can be interpreted as a forcing in the radiative energy balance. For longwave radiation (LW), the large opacity of clouds increases the optical depth of the atmosphere, which promotes increased surface temperature by enhancing the greenhouse effect. Thus, clouds introduce warming in the LW energy budget. For the shortwave (SW) radiation, the high reflectivity of clouds decreases the incoming solar flux, which favors reduced surface temperature. Thus, clouds introduce cooling in the SW energy budget. Longwave emission is controlled by the cloud top temperature. Shortwave albedo of clouds is controlled by cloud thickness, droplet sizes and sun angle. The relative importance of the two competing effects of clouds depends on the circumstances: shortwave cooling is

dominant for clouds over the ocean (and dark surfaces), in daytime, in summer, and for low clouds. The longwave warming effect is dominant for clouds over snow (and other bright surfaces), at night, in winter, and for high clouds. The zenit angle dependence of scattering enhances albedo at high latitudes. Clouds also introduce heating by absorbing SW radiation.

A quantitative description of how clouds figure in the global energy budget is complicated by their dependence on microphysical properties and interactions with the surface. The bulk effect on the energy budget is given by the so called cloud radiative forcing (CRF) (Ramanathan et al., 1989; Shupe et al., 2004). It is defined as the difference between the net irradiance measured in cloudy sky conditions minus the net irradiance that would have been in clear sky conditions, namely:

$$CRF = F_{net} - F_{net}^{clear} \quad . \tag{1.1}$$

We can define the net irradiance using broadband radiation fluxes:

$$F_{net} = F_{net,SW} + F_{net,LW} = (F_{\downarrow,SW} - F_{\uparrow,SW}) + (F_{\downarrow,LW} - F_{\uparrow,LW}) \tag{1.2}$$

where $F_{\downarrow,SW}$, $F_{\uparrow,SW}$, $F_{\downarrow,LW}$ and $F_{\uparrow,LW}$ are respectively the shortwave downwelling and upwelling irradiances (i.e. visible wavelengths, from 0.3 $\mu$m - 3 $\mu$m), and the longwave downwelling and upwelling irradiances (i.e. infrared wavelengths, 4 $\mu$m - 50 $\mu$m).

Replacing equation 1.2 in 1.1, the CRF can be rewritten separating the cloud forcing on the different radiation components:

$$CRF = CF_{\downarrow,SW} - CF_{\uparrow,SW} + CF_{\downarrow,LW} - CF_{\uparrow,LW} \quad . \tag{1.3}$$

where $CF_{\downarrow,SW}$ is the cloud forcing on the shortwave downwelling irradiance and so on.

The forcing can be evaluated at the Earth surface or at the top of atmosphere (TOA). The first requires the knowledge of surface based radiation measurements, the second can be evaluated directly from broadband fluxes of outgoing LW and SW radiation measured by satellite.

The so defined CRF gives only the column-integrated effects of clouds, not providing information on the vertical distribution of the heating/cooling.

Generally, shortwave cloud forcing (which represents cooling) is concentrated near the surface, because the principal effect of increased albedo is to shield the ground from incident solar radiation. Longwave cloud forcing (which represents warming) is manifested heating near the base of a cloud and cooling near its top.

Clouds also introduce heating through the release of latent heat: this effect is of particular for tropical organized deep cumulunimbus clouds, which produce large volumes of precipitation, and thus latent heating contributions reach the radiative ones magnitude.

To better understand the effect of clouds on radiation we need to give a quantitative description of their interaction using radiative transfer equations.

## 1.1 Fundamentals of solar radiation

Radiation designates all the phenomena describing the transport of energy in space. It is characterized by a frequency, $\nu$, and a wavelength, $\lambda$. The electromagnetic spectrum is obtained by classifying radiation according to $\nu$ and $\lambda$. Consider the radiant energy $dE_\lambda$, in the wavelength interval between $\lambda$ and $\lambda + d\lambda$, that in the time interval dt crosses an element of area dA, in directions limited to the differential solid angle $d\Omega$, which is oriented to an angle $\theta$ with respect to the normal to dA. This energy is expressed in terms of the monochromatic intensity, or radiance $I_\lambda$:

$$dE_\lambda = I_\lambda cos\theta dA d\Omega d\lambda d\theta \quad . \tag{1.4}$$

Thus radiance is defined as follows:

$$I_\lambda = \frac{dE_\lambda}{cos\theta dA d\Omega d\lambda d\theta} \tag{1.5}$$

and is measured in $W/m^3sr$. The monochromatic irradiance is defined as the normal component of $I_\lambda$ integrated over the hemispheric solid angle:

$$F_\lambda = \int_\Omega I_\lambda cos\theta d\Omega = \int_0^{2\pi} \int_0^{\pi/2} I_\lambda(\theta, \phi) cos\theta sin\theta d\theta d\phi \tag{1.6}$$

For isotropic radiation $F_\lambda = \pi I_\lambda$. The total irradiance F is obtained by integrating the monochromatic irradiance over the eloctromagnetic spectrum:

$$F = \int_0^\infty F_\lambda d\lambda \tag{1.7}$$

and it is measured in $W/m^2$.

The solar constant $S_0$ is the total solar energy reaching the top of the atmosphere. It is defined as the energy per unit time which crosses a surface of unit area normal to the solar beam at the mean distance between the Sun and the Earth. The Sun emits an irradiance F of 6.2 $10^7$ $W/m^2$. If there is no medium between the Sun and the Earth, according to the principle of conservation of energy, the energy emitted from the Sun must remain constant at some distance away, thus also in correspondence of the atmosphere of the Earth:

$$F 4\pi a_s^2 = S_0 4\pi r^2 \tag{1.8}$$

where $a_s$ is the radius of the Sun and r is the mean Earth-Sun distance. Thus the solar constant can be expressed as:

$$S_0 = F\left(\frac{a_s}{r}\right)^2 \tag{1.9}$$

The accepted measured value for $S_0$ is 1366 $\pm$ 3 $W/m^2$. The solar constant is defined for a mean distance between the Earth and the Sun, $d_m$, that is 1.496 $10^{11}$ m, but the actual distribution of solar radiation at the top of the atmosphere depends on the eccentricity of the elliptical orbit of the Earth around the Sun. The point of maximum distance (1.521 $10^{11}$ m) is called aphelion and the Earth is in this position at the beginning of July. The point of minimum distance (1.471 10 11 m) is called perihelion, and corresponds to the beginning of January. The irradiance on an horizontal surface at the top of the atmosphere also depends on the sun zenith angle:

$$F_h = F cos\theta = S_0\left(\frac{d_m}{d}\right)^2 cos\theta \tag{1.10}$$

where F is the irradiance on a plane normal to the solar beam, $\theta$ is the latitude and d is the actual Earth-Sun distance. The $(d_m/d)^2$ term is the Sun-Earth distance

correction, that in the following will be designated with AU. It varies from values slightly lower than 1 to values slightly higher than 1 during the year.

Solar radiation entering the Earths atmosphere is absorbed and scattered by atmospheric gases, aerosols, clouds, and the Earths surface. Atmospheric scattering can be due to particles of different size, like gas molecules ($\sim 10^4$ $\mu$m), aerosols ($\sim$ 1 $\mu$m), water droplets ($\sim$ 10 $\mu$m), and rain drops ($\sim$ 1 cm). The effect of particle size on scattering is represented by the so called size parameter, x. For a spherical particle of radius a, x=$\frac{2\pi a}{\lambda}$. If x<<1 (particle small compared with the wavelength), the scattering is called Rayleigh scattering. An example is the scattering of visible light by atmospheric molecules. If x$\geq$1 (particle has about the same size as the wavelength) the scattering is called Lorenz-Mie scattering. If x>>1 (particle large compared with the wavelength) the scattering is called geometric scattering, and it can be studied by using the geometrical optics of reflection, refraction and diffraction. For low densities of molecules and particles in the air, the scattering is independent, i.e. each particle scatters radiation as if the other particles did not exist. If density increases, like happens inside clouds, each particle can scatter the radiation that has been already scattered by other particles. This process is called multiple scattering.

Absorption is the conversion of radiation in another form of energy, like heat. Absorption can be due to atmospheric molecules or aerosols. The UV radiation in the interval 0.2-0.3 $\mu$m is mainly absorbed by $O_3$ in the stratosphere. Radiation with $\lambda$ shorter than 0.2 $\mu$m is absorbed by $O_2$, $N_2$, O and N. In the troposphere, solar radiation is absorbed in the VIS and IR, mainly by $H_2O$, $CO_2$, $O_2$ and $O_3$.

Scattering and absorption are usually associated. Both processes remove energy from incident radiation, and this attenuation is called extinction.

The angular distribution of light intensity scattered at a given wavelength is called phase function, P. If $\Theta$ is the scattering angle, i.e. the angle between the incident and scattered waves, P is the ratio between the intensity scattered at the angle $\Theta$ and the total scattered intensity. P is defined so that its integral over the unit sphere centered on the scattering particle is $4\pi$:

$$\int_0^{2\pi} P(\Theta) sin\Theta d\Theta d\phi = 4\pi \tag{1.11}$$

### 1.1.1 Surface albedo

The ground albedo strongly depends on the nature of the surface, and on the spectral and angular distribution of the incoming radiation. The spectral albedo can be expressed as:

$$\alpha = \frac{F_{\uparrow,\lambda}}{F_{\downarrow,\lambda}} \tag{1.12}$$

where $F_{\uparrow,\lambda}$ is the reflected monochromatic irradiance and $F_{\downarrow,\lambda}$ is the incident one. Broadband albedo can be expressed as:

$$\alpha = \frac{F_{\uparrow}}{F_{\downarrow}} \tag{1.13}$$

where $F_{\uparrow}$ is the reflected radiative flux and $F_{\downarrow}$ the incident one.

Reflected light is generated through two processes: Fresnel reflection and scattering. Fresnel reflection describes the process happening between two uniform surfaces with different indexes of refraction. In this case the angle of reflection is equal to the angle of incidence. Diffuse radiation, in contrast, is generated by surface elements whose dimensions are of the same order of magnitude as the wavelengths of incident light. The intensity of the scattered light is only function of the scattering angle, $\Theta$. The distribution of the scattered light is specified in terms of a probability distribution function, which is called phase function and is indicated as $P(\Theta)$. $P(\Theta)\sin\Theta d\Theta/2$ represents the fraction of scattered radiation which has been scattered through an angle $\Theta$ into an incremental ring of solid angle $d\Omega=2\pi\sin\Theta d\Theta$. The Henyey-Greenstein phase function is an useful formulation for describing the angular distribution of anisotropic scattering:

$$P(g,\Theta) = \frac{1-g^2}{(1+g^2-2gcos\Theta)^{3/2}} \tag{1.14}$$

It uses the asymmetry parameter, g, which is an intensity-weighted average of the cosine of the scattering angle:

$$g = \frac{1}{2}\int_0^{\pi} cos\Theta P(\Theta) sin\Theta d\Theta \tag{1.15}$$

For g=0 the scattering is isotropic, for g<0 most of the radiation is scattered backward and for g>0 most of the radiation is scattered in the forward direction.

## 1.2 Radiative transfer in presence of clouds

The presence of liquid and solid particles greatly elongates the path traveled by the photons of SW radiation, which then undergo repeated reflection and diffraction. Along with absorption inside particles, this sharply increases the optical depth posed to incident radiation.

### 1.2.1 Rayleigh scattering

The simplest treatement of scattering describes the interaction of sunlight with molecules and is due to Rayleigh (1870): Rayleigh scattering considers a molecule exposed to electromagnetic radiation as an oscillating dipole, that, interacting with the wave's electromagnetic field, radiates a scattered wave. The scattered intensity is proportional to the magnitude of the electric field $\vec{E}$ of the scattered wave, that at large distances from the dipole behaves as a plane wave, and can be expressed as:

$$I(\Theta, r) = I_0 k^4 \frac{\alpha^2}{r^2} \frac{(1 + cos^2\Theta)}{2} \tag{1.16}$$

where $I_0$ is the intensity of the incident sunlight, $\Theta$ is the scattering direction, r is the distance from the radiating dipole, k is the wavenumber, $\alpha$ is the polarizability of the scatterer. In terms of wavelength $\lambda = \frac{2\pi}{k}$ and phase function:

$$P(\Theta) = \frac{3}{4}(1 + cos^2\Theta) \tag{1.17}$$

equation 1.16 can be rewritten as:

$$I(\Theta, r) = I_0 \frac{\alpha^2}{r^2} \frac{32\pi 4}{3\lambda^4} P(\Theta) \quad . \tag{1.18}$$

The scattered intensity has a maxima in the forward ($\Theta = 0^o$) and backward ($\Theta = 180^o$) directions, with equal energy directed into each halfspace.

We define the dimensionless refracting index, that is related to the polarizability $\alpha$, as:

$$m = m_r - m_i \tag{1.19}$$

where $m_r$ is the real refractive index, $m_i$ is the imaginary refractive index: the real part is related to the phase speed of the electromagnetic radiation in a medium

and the imaginary part to its absorption, relative to those in a vacuum. At visible wavelengths the absorption by air molecules is small enough for $m_i$ to be ignored, so the scattering cross section (i.e. the fraction of the scattered power over the incident flux) for an individual molecule is given by:

$$\hat{\sigma} = \frac{32\pi^3(m_r - 1)^2}{3n^2\lambda^4} \tag{1.20}$$

where n is the molecule number desity.

The $\lambda^4$ dependence shows how in clear sky the shorter wavelenghts are scattered more than the longer, so that the sky appears blue.

### 1.2.2 Mie scattering

Mie treatement of scattering (1908) applies to the interaction of radiation with aerosol and cloud droplets. The real refractive index for water $m_r(\lambda)$ is of the order of unity, but varies slightly with wavelengt; the imaginary refractive index $m_i(\lambda)$ is proportional to the absorption coefficient and is small in the visible, but increases sharply for $\lambda > 1$ $\mu$m, making clouds optically thick in the IR.

Mie scattering possesses much stronger directionality compared to the Rayleigh one. It exhibits strong forward scattering, expecially at shorter wavelenght, which are sharply peaked about $\Theta$=0 and for which absorption is small; a weaker maximum appears at backward scattering for wavelengths in the near-IR and visible regions.

The mean extinction cross section for the particle population is nearly constant across the visible, where cloud droplets are large, and the extinction is only due to scattering, that is wavelength independent: individual components of sunlight are then scattered with equal efficiency, so the cloud appears white. The extinction cross section attains a maximum near 5 $\mu$m, wavelength comparable to the mean radius of cloud droplets, and falls off at longer wavelengths. Scattering dominates over absorption at wavelengths of SW radiation. Exceptional are narrow bands at $\lambda \simeq$3 and 6 $\mu$m, where absorption spectra of water and ice are peaked.

Extinction by cloud droplets greatly increases the SW opacity of the atmosphere, even for shallow stratus. Scattering by nonspherical ice particles is

complicated by their irregular structure and anisotropy.

### 1.2.3 Radiative transfer in a cloudy atmosphere

Influences of cloud on atmospheric thermal structure can be evaluated with the radiative transfer equation, which general form, for monochromatic radiation of intensity $I_\lambda$ that crosses a layer of thickness ds and density $\rho$, is:

$$\frac{dI_\lambda}{\rho k_\lambda ds} = -I_\lambda + J_\lambda \tag{1.21}$$

where $J_\lambda$ is the source function, that describes the contribution of the emission of the layer to the resulting intensity. In absence of scattering, under local thermodynamic equilibrium conditions, the source function is given by the Planck function $B_\lambda(T)$. In presence of scattering, that cannot be neglected in presence of a clous, it becomes:

$$J(\phi,\mu,\tau) = \frac{\omega}{4\pi}\int_0^{2\pi}\int_{-1}^{1} I(\phi',\mu',\tau)P(\phi,\mu;\phi',\mu')d\phi' d\mu' + \frac{\omega}{4\pi}F_s P(\phi,\mu;\phi',-\mu_s)e^{-\frac{\tau}{\mu_s}} \tag{1.22}$$

where $\mu$=cos$\Theta$, $\phi$ is the azimuth, $\tau$ is the optical depth, $\omega$ is the single scattering albedo; the wavelength dependence is implicit and emission is ignored. The fist term on the right-hand side represents the contributions to diffuse radiation from multiple scattering of the diffuse intensity I, whereas the second term represents the contribution from single scattering of direct solar radiation $I_s$.

Radiative transfer equation becomes much more complicated in presence of scattering. For a detailed treatement see Salby (1995).

The obtained solution for scattered irradiance can be used to evaluate the cloud albedo and trasmissivity in presence of a cloud. At visible wavelengths, cloud albedo increases sharply at small optical depth and reaches a constant value of 0.8 for high optical depth; even shallow stratus are highly reflective. Transmissivity presents an opposite trend, i.e. it decreases with increasing $\tau_c$. The two quantities are nearly complementar, so that most of the incident SW is reflected or transmitted, and only a 10% is absorbed. Moreover, $\alpha_c$ increases with increasing solar zenith angle, as it elongates the slant optical path; the

opposite trend is observed for $t_c$. Shallower clouds depend even more strongly on solar zenith angle because the slant optical path then varies between optically thin and optically thick conditions.

Furthermore, for the same liquid water content, clouds with small droplets (i.e. continental clouds) have an higher albedo and smaller absorptivity than clouds with larger droplets, due to increased number densities; precipitation, on the other hand, sharply increases the absorptivity of clouds. Ice clouds are likewise highly reflective across the visible.

To understand the effect of clouds on longwave radiation we consider a simplified situation in which the monochromatic radiative flux (10 $\mu$m) interacts with an homogeneous optically thick scattering layer in radiative-convective equilibrium. First of all, an increase in surface temperature occurs. Under the cloud, there is a sharp change of downwelling and upwelling longwave radiative fluxes, both increasing from their clear-sky values. As the cloud is optically thick, in its interior the two fluxes undergo an adjustment that drives them nearly into coincidence. Changes in radiative fluxes also introduce strong warming and cooling in thin layers at the base and at the top of the cloud layer.

## 1.3 Clouds observations in Antarctica

In the Polar regions clouds act as a critical forcing factor on the radiation budgets at the top of the atmosphere and the surface. In the Antarctic, cloud observations have largely been confined to synoptic observations, although in recent years these measurements have been supplemented by occasional in situ microphysical measurements, mainly of low cloud from the surface, and radiometric measurements made from the surface and from satellite data. These measurements have only been made at a few locations and these locations may not be representative of the continent as a whole. It is not easy to model the relation between radiative balance at the surface to cloud properties. Thus, observational data are crucial, expecially in climatic areas where the sensitivity of the surface-atmosphere system to clouds is more pronounced, in order to

improve the parametrization schemes to be inserted in climatic models and test their results.

Several methods have been used to measure cloud cover in the Antarctic (ground-based visual observations, satellite measurements, active measurements such as LIDAR). These methods can give quite different results, and it can be difficult to establish the true value of the extent and frequency of cloud. Surface visual observations have been routinely made at Antarctic research stations for the last 50 years, and give the longest running cloud data set available (Hahn and Warren, 2003). However, the surface observing sites are widely spaced in Antarctica, and most are located close to the coast. Visual observations are subjective, and changes in observer can result in step changes in particular measurements. Also, visual observations during the night are difficult to make because of the low level of illumination of the clouds and this is particularly true of Antarctic clouds during the winter.

Surface radiation measurements can also be used to derive cloud cover. Town et al. (2007) compared fractional cloud cover from visual observations, satellite retrievals and surface-based infrared measurements at the South Pole. They suggested that the best measurements are those retrieved from surface-based pyrgeometer measurements, both in terms of accuracy and length of record, as they are not affected by the lack of sunlight. Town et al. (2007) compared surface visual observations with values retrieved from the pyrgeometer, and showed that during summer the two values agree well, whereas during winter the visual observations are around 20% lower. The pyrgeometer values suggest that the cloud cover at the South Pole is constant throughout the year, at around 50-60%.

Passive satellite instruments measure the upwelling radiation emitted from the surface or atmosphere, and measurements taken using such instruments have a much better spatial coverage. With passive measurements it can be difficult to distinguish between the clouds and the underlying snow surface, as the temperature and radiative properties of the cloud and snow surface are similar.

The best surface observations suggest that the fractional cloud cover at the

South Pole is around 50-60% in all seasons, whereas the cloud cover rises to around 80-90% close to the coast of the continent. For both ISCCP retrievals of cloud fraction and surface observations, it can be seen that cloud cover is at a minimum in the centre of the continent, and increases to a maximum close to the coast. Microphysical observations of cloud parameters are also very sparse in the Antarctic. However, the few measurements that do exist show predominantly ice-crystal clouds across the interior, with mixed-phase clouds close to the coasts. A wide range of crystal shapes is observed at all sites (Lachlan-Cope, 2010).

A predominance of thin clouds is on average observed on the Antarctic coast (Ricchiazzi et al., 1995), with larger crystals observed in summer than in winter, larger optical depths in summer than in winter and larger optical depths at the coast than in the interior; these results conform to expectations, because the atmosphere contains more water vapor at the coast than in the interior and more water vapor in summer than in winter. Also, are pointed out the large difficulties encoutered in measure surface albedo, which is strongly coupled with cloud effects over highly reflective surfaces because of multiple reflections between cloud base and the surface, and so presents high uncertainties.

Typical antarctic atmospheric phenomena comprehend blowing snow, i.e. snow particles lifted from the surface by the wind, diamond dust, i.e. small ice crystals forming in the persistent temperature inversion layer, particularly strong during winter, and snow grains, i.e. larger ice crystals falling from clouds, more common in the coastal region.

# Chapter 2

# Measurement site description

Dome C ($75^o06'00''$ S $123^o20'00''$ E) is on the Antarctic Plateau, 1220 km far from coast, and has an altitude of 3233 m a.s.l. At Dome C, since 2005, the third permanent station of the Antarctic Plateu, the italian-french station Concordia, has been operative also during Autsral Winter, making possibile nigth-time observations. The scientific importance of Concordia station is certified by the great number of international projects hosted in almost every sector of the environmental sciences and astronomy. It is considered representative of the entire Antarctic Plateau climate and weather conditions.

In figure 2.1 a map of the Antarctic continent is shown with in evidence the three permanent plateau stations (Dome C, Vostok, South Pole).

In this chapter we will give a detailed description of the measurement site, i.e. its climatic characterization and the instrumental set up along with an overview of our dataset.

## 2.1 Climate and environment

We analyzed meteorological data provided by the Antarctic Meteorological Research Center (AMRC) and Automatic Weather Station (AWS) program, that comprehend ground temperature (sensor altitude: 2 meters), pressure, relative humidity, wind speed and direction 1-minute measurements. In order to obtain a


Figure 2.1: Map of Antarctica with in evidence the three permanent Plateau stations. Image from *http* : *//lima.nasa.gov/pdf/A3_overview.pdf*.

climatological characterization of the site we computed the yearly, montly and daily averages of the various atmospheric parameters for the period April 2007/September 2015.

The typical climate of the Antarctic plateau is cold and dry, with weaker winds and clearer skies with respect to the coastal region. Concordia station has never recorded a temperature above freezing. Its extreme temperatures result from its latitude and altitude: for three months per year no solar radiation arrives (Polar Winter), and during the Summer, as the surface is covered with snow, more radiation is reflected than absorbed.

In figure 2.2 the montly and yearly averages of temperature are showed. A well

defined yearly cycle is visible, with maxima that don't exceed -30$^o$C taking place in January or December and minima falling between -70$^o$C and -65$^o$C occurring in August: the thermal excursion between Summer and Winter was of about 35$^o$C in 2007, 2008, 2009 and 2014 and of about 40$^o$C in 2010, 2011 and 2012. The overall trend throughout the years is slightly ascendent until 2011 and sligthly descendent from 2011 onwards, fluctuating between -58$^o$C and -52$^o$C. It must be pointed out that the first and last yearly averages do not take in account the missing months of years 2007 (from January to March) and 2015 (from October to December), so their values aren't as reliable as the others.

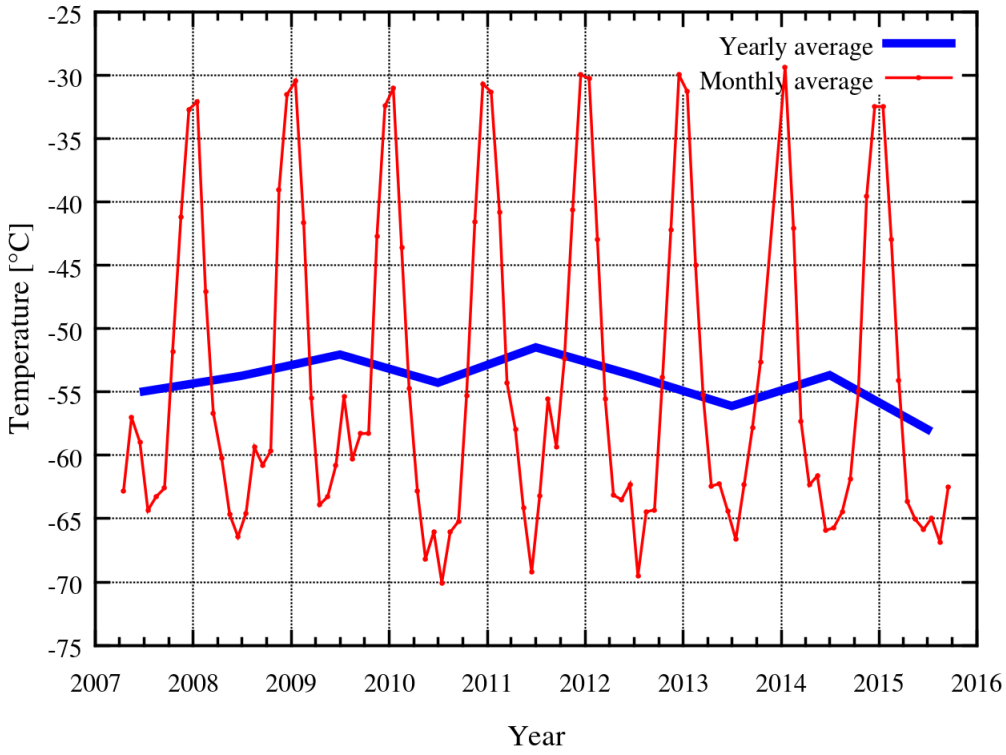


Figure 2.2: Monthly (red thin line) and yearly (blue thick line) mean of atmospheric temperature recorded at Dome C between April 2007 and September 2015.

In figure 2.3 the average daily trend of temperature divided by month is shown: different colours are used to distinguish seasons. Winter months do not

present a daily cycle, as expected as a consequence of the absece of the Sun, and temperature remains fairly constant around -65$^o$. In April and Septemper the Sun is above the horizon for a part of the day so a rise is observed after noon; this effect becomes more evident in October and March. During the remaining four months the daylight hours are 24 so a typical diurnal cycle sets up, with minimum temperature reached between 3:00 and 4:00 and maximum occurring around 15:00: these times of the day do not correspond to minimum and maximum insolation hours, as a certain time span is required for the snow to cool down and heat up. There is a difference of almost 15$^o$ between December-January and November-February daily curves: this is a consequence of the minor amount of incoming solar radiation, as it depends on the the solar zenith angle, which is lower in December and January.

A temperature inversion in the first kilometre of the atmosphere is present for most of the year, stronger in the Winter season, when it reaches 20$^o$C (difference between temperature at the top of the inversion layer and the ground temperature), whereas it almost disappears during Summer months (December, January).

For what concerns the atmspheric pressure no seasonal cycle is evident, with peaks occurring in both Summer and Winter seasons. Yearly averages oscillate between 640 hPa and 645 hPa, with a standard deviation of about 10 hPa: values are so low because of the altitude of the site.

On the Antarctic plateau, on average, a zone of high pressure exists throughout the year resulting in light winds and clear sky, although oceanic storms do occasionally penetrate inland to create hazardous conditions; Dome C does not experience the strong katabatic winds typical of the coastal regions because of its elevated location and its relative distance from the edges of the Antarctic Plateau. In figure 2.4 the wind rose for the whole period is shown. Only a small percentage of data are above 8 m/s, whereas the mean wind speed is between 2 m/s and 4 m/s. The main wind direction is Southward, with lower peaks in the SO or SSO direction: this is a weak surface wind that comes from the highlands in the interior of the continent. Montly averaged wind roses have been analysed too, and only little typical monthly features in the wind direction

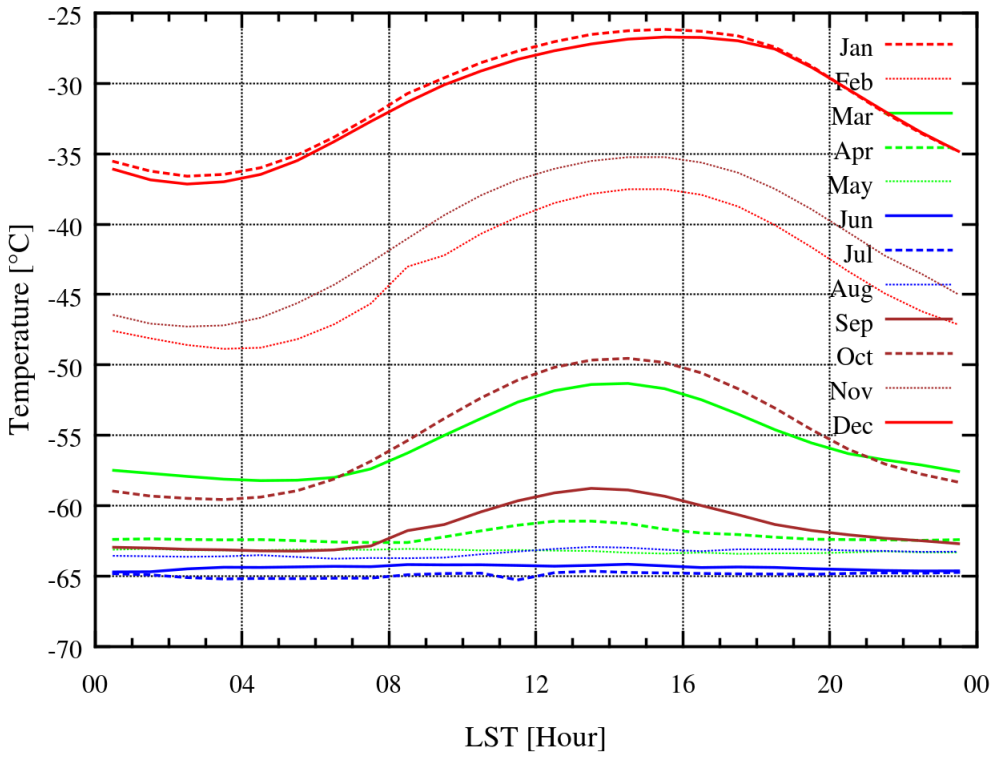


Figure 2.3: Daily curves of temperature computed for every month: every curve is obtained averaging out data from the whole period. Different colours are used to distinguish seasons.

have been identified: for the whole year the prevailing wind is southward, excepted for January and February, when most of the wind measurements are in SO and SSO direction, and during Winter months (June, July and August) 5% of the data is in the northward direction, maybe as a result of the penetration of oceanic storms coming from the coastal region, that is more likely to happen during Winter.

Humidity is also low (temperatures are cold) so that little water is available for precipitations, that in fact are very low, namely 5 $cm^2$/year on the average. Absolute humidity varies regularly with season within the low troposphere, presenting marked peaks in the summer months (40 % at the surface). As a result of the extreme temperatures, marked instrumental errors and dry biases

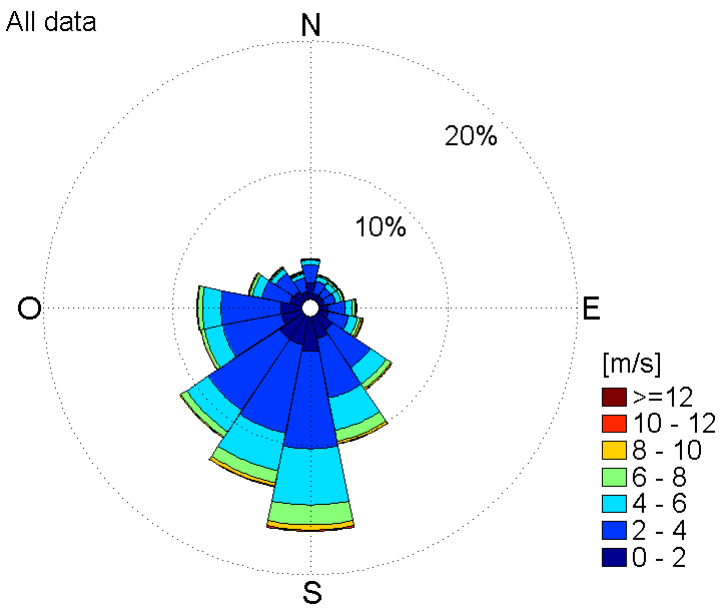


Figure 2.4: Wind rose calculated using all the available data of the period April 2007/September 2015.

are producted in the radiosonde measurements of humidity, which therefore require appropriate correction procedure (Tomasi et al., 2012).

## 2.2 Instrumental set up

The radiometric measurement station build in Dome C is a part of the Baseline Surface Radiation Network (BSRN), a World Climate Research Programme (WCRP) project for monitoring Earth's radiation field at the Earth's surface, providing high quality observations for shortwave and longwave surface radiation fluxes, that can be used for the validation and evaluation of satellite-based estimates of the surface radiative fluxes and for comparison to climate model (GCM) calculations and for the development of local regionally representative radiation climatologies.

As all the BSRN stations at Dome C continuous measurements of broadband surface irradiance, 0.3 $\mu$m-3$\mu$m for the solar radiation and the band 3$\mu$-50$\mu$m for

longwave radiation, are carried on with a 1-minute rate. Radiation measurements are performed through pyranometers, pyreliometers and pyrgeometers. It follows a description of the main characteristics of these devices.

- PYRANOMETER: it is used to measure global solar radiation, so it must respond both to the direct solar beam and to diffuse sky radiation from the whole hemisphere (fiel of view of $180^o$). The sensing element (a thermopile with a black coating) is covered with a a quartz dome with transmittance that approaches unity in the visible and near IR wavelength range (0.3 $\mu$m-4$\mu$m); the glass shield is necessary to isolate the sensor from the environment (wind, rain, etc.). Our pyranometers are ventilated to avoid additional heating of dome.

- PYRGEOMETER: it is used to measure longwave radiation in region between 3$\mu$m and 50$\mu$m. Tipically a flat silicon window is used to isolate the sensing element (thermopile) from the environment, and to filter only IR radiation.

- PYRHELIOMETER: it measures the direct solar beam. Its sensing element is constitued by a thermal detector. It must be kept normal to the solar beam and therefore the pyrheliometer must be pointed at the Sun through a tracking mechanism. Its field of view should be small ($5^o$) in order to exclude the scattered sky radiation

At Dome C both the upwelling and downwelling components are mesured, downwlling components since the end of 2005, while upwelling cpmponents are measured at a height of 3 m above the ground since the begining of 2007. All measurements are carried on using secondary standard pyranometer (Kipp & Zonen CM22), pyreliometer (Kipp & Zonen CH1) and pyrgeometer (Kipp & Zonen CG4). Measure of diffuse and downwelling longwave radiation are performed with shadowbands on the radiometers. For what concerns the upwelling measurements of shortwave radiation, two CM22 have been located on the opposite sites of the so called albedo rack. In figure 2.5 is shown the instrumental set up for downwelling and upwlling measurements.

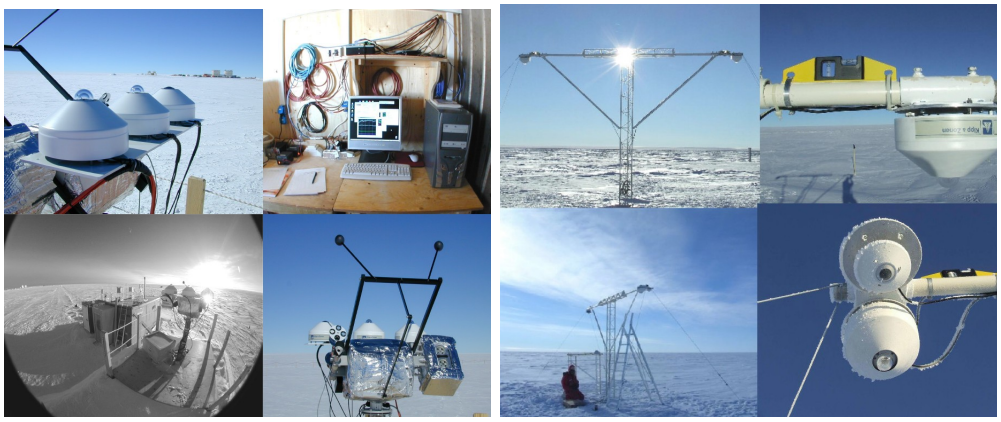

Figure 2.5: Pictures of the radiation measurements instrumental set up at Concordia station. On the left are shown the devices for downwelling irradiance measurement, on the right the albedo rack for upwelling irradiance measurements, with pyranometer $p_A$ and $p_B$, and pyrgeometer.

All instruments are periodically calibrated following Pmod-LTD guideline (see *https : //www.pmodwrc.ch/pmod.php?topic = calibration* and references therein).

## 2.3 Dataset overview

Signals are acquired by a datalogger (Campbell) every second and the 1-minute average along with standard deviation, minimum and maximum values represent the raw data obtained from the measurement system. These 1-minute raw data are corrected following BSRN guidelines (McArthur, 2004), in order to eliminate instrumental errors. These corrections take in account the temperature compensation of the calibration constant variability for all the instruments, the thermal offset for pyranometers and pyrgeometers and the cosine response for unshaded pyramoneters, and are reported in equations 2.1, 2.2 and 2.3. For pyranometers, pyrheliometers and pyrgeometers the corrected irradiance are respectively $F_{c,pn}$, $F_{c,pg}$ and $F_{c,ph}$ and are given by:

$$F_{c,pn} = SR(T)R(\mu)(F_{pn} - F_0) \tag{2.1}$$

$$F_{c,pg} = SR(T)(F_{pg} - F_0) \tag{2.2}$$

$$F_{c,ph} = SR(T)F_{ph} \tag{2.3}$$

where S is the radiometer sensitivity, R(T) is the temperature correction, R($\mu$) is the cosine response correction ($\mu$=cos($\theta$), with $\theta$ the solar zenith angle), $F_0$ is the night offset, and $F_{c,pn}$, $F_{c,pg}$ and $F_{c,ph}$ are the measured signals.

The thermal offset (or night offset) $F_0$ is the thermal signal of the sensing element, so that the radiometer measures a nonzero irradiance even if no sources are present. For the pyranometer its value is estimated to be about 2 W/m$^2$, whether for the pyreliometer it is less than the instrument accuracy, so that no correction is needed; pyrgeometer it is not affected by night offset errors. The cosine correction R($\mu$) only affects the pyranometer signal (i.e. the global irradiance measurements). Under ideal conditions a pyranometer should have a so-called ″cosine response″ (full response when the Sun is perpendicular to the sensor and zero response at solar zenith angle of 90$^o$), however in the reality this response deviates from ideal and shall be corrected (on average it falls between -1.5 W/m$^2$ and 1.5 W/m$^2$). The temperature correction R(T) is an adjustment to the instrument sensitivity, that changes with outside temperature. The sensitivity correction due to temperature is given by the manufacturer only until -20$^o$C, whereas the temperature range at Dome C is from -80$^o$C to -25$^o$C. The common approach here is to extrapolate to lower temperatures the sensitivity using a third degree polynomial (Su et al., 2008); at -60$^o$C the correction is of 10%. In table 2.1 a summary of the instruments' technical characteristics and errors is given.

From January 2012 to December 2013 a new calibration has been applied to the pyrgeometer. We corrected 2012/13 data using the constructor formula:

$$F_{LW,new} = (F_{LW,old} - \sigma T^4)(1 + k_1\sigma T^3) + k_2\sigma T^4 \tag{2.4}$$

where $k_1$=0.04, $k_2$=0.9967 and T is the body temperature of the pyrgeometer, instead of the previous one $F_{LW,old}=\frac{U}{S_1}(1+\sigma\ T^4)$, where $S_1$=10.03. In figure 2.6 the difference between the old/new calibration are shown for the two years considered: values oscillate between 1 W/m$^2$ and 5 W/m$^2$.

| | CM22<br>secondary standard pyranometer | CG4<br>pyrgeometer |
|---|---|---|
| Spectral range | 280-2800 nm | 4.5-42 $\mu$m |
| Sensitivity | 10 $\mu$V/W/m$^2$ | 10 $\mu$V/W/m$^2$ |
| Response time | 5 s | 25 s |
| Non linearity | $\pm$0.2% | $< \pm$1% |
| Temperature correction | $\pm$0.5% (-20$^o$C to 50$^o$C) | $\pm$1% |
| Zero offset | 3 W/m$^2$ | <2 W/m$^2$ |
| Operating temperature | -40$^o$C to 80$^o$C | -40$^o$C to 80$^o$C |
| Viewing angle | 2$\pi$ sr | 2$\pi$ sr |
| Cosine response | $\pm$1% ($\theta$=60$^o$), $\pm$3% ($\theta$=80$^o$) | no |

Table 2.1: Technical characteristics and errors for pyranometer and pyrgeometer, from Kipp & Zonen instruction manuals.

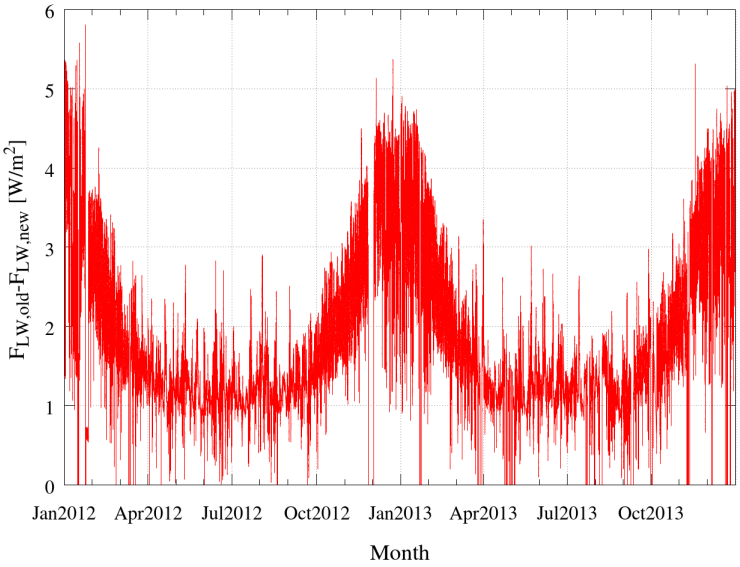


Figure 2.6: Differences between measured longwave irradiance and longwave irradiance corrected using equation 2.4.

After the raw data has been corrected using equations 2.1, 2.2 and 2.3, a strongly defined quality check (QC) has been performed in order to conform to

BSRN standards (Long and Dutton, 2002). The quality check ensures that irradiance measurements fall between certain limits (divided in physical possible limits, PPL, and extremely rare limits, ERL) and satisfy certain intercomparison criteria. The tresholds are illustrated in tables 2.2, 2.3 and 2.4.

| | PPL | | ERL | |
|---|---|---|---|---|
| | Min [W/m$^2$] | Max [W/m$^2$] | Min [W/m$^2$] | Max [W/m$^2$] |
| Global | -4 | 1.5S$_a$ $\mu_0^{1.2}$100 | -2 | 1.2S$_a$ $\mu_0^{1.2}$50 |
| Diffuse | -4 | 0.95S$_a$ $\mu_0^{1.2}$50 | -2 | 0.75S$_a$ $\mu_0^{1.2}$30 |
| Direct | -4 | S$_a$ | -2 | 0.95S$_a$ $\mu_0^{0.2}$+10 |
| Longwave | 40 | 700 | 60 | 500 |

Table 2.2: BRSN quality check physical possible limits and extremely rare limits for absolute values of irradiance. Here S$_a$=$\frac{S_0}{AU2}$ is the solar constant adjusted for Sun-Earth distance and $\mu_0$=cos($\theta$) is the cosine of the solar zenith angle.

| | $\theta < 75^o$ | $93^o < \theta < 75^o$ |
|---|---|---|
| Glo-Sum Ratio | $0.92 < \frac{Glo}{Dif+Dir} < 1.08$ | $0.85 < \frac{Glo}{Dif+Dir} < 1.15$ |
| Diffuse Ratio | $\frac{Dif}{Glo} < 1.05$ | $\frac{Dif}{Glo} < 1.10$ |
| Up irradiance | SW$_{up}$ < Sum (or Glo) | |

Table 2.3: BRSN quality check limits for compared shortwave measurements.

| | Min [W/m$^2$] | Max [W/m$^2$] |
|---|---|---|
| LW$_{down}$ (1) | 0.4 $\sigma$ T$_a$ $^4$ | $\sigma$ T$_a$ $^4$ + 25 |
| LW$_{up}$ | $\sigma$ (T$_a$ -15)$^4$ | $\sigma$ (T$_a$ + 25)$^4$ |
| LW$_{down}$ (2) | LW$_{up}$ - 300 | LW$_{up}$ + 25 |

Table 2.4: BRSN quality check limits for compared longwave measurements. Here T$_a$ is the air temperature in Kelvin and $\sigma$=5.67 $10^{-8}$ is the Stefan-Boltzmann constant.

The BSRN guidelines clearly indicate that ERL should be defined according to a significant climatology of the site and values valid for one station could not be applied to another. At Dome C for example it was observed that the lower longwave ERL (+60 W/m$^2$) was experienced many times (12%), with the $10^{th}$ percentile of 58 W/m$^2$ and median value of 79 W/m$^2$ and a $90^{th}$ percentile of 98 W/m$^2$ (Lanconelli et al., 2012). However we kept the limit found in Long and Dutton (2002).

A final visual inspection of the time series of irradiances in various time resolutions and combinations with other information, has been performed, being considered the most effective test (Ohmura et al., 1998; Long and Shi, 2008; Long and Dutton, 2002).

After the quality check procedure has been performed data are ready to be analysed. All bad data are set to -9999 and are excluded from the analysis. In section 2.3.1 the results of the quality check are shown in terms of percentage of bad data per year, for all the irradiance components.

In figure 2.7 the average yearly trend is shown for the four irradiance components, i.e. shortwave upwelling and downwelling irradiance ($F_{\uparrow,SW}$ and $F_{\downarrow,SW}$), and longwave upwelling and downwelling irradiance ($F_{\uparrow,LW}$ and $F_{\downarrow,LW}$). Every point is a daily mean performed on all the 1-minute data of that day from the different years.

The Sun elevation is the leading factor in controlling the shortwave irradiance tendency: its value is zero from May to the first week of August, when the yearly last sunset and first sunrise occurr. For the rest of the year the average irradiance is proportional to $\cos(\overline{\theta})$, where $\overline{\theta}$ is the daily average value of the solar zenit angle (the minimum value of the solar zenith angle at Dome C is of about $50^o$ at midday during Austral Summer). The upwelling irradiance (i.e. the solar irradiance reflected by the surface) is significantly lower than the downwelling one only from November to the end of February, probably as a consequence of the fact that at higher solar elevations a larger part of the incoming irradiance is absorbed by the surface, while at low incidence angles it is most likely reflected. The maximum value of the downwelling irradiance is about 450 W/m$^2$, whereas it

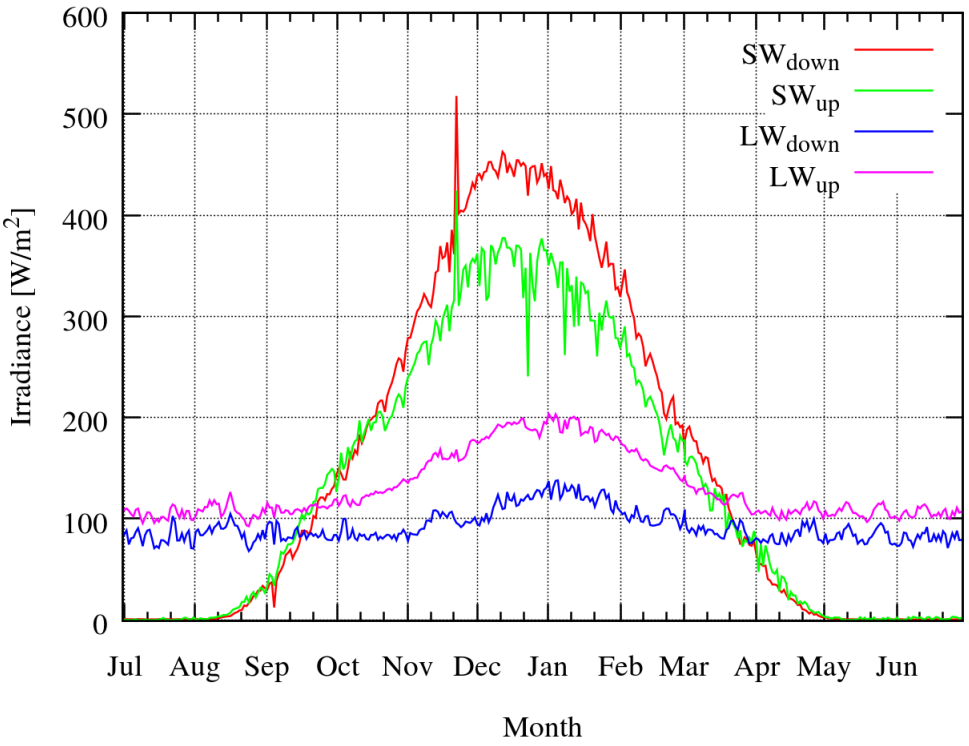


Figure 2.7: Typical yearly trend of the different irradiance components (shortwave upwelling and downwelling, longwave upwelling and downwelling). A daily average has been performed using the available measurements from the whole period.

is about 370 W/m$^2$ for the upwelling one, both occurring in December.

The longwave upwelling irradiance is the radiation emitted by the snow surface. It is never zero and assumes an almost constant value of 100 W/m$^2$ from the beginning of April to the middle of September, when the system is not affected by the solar heating and surface temperature is nearly constant (see figure 2.3); from October to December its average value increases to 200 W/m$^2$ and then decreases again. The longwave downwelling irradiance, i.e. the one emitted by the atmospheric gases (in particular water vapour) and aerosols, presents more of less the same features of the upwelling one, remaining fairly constant around 90 W/m$^2$ during Antarctic Winter months and slightly increasing to a maximum of about 120 W/m$^2$ between December and January; this fact means that atmospheric

temperature is not as sensible as the surface one to the Solar heating.

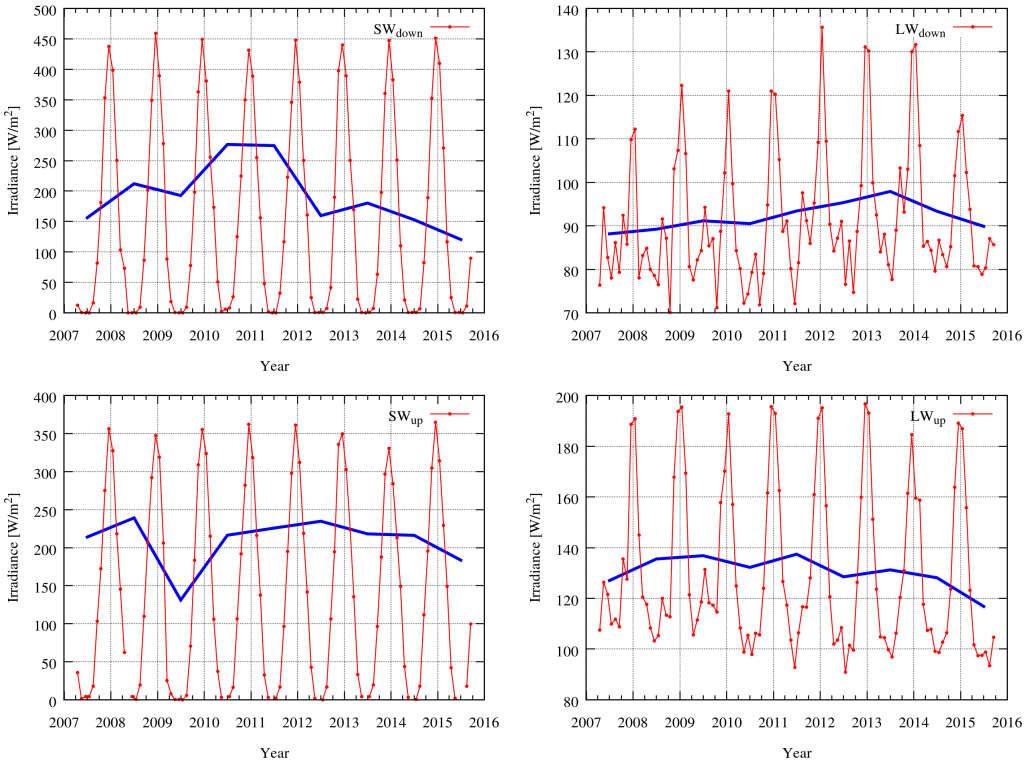


Figure 2.8: Monthly (red thin line) and yearly (blue thick line) mean of shortwave downwelling (top left) and upwelling (bottom left) and longwave downwelling (top right) and upwelling (bottom right) irradiance measured at Dome C from April 2007 to September 2015.

In figure 2.8 the monthly and yearly averages of the time series of the different irradiance components are shown for our period of study.

The monthly trends of the shortwave irradiances do not present features different from the already described ones: maxima of around 450 W/m$^2$ for the downwelling and of around 350 W/m$^2$ for the upwelling irradiance always occurr in December. The yearly trend for $F_{\downarrow,SW}$ oscillate between 100 W/m$^2$ and 300 W/m$^2$, with highest value occurring in 2010 and 2011; for what concerns the yearly $F_{\uparrow,SW}$ it remains fairly constant between 200 W/m$^2$ and 250 W/m$^2$ for the whole period, excepted for a minimum of 130 W/m$^2$ in 2009.

The behavior of $F_{\downarrow,LW}$ is the most interesting as it presents a rise of about 100 W/m$^2$ in its maximum values during 2012, 2013 and 2014 (the same is observed in the yearly average). This in part is due to the different calibration formula that has been employed for the pyrgeometer during that period, issue that will be discussed in previous section, and in part can be an effect of an increase of the atmospheric moisture.

The last plot of $F_{\uparrow,LW}$ presents a regular behavior throughout the years, oscillating between 90 W/m$^2$ in colder months and 200 W/m$^2$ in warmer months.

### 2.3.1 Quality check results

In the following the results of the BSRN quality check performed on data is illustrated for every year in our dataset. The plots on the left show the different irradiance components 1-minue data (gold line), namely:

- GloB: upwelling irradiance measured by down-facing pyranometer $p_B$;
- GloA: upwelling irradiance measured by down-facing pyranometer $p_A$;
- Lwu: upwelling longwave irradiance;
- Lwind dir.: downwelling longwave irradiance;
- Dir: direct solar irradiance;
- Dif: diffuse solar irradiance;
- Glo: global solar irradiance.

The blue-red bar at the bottom of each graph represents good-bad data respectively, as results of the qc test. The percentage of missing data on the annual total number is also indicated, along with some statistical informations (maximum, minimum, mean, median, $95^{th}$ percentile). The plots on the right are the frequency histograms of the different radiation measurements.

It must be noted that the high percentage of missing data in 2007 and 2015 are not only a consequente of the quality check, but represent the data not present in our dataset.

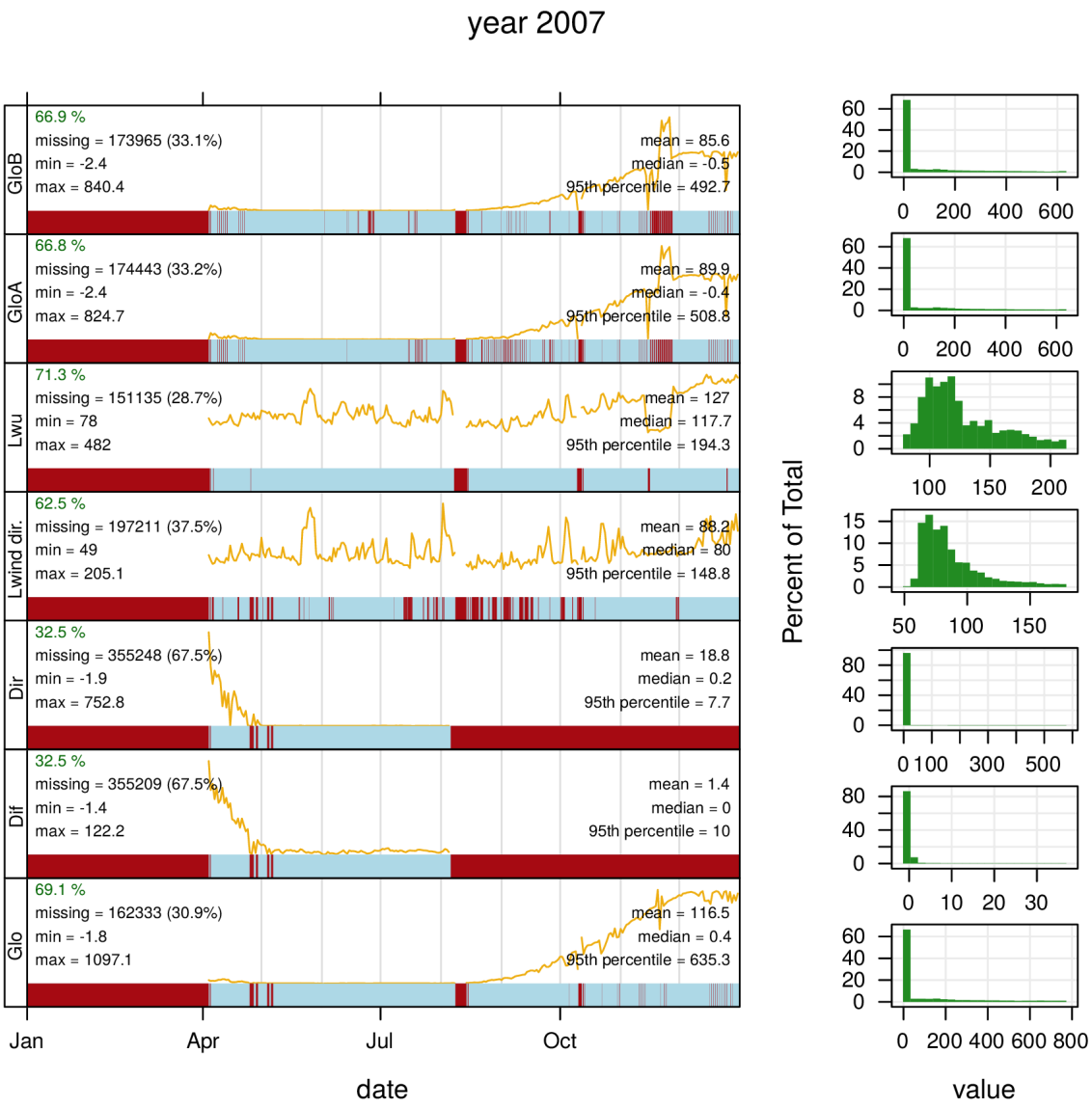
year 2007
GloB
66.9 %
missing = 173965 (33.1%)
min = -2.4
max = 840.4
mean = 85.6
median = -0.5
95th percentile = 492.7
GloA
66.8 %
missing = 174443 (33.2%)
min = -2.4
max = 824.7
mean = 89.9
median = -0.4
95th percentile = 508.8
Lwu
71.3 %
missing = 151135 (28.7%)
min = 78
max = 482
mean = 127
median = 117.7
95th percentile = 194.3
Lwind dir.
62.5 %
missing = 197211 (37.5%)
min = 49
max = 205.1
mean = 88.2
median = 80
95th percentile = 148.8
Dir
32.5 %
missing = 355248 (67.5%)
min = -1.9
max = 752.8
mean = 18.8
median = 0.2
95th percentile = 7.7
Dif
32.5 %
missing = 355209 (67.5%)
min = -1.4
max = 122.2
mean = 1.4
median = 0
95th percentile = 10
Glo
69.1 %
missing = 162333 (30.9%)
min = -1.8
max = 1097.1
mean = 116.5
median = 0.4
95th percentile = 635.3
Jan
Apr
Jul
Oct
date
Percent of Total
value

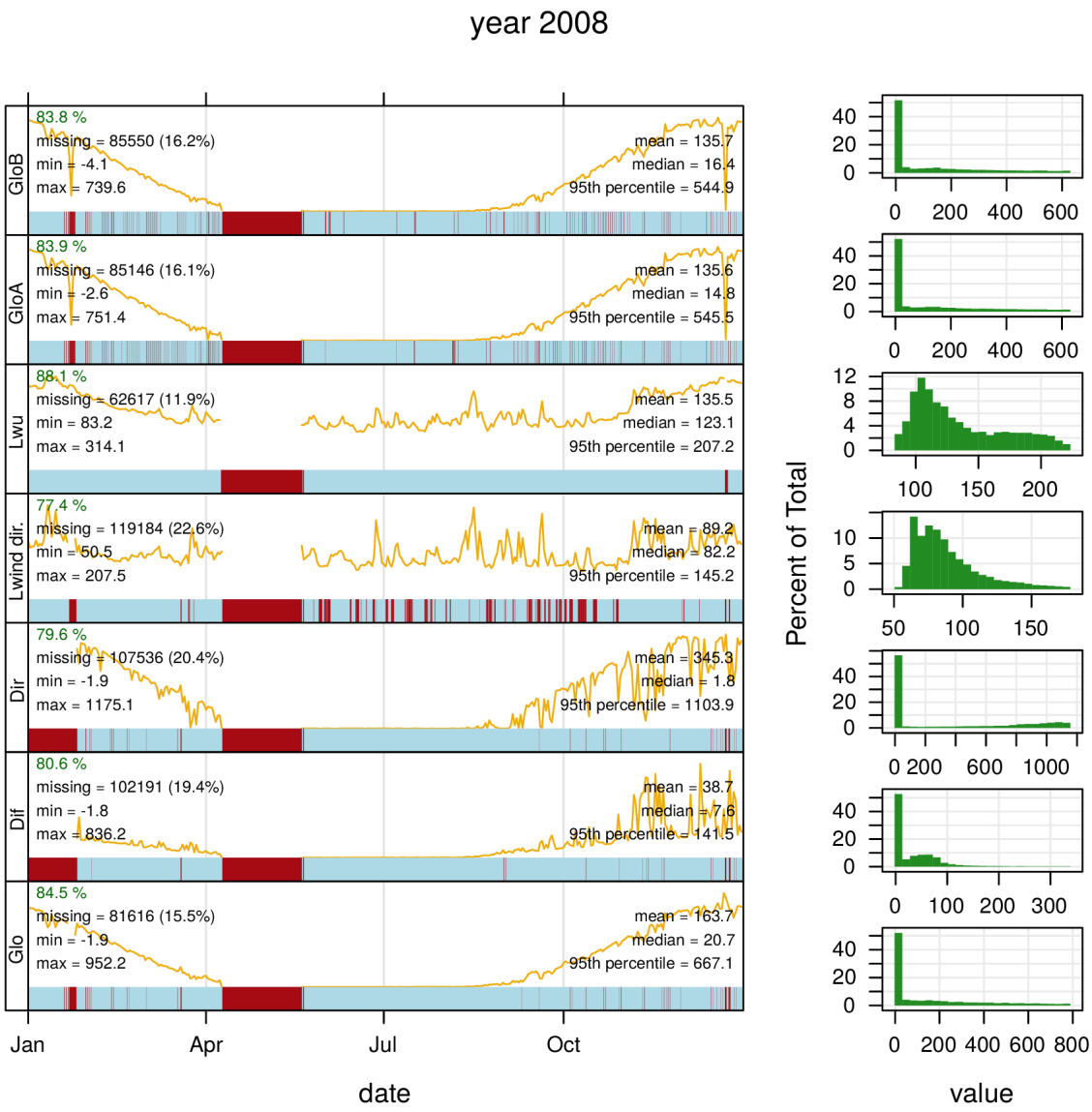
year 2008
GloB
83.8 %
missing = 85550 (16.2%)
min = -4.1
max = 739.6
mean = 135.7
median = 16.4
95th percentile = 544.9
GloA
83.9 %
missing = 85146 (16.1%)
min = -2.6
max = 751.4
mean = 135.6
median = 14.8
95th percentile = 545.5
Lwu
88.1 %
missing = 62617 (11.9%)
min = 83.2
max = 314.1
mean = 135.5
median = 123.1
95th percentile = 207.2
Lwind dir.
77.4 %
missing = 119184 (22.6%)
min = 50.5
max = 207.5
mean = 89.2
median = 82.2
95th percentile = 145.2
Dir
79.6 %
missing = 107536 (20.4%)
min = -1.9
max = 1175.1
mean = 345.3
median = 1.8
95th percentile = 1103.9
Dif
80.6 %
missing = 102191 (19.4%)
min = -1.8
max = 836.2
mean = 38.7
median = 7.6
95th percentile = 141.5
Glo
84.5 %
missing = 81616 (15.5%)
min = -1.9
max = 952.2
mean = 163.7
median = 20.7
95th percentile = 667.1
Jan
Apr
Jul
Oct
date
Percent of Total
value

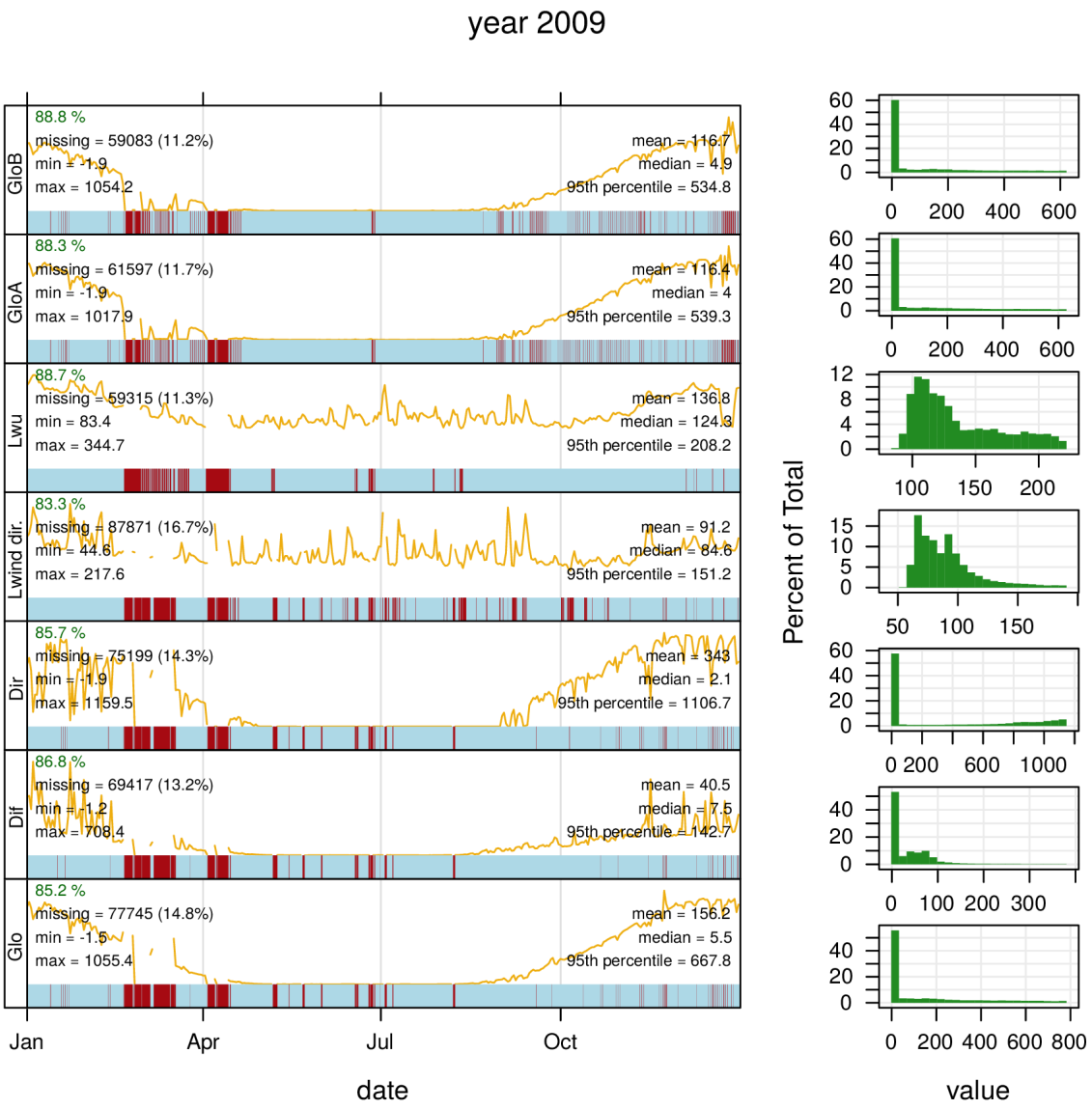
year 2009
GloB
88.8 %
missing = 59083 (11.2%)
min = -1.9
max = 1054.2
mean = 116.7
median = 4.9
95th percentile = 534.8
GloA
88.3 %
missing = 61597 (11.7%)
min = -1.9
max = 1017.9
mean = 116.4
median = 4
95th percentile = 539.3
Lwu
88.7 %
missing = 59315 (11.3%)
min = 83.4
max = 344.7
mean = 136.8
median = 124.3
95th percentile = 208.2
Lwind dir.
83.3 %
missing = 87871 (16.7%)
min = 44.6
max = 217.6
mean = 91.2
median = 84.6
95th percentile = 151.2
Dir
85.7 %
missing = 75199 (14.3%)
min = -1.9
max = 1159.5
mean = 343
median = 2.1
95th percentile = 1106.7
Dif
86.8 %
missing = 69417 (13.2%)
min = -1.2
max = 708.4
mean = 40.5
median = 7.5
95th percentile = 142.7
Glo
85.2 %
missing = 77745 (14.8%)
min = -1.5
max = 1055.4
mean = 156.2
median = 5.5
95th percentile = 667.8
Jan
Apr
Jul
Oct
date
Percent of Total
value

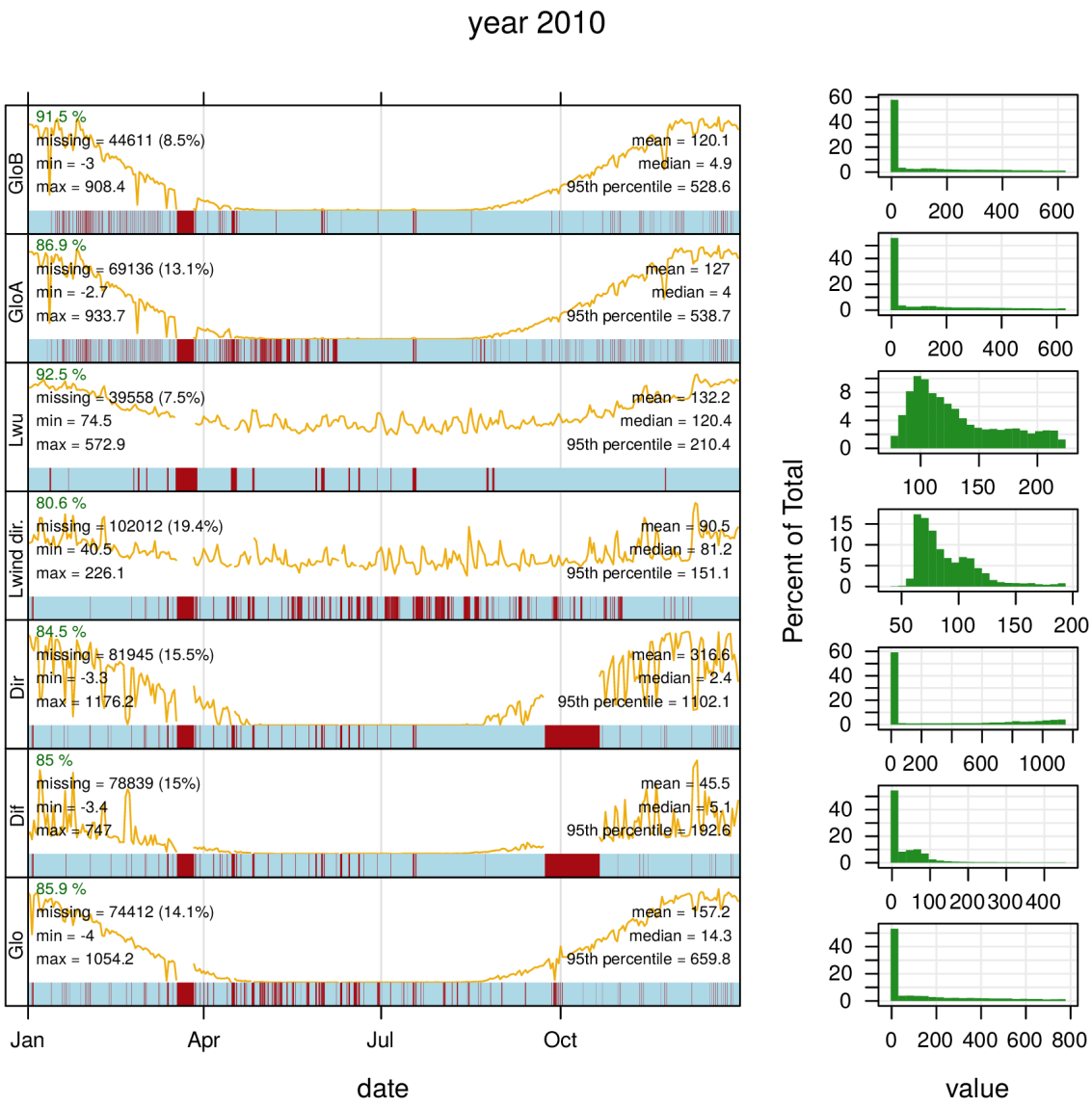
year 2010
GloB
91.5 %
missing = 44611 (8.5%)
min = -3
max = 908.4
mean = 120.1
median = 4.9
95th percentile = 528.6
GloA
86.9 %
missing = 69136 (13.1%)
min = -2.7
max = 933.7
mean = 127
median = 4
95th percentile = 538.7
Lwu
92.5 %
missing = 39558 (7.5%)
min = 74.5
max = 572.9
mean = 132.2
median = 120.4
95th percentile = 210.4
Lwind dir.
80.6 %
missing = 102012 (19.4%)
min = 40.5
max = 226.1
mean = 90.5
median = 81.2
95th percentile = 151.1
Dir
84.5 %
missing = 81945 (15.5%)
min = -3.3
max = 1176.2
mean = 316.6
median = 2.4
95th percentile = 1102.1
Dif
85 %
missing = 78839 (15%)
min = -3.4
max = 747
mean = 45.5
median = 5.1
95th percentile = 192.6
Glo
85.9 %
missing = 74412 (14.1%)
min = -4
max = 1054.2
mean = 157.2
median = 14.3
95th percentile = 659.8
Jan
Apr
Jul
Oct
date
Percent of Total
value

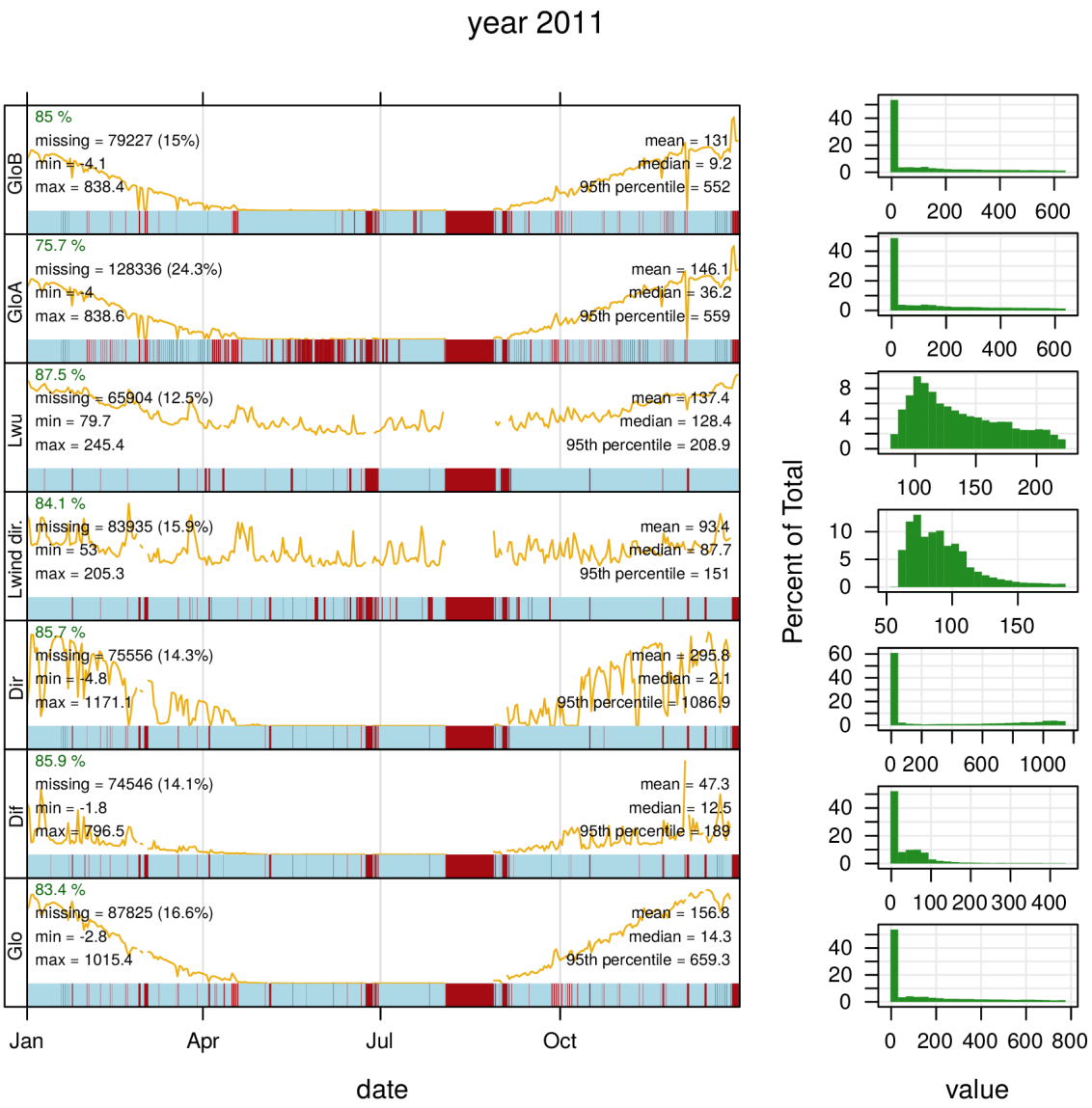
year 2011
GloB
85 %
missing = 79227 (15%)
min = -4.1
max = 838.4
mean = 131
median = 9.2
95th percentile = 552
GloA
75.7 %
missing = 128336 (24.3%)
min = -4
max = 838.6
mean = 146.1
median = 36.2
95th percentile = 559
Lwu
87.5 %
missing = 65904 (12.5%)
min = 79.7
max = 245.4
mean = 137.4
median = 128.4
95th percentile = 208.9
Lwind dir.
84.1 %
missing = 83935 (15.9%)
min = 53
max = 205.3
mean = 93.4
median = 87.7
95th percentile = 151
Dir
85.7 %
missing = 75556 (14.3%)
min = -4.8
max = 1171.1
mean = 295.8
median = 2.1
95th percentile = 1086.9
Dif
85.9 %
missing = 74546 (14.1%)
min = -1.8
max = 796.5
mean = 47.3
median = 12.5
95th percentile = 189
Glo
83.4 %
missing = 87825 (16.6%)
min = -2.8
max = 1015.4
mean = 156.8
median = 14.3
95th percentile = 659.3
Jan
Apr
Jul
Oct
date
Percent of Total
value

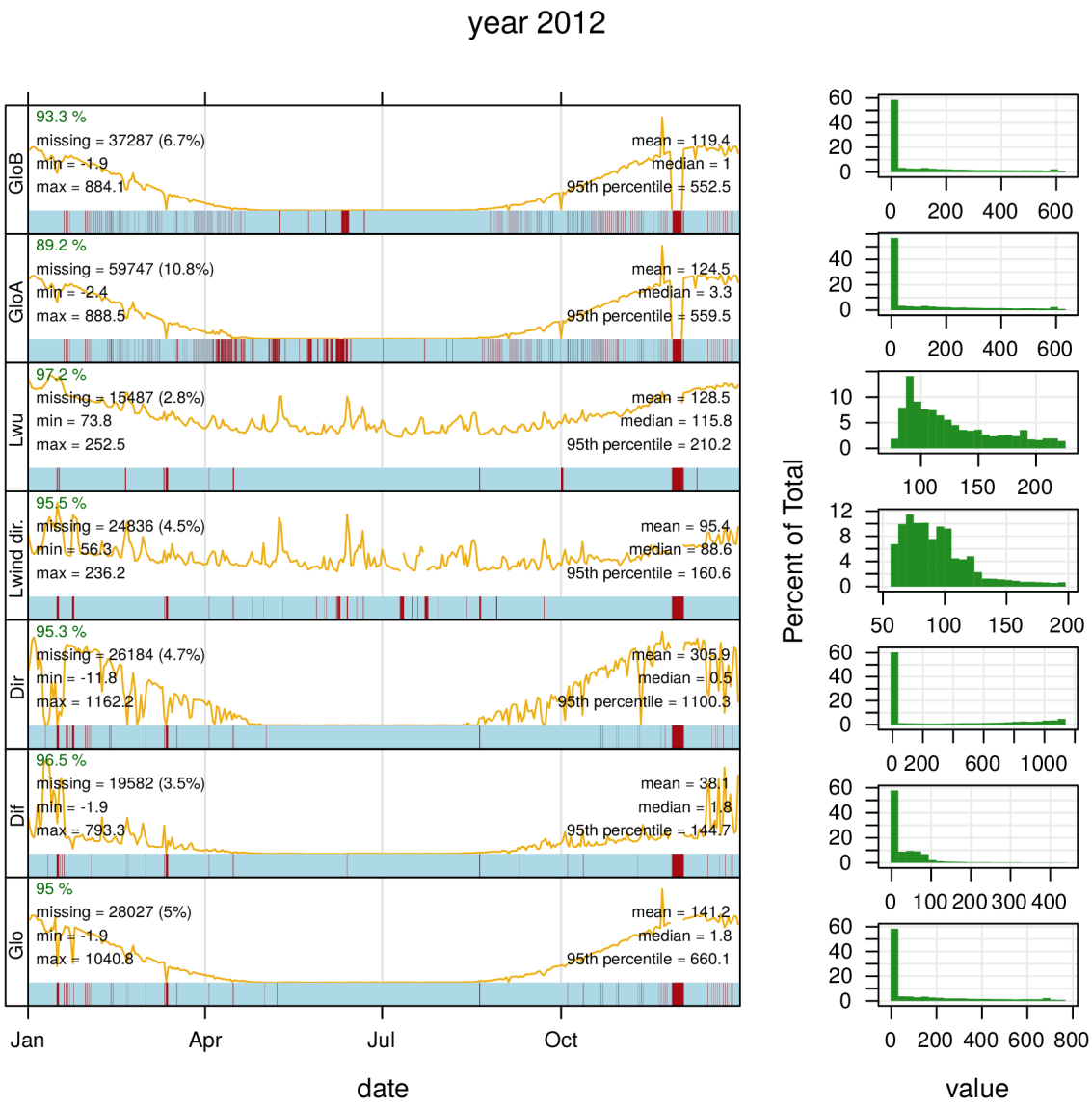
year 2012
GloB
93.3 %
missing = 37287 (6.7%)
min = -1.9
max = 884.1
mean = 119.4
median = 1
95th percentile = 552.5
GloA
89.2 %
missing = 59747 (10.8%)
min = -2.4
max = 888.5
mean = 124.5
median = 3.3
95th percentile = 559.5
Lwu
97.2 %
missing = 15487 (2.8%)
min = 73.8
max = 252.5
mean = 128.5
median = 115.8
95th percentile = 210.2
Lwind dir.
95.5 %
missing = 24836 (4.5%)
min = 56.3
max = 236.2
mean = 95.4
median = 88.6
95th percentile = 160.6
Dir
95.3 %
missing = 26184 (4.7%)
min = -11.8
max = 1162.2
mean = 305.9
median = 0.5
95th percentile = 1100.3
Dif
96.5 %
missing = 19582 (3.5%)
min = -1.9
max = 793.3
mean = 38.1
median = 1.8
95th percentile = 144.7
Glo
95 %
missing = 28027 (5%)
min = -1.9
max = 1040.8
mean = 141.2
median = 1.8
95th percentile = 660.1
Jan
Apr
Jul
Oct
date
Percent of Total
value

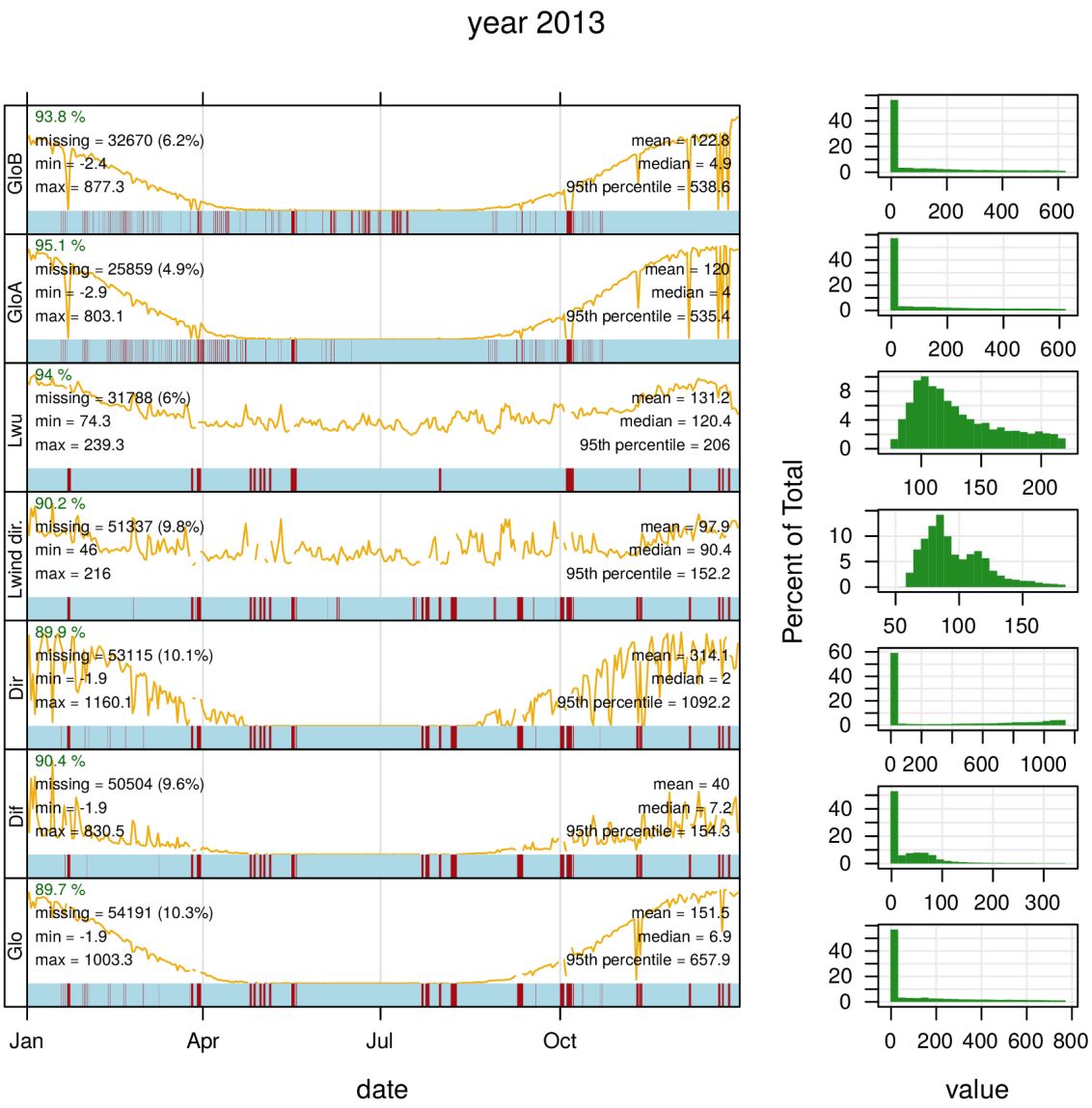
year 2013
GloB
93.8 %
missing = 32670 (6.2%)
min = -2.4
max = 877.3
mean = 122.8
median = 4.9
95th percentile = 538.6
GloA
95.1 %
missing = 25859 (4.9%)
min = -2.9
max = 803.1
mean = 120
median = 4
95th percentile = 535.4
Lwu
94 %
missing = 31788 (6%)
min = 74.3
max = 239.3
mean = 131.2
median = 120.4
95th percentile = 206
Lwind dir.
90.2 %
missing = 51337 (9.8%)
min = 46
max = 216
mean = 97.9
median = 90.4
95th percentile = 152.2
Dir
89.9 %
missing = 53115 (10.1%)
min = -1.9
max = 1160.1
mean = 314.1
median = 2
95th percentile = 1092.2
Dif
90.4 %
missing = 50504 (9.6%)
min = -1.9
max = 830.5
mean = 40
median = 7.2
95th percentile = 154.3
Glo
89.7 %
missing = 54191 (10.3%)
min = -1.9
max = 1003.3
mean = 151.5
median = 6.9
95th percentile = 657.9
Jan
Apr
Jul
Oct
date
Percent of Total
value

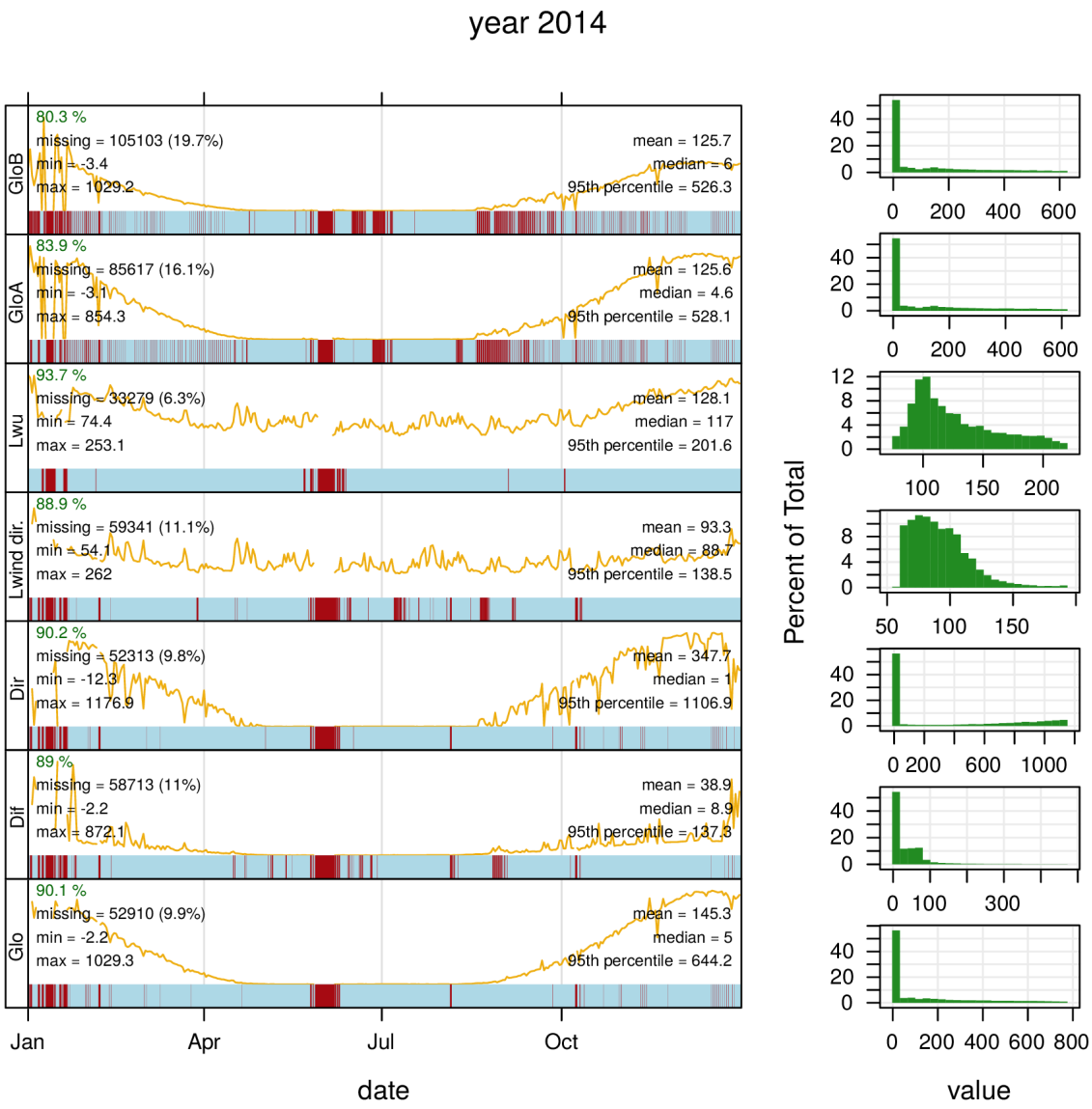
year 2014
GloB
80.3 %
missing = 105103 (19.7%)
min = -3.4
max = 1029.2
mean = 125.7
median = 6
95th percentile = 526.3
GloA
83.9 %
missing = 85617 (16.1%)
min = -3.1
max = 854.3
mean = 125.6
median = 4.6
95th percentile = 528.1
Lwu
93.7 %
missing = 33279 (6.3%)
min = 74.4
max = 253.1
mean = 128.1
median = 117
95th percentile = 201.6
Lwind dir.
88.9 %
missing = 59341 (11.1%)
min = 54.1
max = 262
mean = 93.3
median = 88.7
95th percentile = 138.5
Dir
90.2 %
missing = 52313 (9.8%)
min = -12.3
max = 1176.9
mean = 347.7
median = 1
95th percentile = 1106.9
Dif
89 %
missing = 58713 (11%)
min = -2.2
max = 872.1
mean = 38.9
median = 8.9
95th percentile = 137.3
Glo
90.1 %
missing = 52910 (9.9%)
min = -2.2
max = 1029.3
mean = 145.3
median = 5
95th percentile = 644.2
Jan
Apr
Jul
Oct
date
Percent of Total
value

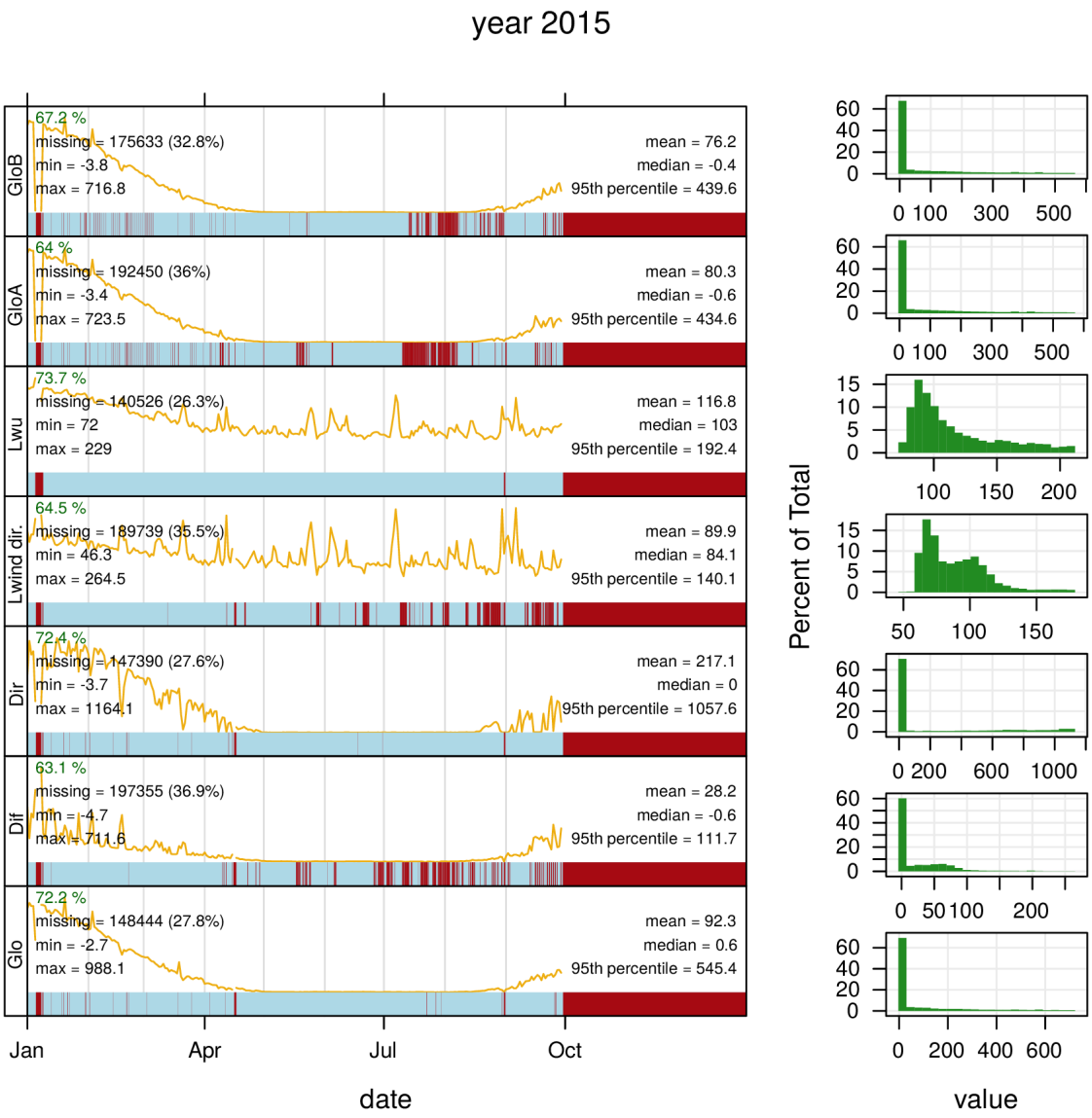
year 2015
GloB
67.2 %
missing = 175633 (32.8%)
min = -3.8
max = 716.8
mean = 76.2
median = -0.4
95th percentile = 439.6
GloA
64 %
missing = 192450 (36%)
min = -3.4
max = 723.5
mean = 80.3
median = -0.6
95th percentile = 434.6
Lwu
73.7 %
missing = 140526 (26.3%)
min = 72
max = 229
mean = 116.8
median = 103
95th percentile = 192.4
Lwind dir.
64.5 %
missing = 189739 (35.5%)
min = 46.3
max = 264.5
mean = 89.9
median = 84.1
95th percentile = 140.1
Dir
72.4 %
missing = 147390 (27.6%)
min = -3.7
max = 1164.1
mean = 217.1
median = 0
95th percentile = 1057.6
Dif
63.1 %
missing = 197355 (36.9%)
min = -4.7
max = 711.6
mean = 28.2
median = -0.6
95th percentile = 111.7
Glo
72.2 %
missing = 148444 (27.8%)
min = -2.7
max = 988.1
mean = 92.3
median = 0.6
95th percentile = 545.4
Jan
Apr
Jul
Oct
date
Percent of Total
value

# Chapter 3

# Cloud forcing on shortwave downwelling irradiance

In this chapter we will describe the metodology used to estimate the cloud forcing (CF) on the downwelling shortwave component. For this purpouse we employed an algorithm developed by Long and Ackerman (2000) that incorporates a cloud screening method and a fitting procedure to define clear sky irradiances.

In section 3.1 we will explain in detail how the algorithm works; in the following sections we will show the results of the calculation of the CF on the shortwave downwelling component.

## 3.1 Long and Ackerman algorithm

Long and Ackerman (2000) developed a methodology that identifies clear sky periods using high temporal resolution measurements of the downwelling global and diffuse shortwave irradiance. The advantage of this method rely on its independence on ancillary data like ozone and water vapor profiles and aerosol amounts (differently from other approaches, such as the use of radiative transfer models) as it only requires radiation measurements, performed with simply and versatile instrumens like pyranometers are.

Fundamental criteria is that for cloudy conditions the global and diffuse

shortwave irradiances differ from those measured under clear sky: in overcast conditions or in presence of large cumulus clouds the expected total irradiance can be less (negative cloud effect), while broken or thin clouds will increase the total irradiance for the enhancement of the diffuse component (positive cloud effect).

Here is a brief summary of how the algorithm works:

1. a series of test (see section 3.1.1) is performed on the dataset, in order to determine whether the measurements can be classified as clear or not;

2. if a sufficient number of data per day are detected as clear, these are used to fit a parametric model suitable to represent the typical bell-shaped clear sky irradiances (global and diffuse);

3. the fitting coefficients are tested to verify their reliability;

4. fitting coefficients are linearly interpolated for cloudy days, and a clear sky curve is calculated also for these days, in order to evaluate the cloud forcing.

This is an iterative process that involves a first guess of the required parameters for a rough classification of the clear sky data and fitting: new coefficients are then used in a second iteration and so on, until convergence of derived coefficients occurs.

### 3.1.1 Detection metod

Cloudy sky exhibits shortwave features that clear sky does not, which can be used to separate the two situation within the dataset. Four tests are used to eliminate data that occur under cloudy skies.

The first test ensures that the normalized total shortwave irradiance ($F_N = F/\mu$, where $\mu = cos\theta$) falls inside a certain range: maximum and minimum limits are set according to the characteristics of the measurement site. In this way obvious periods of cloudiness are eliminated, along with data at solar zenith angles greater than approximately $80^o$ (for the $\mu = cos\theta$ normalization).

The second test concerns the diffuse component of the incoming radiation, that significantly increases in presence of clouds. A limit is imposed to the clear sky diffuse irradiance, so that it matches the tipical climatological value of the instrument location: all the data that fall above this limit are then eliminated. This test detects obvious periods of cloudiness, including or not thick haze or subvisual cirrus clouds, depending on the operator choice of the limit.

The third test checks the temporal change of the total shortwave irradiance: for clear sky this change is small over short periods of time with respect to changes due to cloud effects. The value $\Delta F/\Delta t$ is compared to the change of the top-of-atmosphere irradiance which reaches its maximum at $\theta = 90^o$: based on this, a validity range is defined, so that only values falling in it are kept. This test is helpful in maintaining high solar zenith angle data (usually eliminated by the first test) because it considers that at longer atmospheric path lengths the insolation is small, so that $\Delta F/\Delta t$ is also small.

The fourth test uses the variability of normalized diffuse ratio (defined as the diffuse shortwave irradiance divided by the total shortwave irradiance, normalized with $\mu$) to detect optically thin clouds: in fact this parameter is sensitive to small changes both in the diffuse and direct shortwave components. Authors point out the importance of the choice of the limit for clear sky running standard deviation of normalized diffuse ratio, because it strongly influences the number of data detected as clear: too low values cause an underestimation (interpreting system noise as cloudy conditions), and vice versa. They find that values between 0.001 and 0.0015 work well for the majority of the systems.

The tests' tresholds are listed in table 3.1.

Only data that pass all the tests are classified as clear and are used in the next step. It must be pointed out that measurements that meet all specified requirements are deemed representative of clear-sky measurements for a field of view of $160^o$, not $180^o$, because of the cosine response error of the instruments that increases with solar zenith angle: we will see that this limitation represents a problem for clear-sky detection in particular during last-first sunrise months (August/September and April), when solar zenith angles are higher than $80^o$.

### 3.1.2 Empirical fit for clear sky

The primary factor that determines the magnitude of the diurnal cycle of downwelling shortwave irradiance for clear sky is the solar zenith angle. Long and Ackerman (2000) found that a simple power law equation in the form

$$Y = a\mu^b \tag{3.1}$$

well represents clear-sky conditions. Equation 3.1 can be written as

$$Y = S_0 AU a' \mu(\mu^{b-1}) \tag{3.2}$$

where $S_0$=1367 W/m$^2$ is the solar constant and AU is the Sun-Earth distance correction. This form evidences better the rough meaning of the terms a and b; according to the authors, $a$ represents the clear-sky irradiace for $\theta = 0^o$ and includes such effects as the aerosol and column water vapor amounts, the mean Earth-Sun distance, and radiometer calibration; $b$ includes instrumental effects such as the radiometer cosine response.

Data identified as clear by the four tests are fitted using the equation 3.1. Daily coefficients for both total and diffuse component (and by subtraction for the direct one) can be calculated only if a sufficient number of clear-sky values spanning a significant range of solar zenith angles is found on that day. A minimum number of identified clear-sky measurements for fitting has should be set; whether this requirement is never satisfied during the period (e.g. tropical climate sites which present persistent cloudiness or high latitude sites where the sun has a low elevation for the most of the day) an average value for the coefficients is estimated from the available data. When instead daily coefficients are determined for clear days, they can be linearly interpolated for cloudy days. Authors showed that ignoring ancillary input of the atmospheric state variables in operating the interpolation, produces uncertainties in the resulting irradiance within the estimated uncertainties of the radiometer used.

Obtained coefficients must meet some empirical constraints, otherwise are recalculated.

At the end of this step a series of daily coefficients $a$ and $b$ are available for the entire period, and are used to evaluate clear sky shortwave fluxes: these clear-sky

values can be compared to the measured values to calculate the effect of clouds on radiation.

We show two examples of the result of the fit for global and diffuse irradiance for a cloudless day (21-12-2014) and for a partially cloudy day (21-11-2014) in figure 3.1. Function 3.1 perfectly match the measurements in the first plot; in the second, negative cloud effect is evident for the global irradiance, whereas positive cloud effect occurr in the diffuse component.

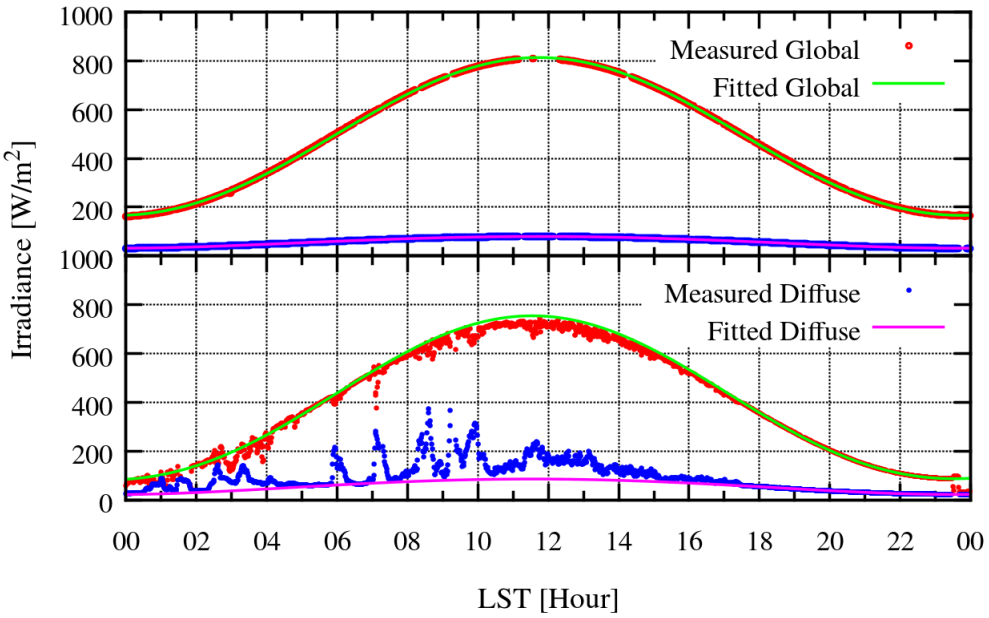


Figure 3.1: Comparison between measured and fitted global and diffuse irradiance for day 21-12-2014 (upper part) and day 21-11-2014 (lower part). The first is an example of a typical irradiance trend for cloudless sky, the second shows the effects of clouds.

## 3.2 Shortwave data analysis

We ran Long script in order to obtain daily clear-sky coefficients for our dataset. It is a FORTRAN77 code that requires an input file and a configuration file:

- the input file must contain columns with 1-minute irradiance data (total, direct and diffuse component); our input data file also includes the sun azimuth and elevation angles, the downwelling longwave irradiance, and the upwelling shortwave and longwave irradiance;

- the configuration file contains all the information the algorithm needs to perform its calculations, e.g. the clear sky tests tresholds, the coordinates of the site (to calculate $\theta$), infos about the date/time format, etc.

It is recommended to run the code twice, in this way the first run generates a set of parameters suitable for our particular climate regime and instrumentation, that can be used as a starting point in the second run.

The main output of the code gives us the following information:

- daily a and b coefficients for diffuse ratio, global irradiance, sum irradiance (obtained adding the diffuse and direct component) and albedo;

- one-minute data reporting date and time (GMT and LST), $\mu$, Earth-Sun distance correction, measured and clear-sky downwelling global SW, diffuse SW, direct SW and sum SW, cloud forcing for every component of radiation (computed as measured minus fitted value), a series of flags that identify ″bad data″, derived from an automated quality check performed by the algorithm, a ″clear-sky flag″, albedo (computed as the shortwave upwelling irradiance divided by the shortwave global downwelling irradiance), and all the remaining data contained in the input file.

**Configuration file** In table 3.1 the principal values we put in the configuration file are listed; most of them have been chosen empirically, sometimes adusting the initial evaluation made by the authors to better reproduce the characteristics of our dataset (e.g. the minimum number of minutes necessary to detect clear days has been reduced from 120 to 90, to deal with the Antarctic shortening of the days and low sun elevation; for the same reason the maximum limit for diffuse shortwave irradiance has been set to 200 W/m$^2$, instead of 150 W/m$^2$).

| | |
|---|---|
| Minimum number of 1-min data detected as clear in a diurnal cycle for that day to be used for the fitting | 90 |
| Number of minutes of data for the running standard deviation used to detect clear sky | 11 |
| Normalized diffuse ratio standard deviation limit | 0.0012 |
| First guess of b parameter (typical average) | 1.12 |
| Low limit for total SW irradiance [W/m$^2$] | 1 |
| Clear-sky maximum limit for diffuse irradiance [W/m$^2$] | 200 |

Table 3.1: Values used in the clear sky detection algorithm. See also Long and Ackermann (2000).

### 3.2.1 Cloudiness analysis

As an output of the algorithm we also obtain data useful to characterize the cloudiness of the site, such as the number of dayligth data points par day along with the number of detected clear sky data. We used these results to obtain a rough information about the cloudiness at Dome C, keeping in mind that bad data doesn't always correspond to cloudy sky.

In figure 3.2 the daily number of total and clear-sky data are shown for the period August 2007/April 2015: missing points before February 2008 are a consequence of the lack of good direct and diffuse irradiance data, that prevented the algorithm from performing the computation. The maximum number of daylight minutes during summer months is 1440. Missing points are a consequence of the initial data quality check. From this plot we can get an idea of the general trend, namely a reduction of the relative number of clear-sky detected points per day during mid-seasons for all the years. Notice that no day was detected as completely cloudless, because the algorithm tends to eliminate low sun elevation measurements. This effect is enhanced at Dome C where maximum sun elevation is low during the major part of the year.

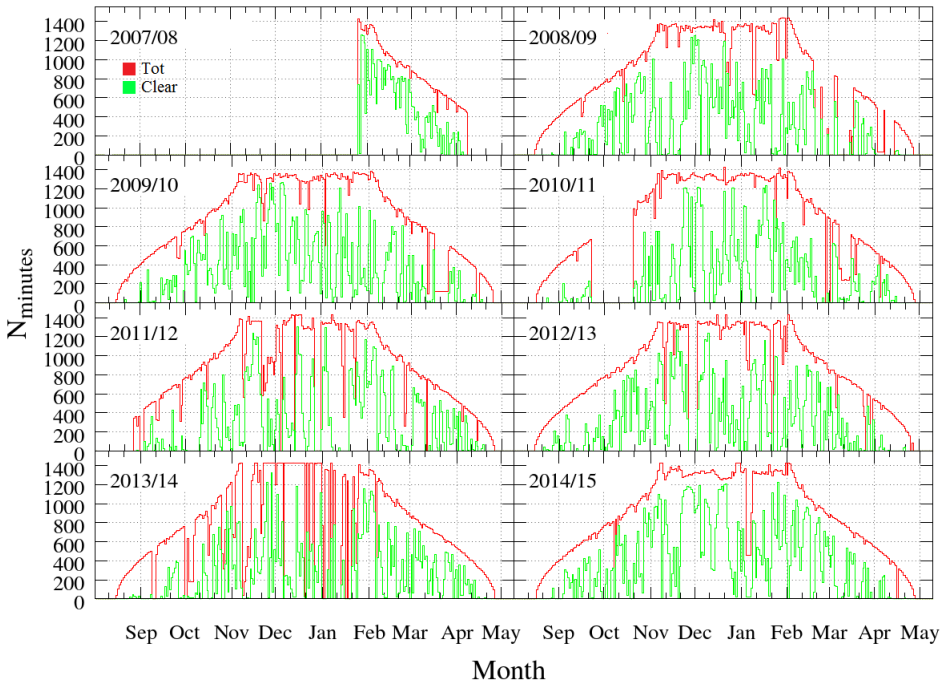


Figure 3.2: Total number of daylight minutes per day (red) and clear minutes as detected by the algorithm (green). All the years in our dataset are shown, excepted August and September 2015.

We calculated monthly means of the cloud occurence, defined as:

$$CO = \frac{N_{tot} - N_{clear}}{N_{tot}} \tag{3.3}$$

where $N_{tot}$ is the number of daylight minutes and $N_{clear}$ is the number of clear sky minutes, and plotted the results in figure 3.3. The time frame is the same of figure 3.2. For all the years montly mean cloud occurence diminishes from around 0.8 in September to values between 0.4 and 0.6 in November, except for 2008/09 where it presents a saw thoot shape, oscillating between 0.8 and 0.5. For 2009/10, 2012/13 and 2014/15 cases cloud occurence increases again from December to March, while for 2011/12 and 2013/14 it remains fairly constant around 0.6; in 2010/11 there is a downward trend until January and then a rise. All average values fall in the range 0.4-1, while an higher variability is observed from day to day.

In figure 3.4 we plotted together all the monthly mean cloud occurences

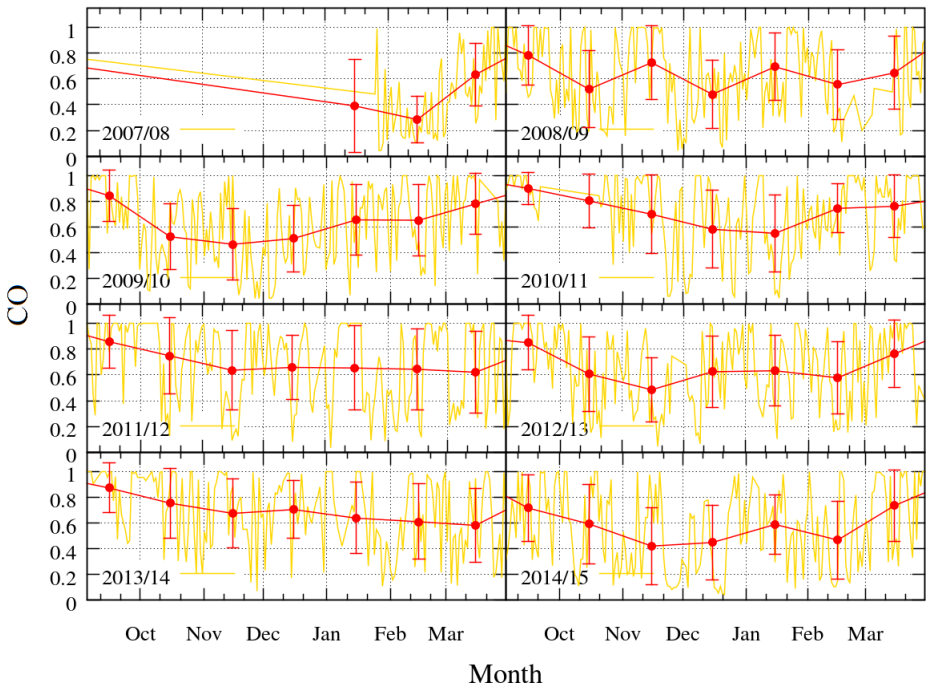


Figure 3.3: Daily (gold) and monthly mean (red) cloud occurence for all our period of interest (only August and September 2015 are not shown), divided by year. Error bars represent the standard deviations of the computed means.

calculated for all the years, along with an average of the monthly means (red line) in order to point out a not only a seasonal, bat also a climatological characterization of cloudiness. The lowest number of clear sky data is observed in September and March, with a maximum cloud occurrence of 80%/90%. Minimum values of 55% occurr on December and February, with a slight increase observed in January.

### 3.2.2 Coefficient analysis

We obtained $a$ and $b$ constants for every day of our period of interest (from April 2007 to September 2015), except for the Winter days, characterized by absence of Sun (approximately from 01/05 to 10/08 of every year). The algorithm fits the values for the global irradiance, the diffuse irradiance and the diffuse plus direct

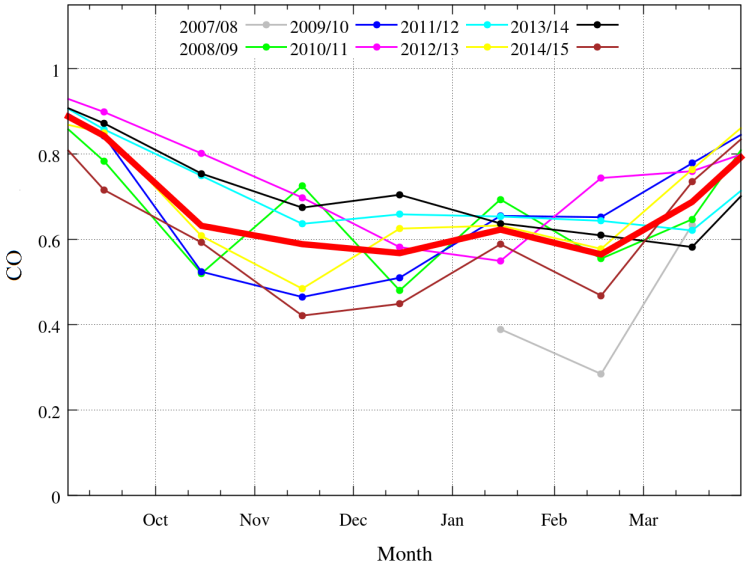


Figure 3.4: Montly mean cloud fraction computed with equation 3.3 for all the years in our dataset, along with a climatological mean (red).

irradiance; we will call this last component sum irradiance, and related coefficients $a_+$ and $b_+$.

Some words should be spent on the physical meaning of the two constants: as we've already pointed out in section 1.1.2, according to Long and Ackerman (2000), $a$ accounts for atmospheric effects and $b$ for instrumental errors. However we found out that this separation is not so net. In fact, if $a$ represents the attenuation of the radiation due to atmospheric absorption, it must be a function of the solar constant, the Sun-Earth distance, the latitude, the aerosol, water vapor and ozone content; we include these quantities in the definition of effective transmittance t($\mu$)):

$$t(\mu) = \frac{a\mu^b}{S_0 AU\mu} \tag{3.4}$$

In figure 3.5 we show the scatter plot $a$ vs $b$ and $a_+$ vs $b_+$ calculated only for clear days; isolines of effective transmittance calculated for four solar zenith angles ($50^o$,$60^o$,$70^o$ and $80^o$) using equation 3.4 are also included: t($\mu$) represents the attenuation of solar irradiance due to atmospheric gases and aerosol absorption, as it is the ratio of fitted groud irradiance (that for clear days is equal to the

measured one) and theorical top-of-atmosphere irradiance. An approximate linear correlation between a and b is evident. Figure 3.5 shows that at constant solar zenith angle many pairs of [a,b] can provide the same global transmittance. The retrieved parameters are valid in the range of angles on which the diurnal fit has been performed: this ensures that the irradiance value given by equation 3.1 will be always lower than $S_0$.

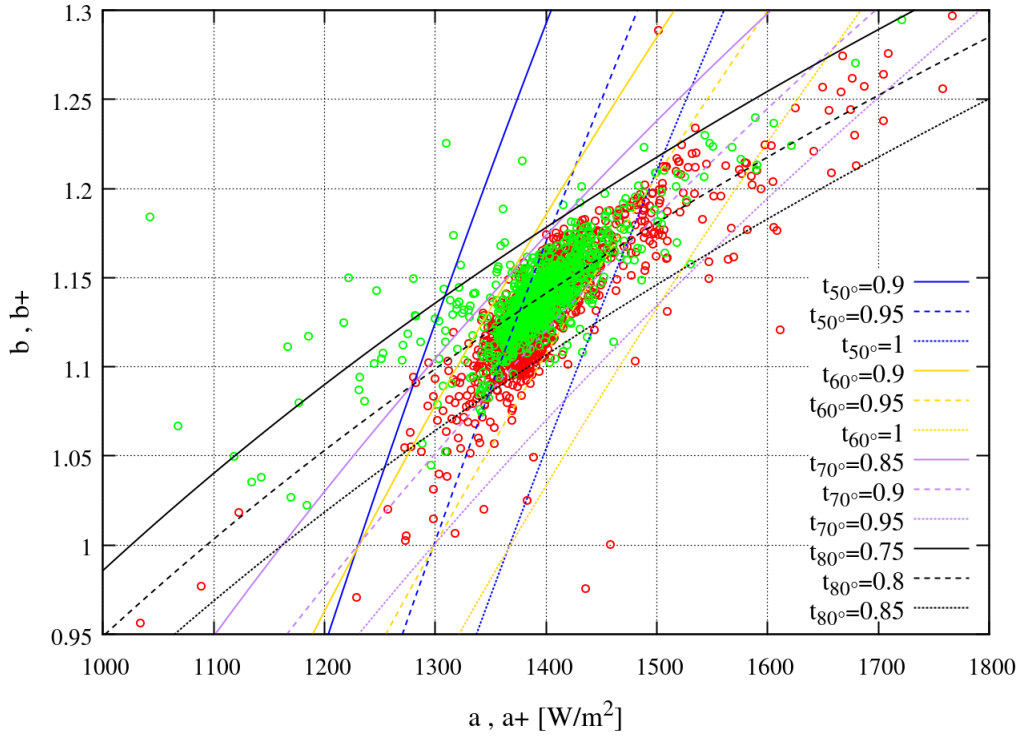


Figure 3.5: Scatter plot between fitting coefficients $a$, $b$, $a_+$ and $b_+$ calculated for clear days, and isolines of transmittace calculated for fixed solar zenith angles using equation 3.4 (e.g. $t_{50^o}$ stands for transmittance calculated at $\theta$=50$^o$).

We computed the seasonal frequency histograms of the clear-days coefficients to analyze their annual behavior, both for the global and sum irradiance. Results are shown in figures 3.6 and 3.7.

Summer $a$ values present a narrower distribution than Autumn and Spring ones, with a frequency peak of 18% in correspondence of 1370 W/m$^2$; the same

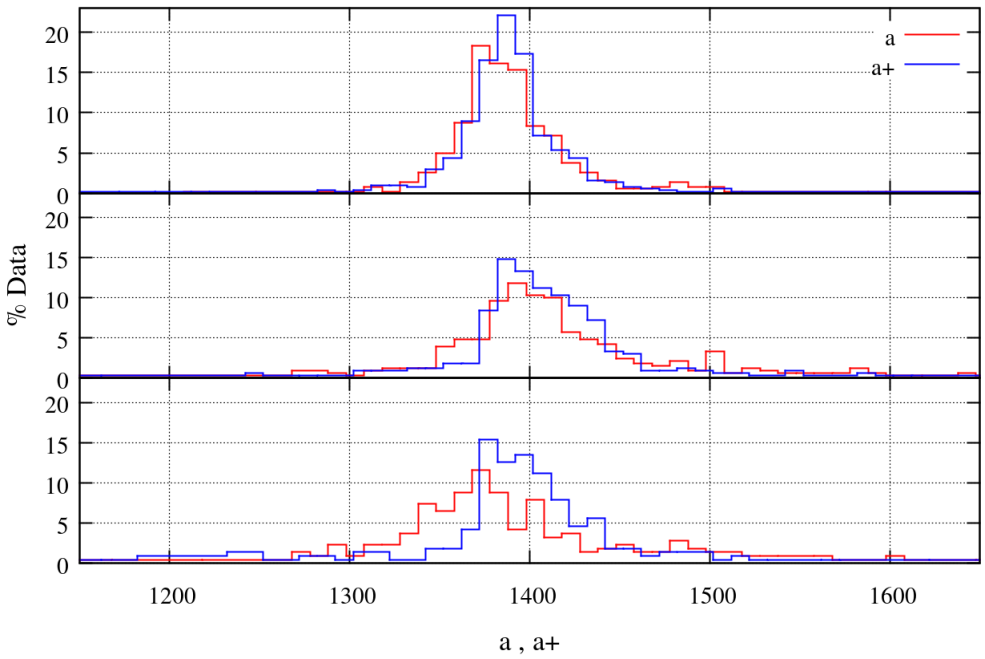


Figure 3.6: Frequency histogram for $a$ and $a_+$ parameters. The first plot refers to Austral Summer season (November, December, January), the second one to Autumn (February, March, April) and the third one to Spring season (August, September,October).

happens for $a_+$, with a more symmetric Summer distribution with a peak of 22% in correspondence of 1380 W/m$^2$. The $b$ coefficient doesn't present the same features, in fact all the distributions are spread without so evident maxima. The $b_+$ summer distribution is almost symmetric, with a well defined peak of 18% in correspondence of 1.13; autumn and spring distributions show a more irregular behavior. These features are probably due to the fact that a major number of clear sky data are available in Summer (as mentioned in section 1.2.1). In the table **??** mean and standard deviations of the distributions are displayed, along with the total number of data considered.

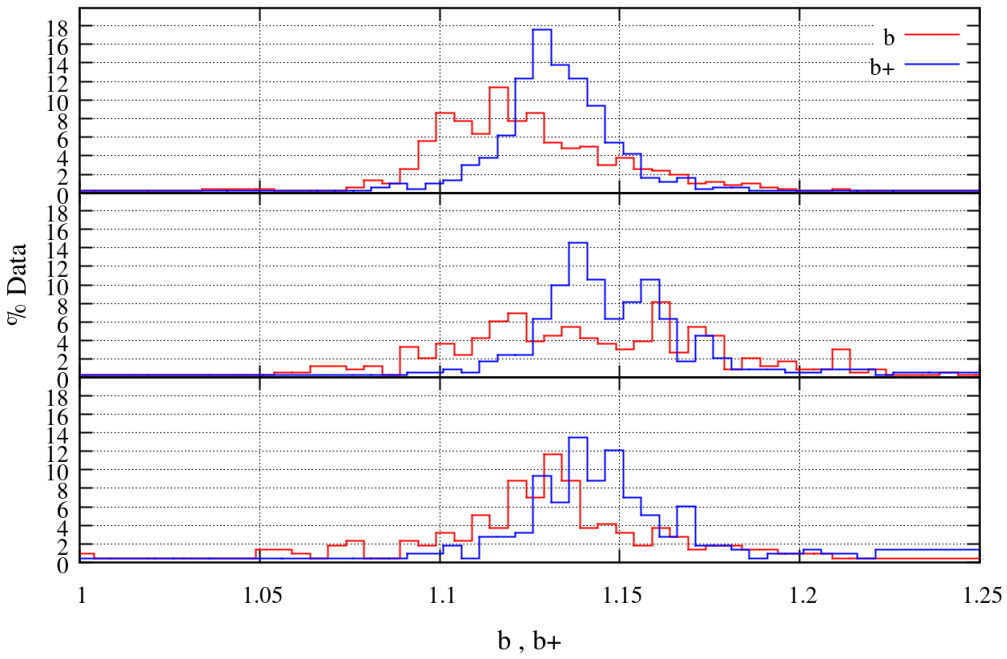


Figure 3.7: Frequency histogram for $b$ and $b_+$ parameters. The upper part refers to Austral Summer season (November, December, January), the central part to Autumn (February, March, April) and the lower part to Spring season (August, September,October).

| | $a$ | $a_+$ | $b$ | $b_+$ | $N_{tot}$ |
|---|---|---|---|---|---|
| Summer | 1400 ± 67 | 1394 ± 208 | 1.13 ± 0.04 | 1.13 ± 0.05 | 502 |
| Autumn | 1427 ± 93 | 1403 ± 87 | 1.14 ± 0.04 | 1.15 ± 0.04 | 331 |
| Spring | 1390 ± 116 | 1382 ± 115 | 1.12 ± 0.07 | 1.14 ± 0.04 | 215 |

Table 3.2: mean and standard deviations of the distributions of the four coefficients are displayed, along with the total number of data used.

### 3.2.3 Model errors

We estimated the differences between the above mentioned parametrization and measured irradiance for clear days, to check its ability in reproducing our data. In Long and Ackerman (2000) authors demonstrated that the model errors

fell within instrumental errors: however they tested the model on datasets from places which climates were different from the cold and dry Antarctic plateau.

For every irradiance data (global, diffuse and sum) detected as clear, we calculated the absolute value of the difference between the measurement and the fit; their mean and standard deviations are shown in the next table:

| Global [W/m$^2$] | Sum [W/m$^2$] | Diffuse [W/m$^2$] |
|---|---|---|
| 2.25 ± 2.94 | 2.42 ± 4.12 | 1.26 ± 3.00 |

In figure 3.8 the frequency distributions of the differences are shown: they are all symmetric around zero, and the maority of the values fall within the instrumental error of approximately 5 W/m$^2$.

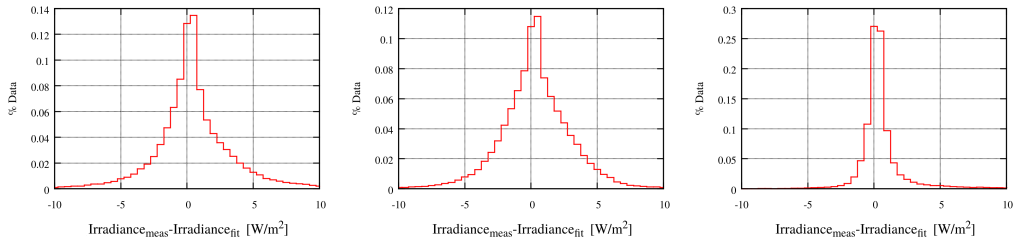


Figure 3.8: Frequency distributions of the difference between modeled and measured irradiance, for global, sum and diffuse component respectively.

### 3.2.4 Calculation of cloud forcing

We define the cloud forcing on the shortwave downwelling irradiance as:

$$CF_{\downarrow,SW} = F_{\downarrow,SW,measured} - F^{clear}_{\downarrow,SW} \tag{3.5}$$

where $F^{clear}_{\downarrow,SW} = a\mu^b$ ("clear" stands for clear sky conditions), and the normalized cloud forcing on the shortwave downwelling irradiance as:

$$CF_{\downarrow,SW,N} = \frac{F_{\downarrow,SW,measured} - F^{clear}_{\downarrow,SW}}{F^{clear}_{\downarrow,SW}} \quad . \tag{3.6}$$

We computed these quantities for all the components of the solar irradiance, namely the global, direct and diffuse part to estimate the cloud effect on radiation

during the day. Then we calculated the monthly averages. Results are shown in figures 3.9, 3.10 and 3.11.

We excluded from the calculations all data referred to solar zenith angles higher than $85^o$: this limitation removes August, September and April measurements, all taken at solar elevations so low that the algorithm can't detect successive clear days, even if no clouds were present, and consequently interpolated the coefficients from the last available ones, introducing additional errors in the cloud forcing values. Eliminating this low irradiance values should not affect too much our results.

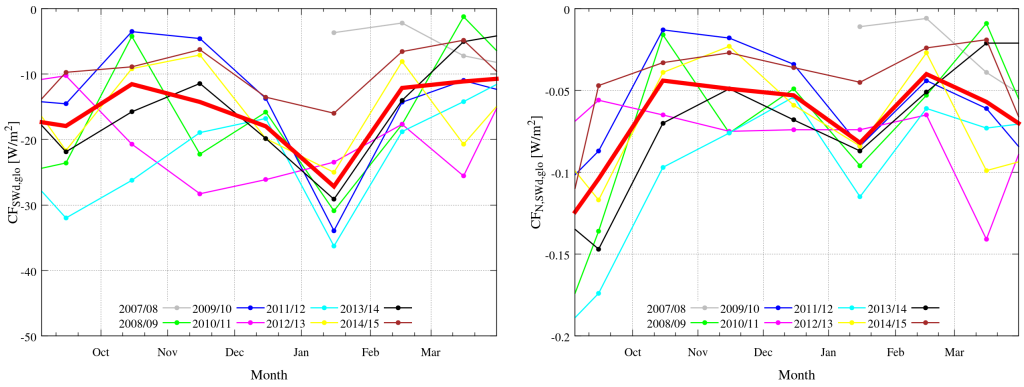


Figure 3.9: Monthly means of cloud for and normalized cloud forcing respectively for the global irradiance. Thin lines are referred to the different years, thick red line is the ″climatological″ mean.

Figure 3.9 shows the cloud forcing on the global irradiance calculated for all the years plus the monthly climatological mean. The normalized cloud forcing is calculated to highlight the relative effect of clouds on the incoming radiation (a CF of -50 W/m$^2$ is not as significant in January as it could be in September because total incoming radiation is lower in magnitude). CF is always negative, as it is expected, resulting from an attenuation of the direct irradiance on one side (negative cloud effect) which is stronger then the enhancements (positive cloud effect). For what concernes the climatological mean, a maximum of -30 W/m$^2$ is found in January, with all other values falling below -10 W/m$^2$. All the years present quite different features, and no typical trend is identified. Direct

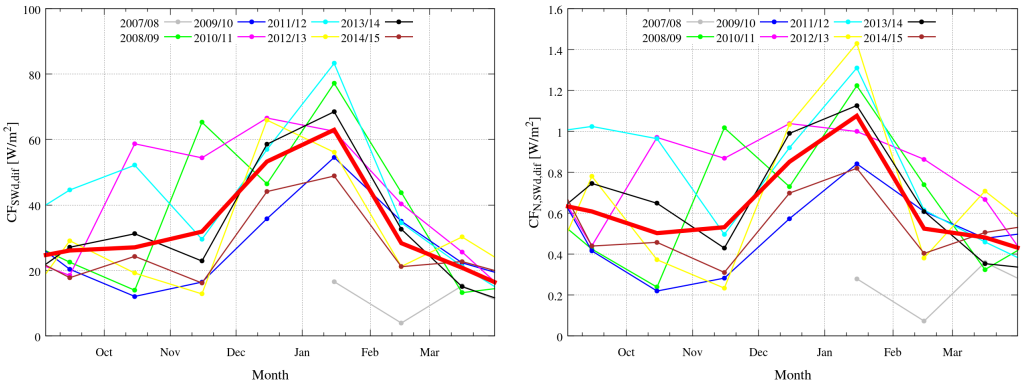


Figure 3.10: Monthly means of cloud forcing and normalized cloud forcing respectively for the diffuse irradiance. Thin lines are referred to the different years, thick red line is the ″climatological″ mean.

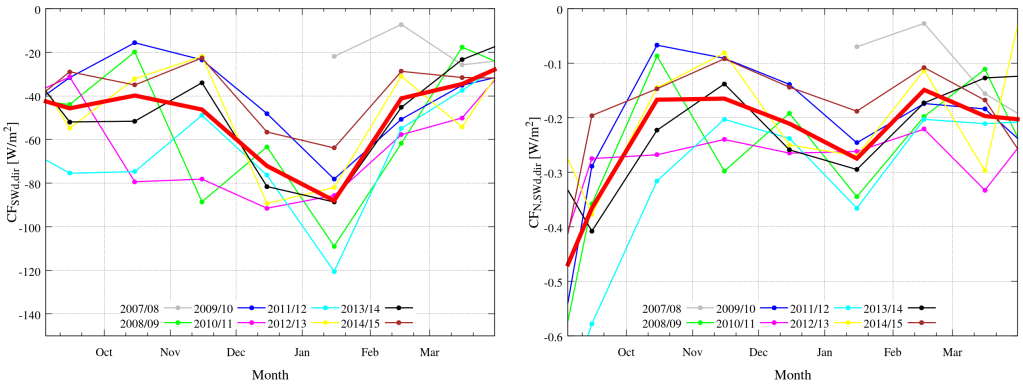


Figure 3.11: Monthly means of cloud forcing and normalized cloud forcing respectively for the direct irradiance. Thin lines are referred to the different years, thick red line is the ″climatological″ mean.

cloud forcing (reported in figure 3.11) usually have a well defined peak in Summer season, with maximum values spanning from about 40 W/m$^2$ to 80 W/m$^2$, with a climatological mean of 60 W/m$^2$; similarly the diffuse effect (reported in figure 3.10) is higher in magnitude during Summer, with a peak of about -60 W/m$^2$. We remark that all these average results present high standard deviations due to the daily variability of the quantity that we are considering; furthermore, mid season values are affected by an higher error due to the interpolation of the coefficients.

# Chapter 4

# Cloud forcing on shortwave upwelling irradiance

In this chapter we will discuss the cloud forcing on the shortwave upwelling irradiance. In order to calculate this forcing we need to parametrize the clear sky shortwave upwelling irradiance. The Long and Ackerman (2000) metodology can't be directly used as for the downwelling component, because it does not compute a fit for the upwelling irradiance. It instead calculates a fit for the albedo, defined as (Iqbal, 1983):

$$\alpha = \frac{F_{\uparrow,SW}}{F_{\downarrow,SW}} \tag{4.1}$$

where $F_{\downarrow}$ and $F_{\uparrow}$ are downwelling and upwelling shortwave irradiance. This is the planetary albedo plus the contribution of irradiance scattered by the atmosphere and detected by the instrument. Equation 4.1 can be inverted to write the clear sky upwelling irradiance as a function of clear sky albedo and downwelling irradiance:

$$F^{clear}_{\uparrow,SW} = \alpha^{clear} F^{clear}_{\downarrow,SW} \tag{4.2}$$

where $F^{clear}_{\downarrow}$ is the clear-sky function for downwelling irradiance parametrized in the previous chapter as $a\mu^b$. Hence the cloud forcing computation is straightforward:

$$CF_{\uparrow,SW} = F_{\uparrow,SW,measured} - F^{clear}_{\uparrow,SW} \quad . \tag{4.3}$$

The albedo curve $\alpha^{clear}$ at Dome C presents particular features that make the Long and Ackerman's parametrization not sufficiently accurate. This fact will

be analyzed in a more detailed way in the next sections, and a more complex parametrization will be proposed.

## 4.1 Albedo ad Dome C

The ground at Dome C is covered with snow for the whole year and melting is not a prominent phenomenon even during Summer because of the low ground temperatures, that even during Antarctic Summer don't exceed -20$^o$C. A slight metamorphism of the snow can certainly occurr (Pirazzini, 2004), but it is not easily determined from our broadband irradiance data. In figure 4.1 the spectral dependence of the snow albedo is shown for snow at different ages: albedo is a function of the time passed from the snow deposition on the surface. The older the snow, the less reflective it is; as it starts to melt there is a noticeable drop in albedo. The visible spectral albedo is almost uniform, and diminishes for wavelength greater than 800 nm due to the solid ice absorption. Hence at our site we expect clear sky albedo ranging between 0.8 and 1.

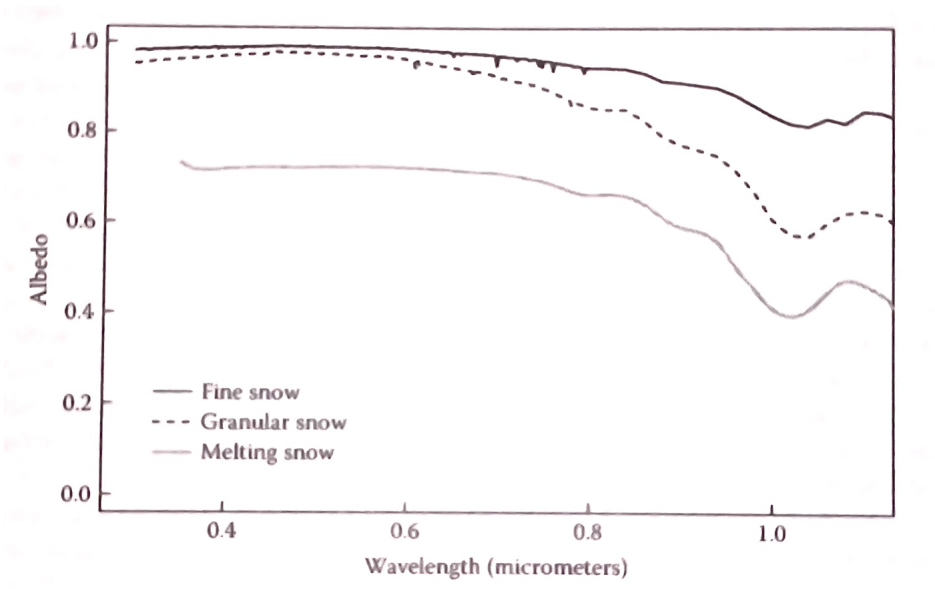


Figure 4.1: Snow albedo spectral dependence for differently types of snow (from Vignola et al., *Solar and infrared radiation measurements*, 2012).

Broadband albedo, which we are going to study, depends on cloud cover conditions and on the radiation incident angle: it remains fairly constant in overcast days because incident diffuse radiation is isotropic. In a cloudless day, typical albedo is larger at high solar zenith angles and progressively decreases until midday, according to Fresnel laws of reflection: light at large incident angles has an higher probability of escaping from the snow grains without being absorbed, while normal incidence light penetrates deeper into the snow and is more likely trapped. But this happens if the snow surface is smooth, uniform and horizontal, and that's not our case; in fact we observed that the diurnal variation of $\alpha^{clear}$ at Dome C was highly variable and irregular.

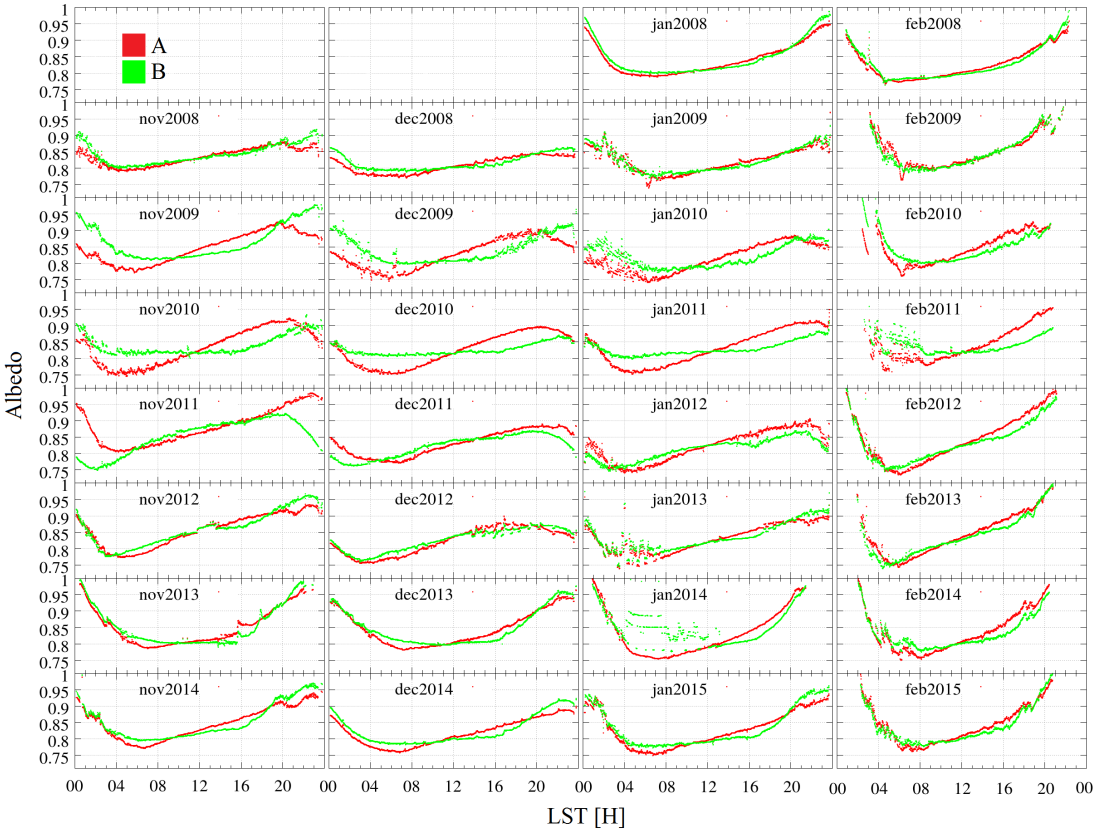


Figure 4.2: Clear sky albedo measured at Dome C by both the instruments ($p_A$ and $p_B$) for Summer months during our measurements period. Every point is a 1-minute average of all detected clear sky data on that month.

In figure 4.2 we plotted the 1-minute average of all the clear sky measurements of albedo detected during the months of November, December, January and February, for all the years in our dataset. The red curve refers to instrument $p_A$ and the green one refers to instrument $p_B$. The majority of data fall between 0.8 and 1 as expected. The main feature of $p_A$ curves is a marked asimmetry between morning and afternoon for almost the whole dataset: all profiles have a minimum of around 0.8 between 4:00 and 8:00, increase until 0.9 at about 20:00 and then slightly decrease (except for February cases where we don't have data between 20:00 and 24:00 due to too low solar elevation). For January and February 2008, and for November and December 2013 the profile is more symmetrical with respect noon, with maxima at midnight.

On the contrary, the $p_B$ curve of figure 4.2 generally presents a trend that is symmetric between morning and afternoon and doesn't significantly change for most of the period, namely from January 2008 to February 2011, and from November 2013 to February 2015. The trend is more similar to the $p_A$ one from December 2011 to February 2013.

The morning/afternoon differences relative the two instruments are well summarized in figure 4.3. The three histograms show total clear-sky albedo measurements, morning measurements and afternoon measurements, considering data for the whole period. For the $p_A$ (upper part) the morning and afternoon distributions are shifted with respect to the total one (that is almost symmetrical around 0.82), with the first having a peak around 0.77, the second around 0.84. For the B instrument the shifting is not so marked, with all the three distributions' peaks falling between 0.8 and 0.85.

Snow albedo irregular daily trend has been investigated from several authors, and different explanations to albedo behaviour are found in literature. Some of them are (Pirazzini, 2004):

- the metamorphism of the snow that takes place after its deposition tends to decrease the value of the albedo due to the change in the form of snow grains (as we have already observed in figure 4.1) until melting occurs. In Antarctic continent this is more likely to happen in Summer on the coastal

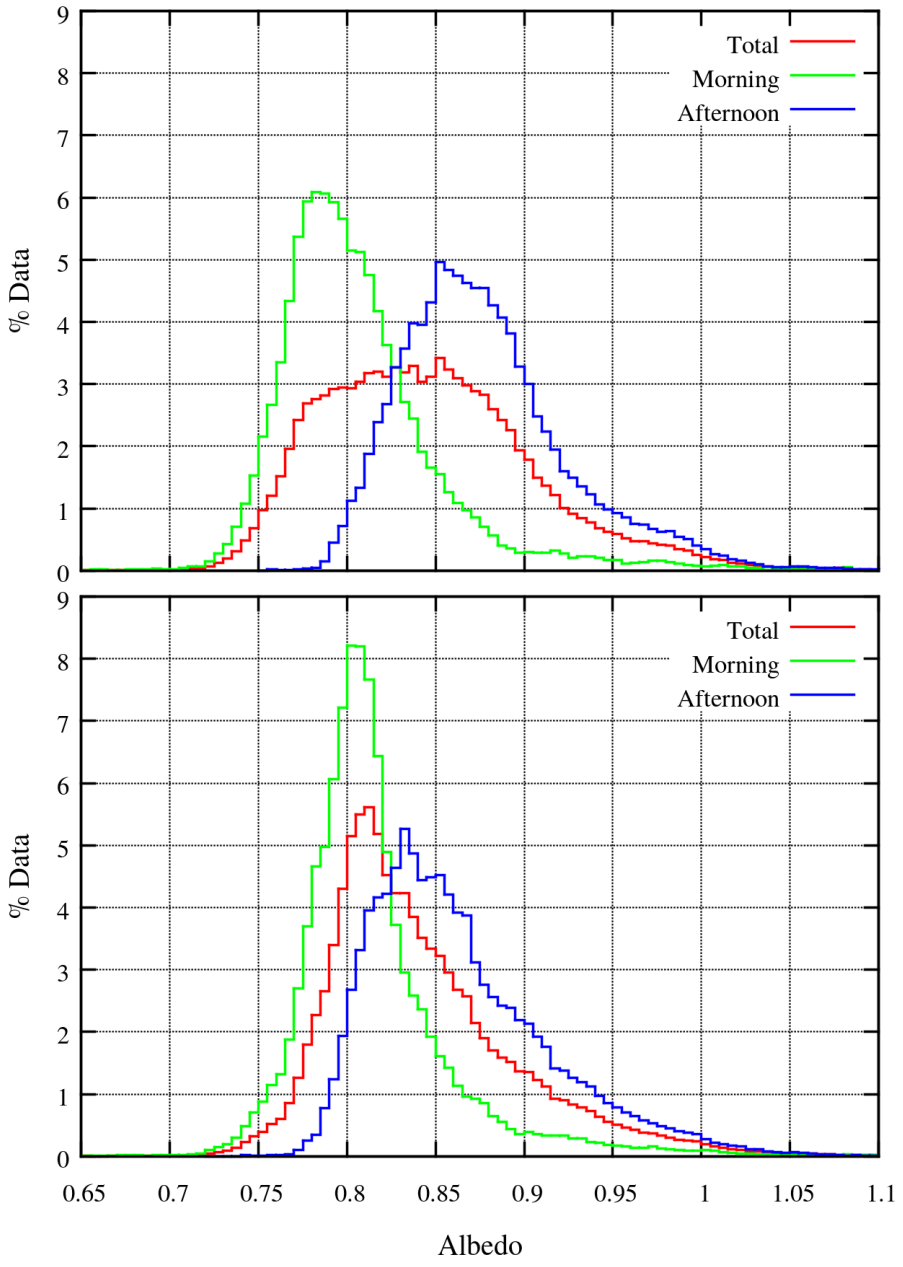


Figure 4.3: Frequency distributions of clear sky albedo calculated for instrument A (upper part) and B (lower part), considering all data, morning data and afternoon data.

region, while on the interior plateau metamorphism progresses more slowly due to lower surface temperatures: frost deposition and diamond-dust may

contribute to the change of the configuration of the ice crystals at the surface, consequently increasing albedo;

- wind effect on transport of snow and erosion of the surface can generate microscale or macroscale patterns, like little dunes or large sastrugi, which shadows influence the albedo value during the day depending on the position of the Sun;

- snow surfaces are far from being perfectly horizontal: they are often tilted with a certain angle and therefore the amount of ground incident radiation when the sun is in the downhill direction will be larger, causing the reflected irradiance to be dependent on the Sun's azimuth.

At Dome C no large patterns such as sastrugi are present on the field of view of the two down-facing pyranometers $p_A$ and $p_B$: in fact sastrugi are mainly due to strong katabatic winds that are not typical of the Antarctic plateau climate. The ground is irregular, and presents a certain inclination, that has been verified to be of approximately $2^o$. In the 8-years period covered by our dataset the snow profile certainly have changed. In particular, during Summer 2010/11 the cofiguration of the containers located in the proximity of the station has been modified: probably this altered the preferential way of accumulation of the snow due to wind under the rack. Looking at the albedo $p_B$ profile in figure 4.2, it is evident that something happened between Summer 2010/11 and Summer 2011/12, as it began to show a different shape, more similar to the $p_A$ one.

Excluding snow metamorphism and sastrugi effects as the main causes of the observed albedo trend (even if a certain influence can be present), we think that the explanation of it can be found in the inclination of the surface under the albedo rack and to the shading effects of the ground irregularities. The asymmetry between morning and afternoon can be explained in terms of azimuth dependence of the albedo, or, in other words, on where the Sun is with respect the inclination direction. However the marked differences in the trend of the two intruments is something still not perfectly understood.

## 4.2 Clear-sky albedo parametrization

### 4.2.1 Long and Ackerman's parametrization

As we have already mentioned, the clear sky detection algorithm we analyzed in the previous chapter, also calculated a fit for the albedo for cloudless days, and then interpolated the obtained coefficients for cloudy days.

The fitting function is of the type:

$$\alpha^{clear} = a_\alpha \mu^{b_\alpha} \tag{4.4}$$

where $\mu$=cos$\theta$. Equation 4.4 is a function of $\theta$ analogous to the one for the downwelling irradiance, with the difference that $b_\alpha$ is negative, so that higher values of albedo correspond to high solar zenith angles. However the function is symmetric with respect noon, so we suppose it won't reproduce in a satisfying way the albedo profile; better results are expected for p$_B$ instrument.

### 4.2.2 Azimuth parametrization

As already pointed out, the previous fit does not take into account the effect of the surface inclination and irregularities. In fact the $\mu$ term alone well represents the albedo trend only on a smooth horizontal snow surface. With the available data it is not possible to construct a theoretical model for surface reflectance, that should consider microphysical features of the snow along with a relation between the geometry of the surface and the Sun position. Hence we propose a more versatile parametrization of clear sky albedo introducing terms of an higher order in $\mu$, along with the azimuth dependence, to include and represent the above mentioned effects. We look for a parametric function in the form:

$$\alpha(\theta, \phi) = \frac{\alpha(\phi)}{\alpha(\phi_0)} \alpha(\theta, \phi_0) \tag{4.5}$$

where the normalized quantity $\frac{\alpha(\phi)}{\alpha(\phi_0)}$ accounts for the azimuth influence, and $\alpha(\theta, \phi_0)$ for the zenith angle.

The azimuth dependence can be expressed by a cosine series of the second order in $\phi$, that reflects the daily dependence on azimuth:

$$\alpha(\phi) = A + Bcos(\phi - \phi_0) + Ccos(2(\phi - \phi_0)) \tag{4.6}$$

where $\phi_0$=30$^o$ is the best fit parameter, that can be explained by the value of the angular position between the Sun and the ground inclination.

We approximated the solar zenith angle dependence with a second order polynomial in cos$\theta$, that is a simplified version of the snow reflectance parametrization found in Warren et al. (1998):

$$\alpha(\theta, \phi_0) = D + Ecos(\theta) + Fcos^2(\theta) \tag{4.7}$$

Figure 4.4 gives a visual interpretation of the described algorithm, being the red curve the albedo measured in a cloudless day (21 December 2014) plotted as a function of cos$\theta$, the green curve represents the fit calculated with equation 4.6, the blue curve the normalized $\alpha(\theta, \phi)/\alpha(\phi)$ and the purple curve the fit calculated with equation 4.7.

The resultant parametric function for the clear sky albedo is:

$$\alpha(\theta, \phi) = \frac{A + Bcos(\phi - \phi_0) + Ccos(2(\phi - \phi_0))}{A + B + C}(D+Ecos(\theta)+Fcos^2(\theta)) \quad . \tag{4.8}$$

The clear sky albedo calculated with equation 4.8 is plotted in figure 4.5 as a function of local standard time: it reproduces quite well the morning/afternoon asymmetry thanks to the introduction of the azimuth terms, whereas the $\mu$ terms account for other surface's irregularities.

Our parametrization depends on six adimensional coefficients, that should account for all the neglected influencing factors, such as snow microphysics or atmospheric composition.

We fit function 4.8 to all the clear days albedo data (from both instruments) and obtained daily sets of six clear-sky-coefficients for the whole period.

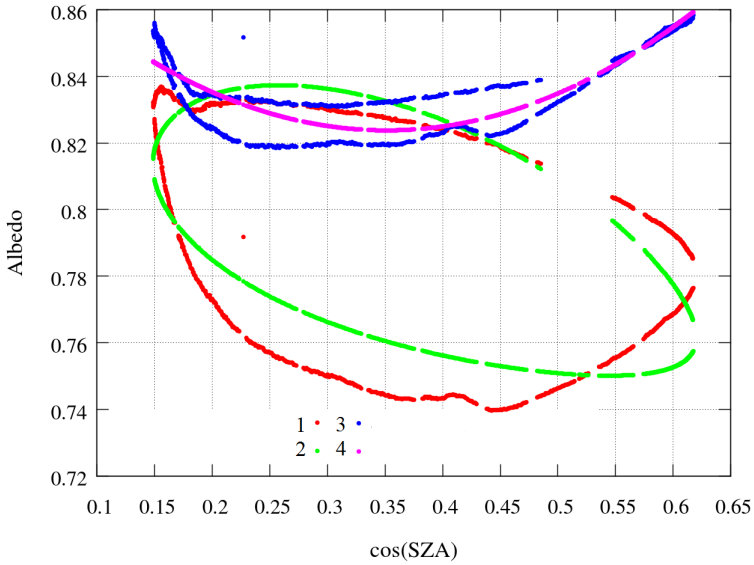


Figure 4.4: Measured and fitted daily albedo as a function of $\mu$. Data from 21 December 2014 are shown. The red curve is the measured albedo (1), the green curve the fit calculated with equation 4.6 (2), the blue curve the normalized $\alpha(\theta, \phi)/\alpha(\phi)$ (3) and the purple curve the fit calculated with equation 4.7 (4).

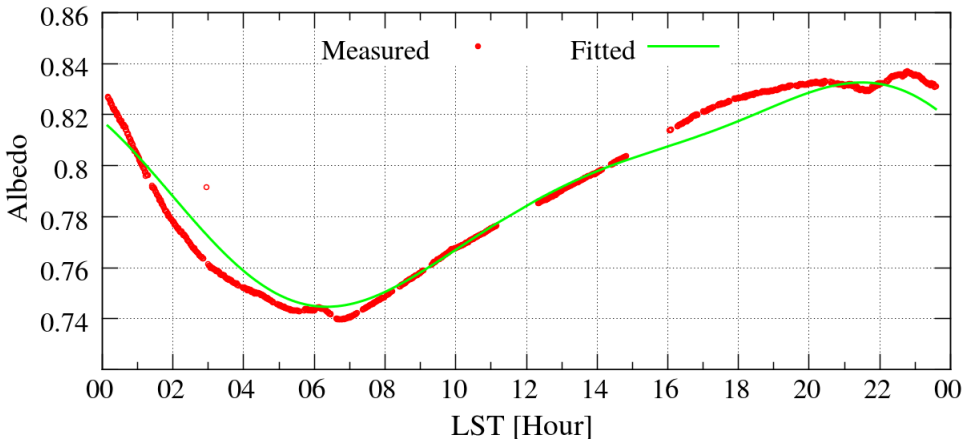


Figure 4.5: Measured and fitted daily albedo as a function of local standar time. Data from 21 December 2014 are shown.

### 4.2.3 Comparison between models

In order to visually check the behaviour of the two parametrizations, we tested them on a typical clear day from year 2010, when the differences between the two

instruments $p_A$ and $p_B$ were more marked. In the upper part of the two plots of figure 4.6 the albedo measured curve is displayed along with the fits calculated with equations 4.4 (green) and 4.8 (blue); the first plot is for $p_A$, while the second one is for $p_B$. In the lower part the absolute value of the differences between models and data are shown. For $p_A$ these are significantly higher for Long's fit, expecially in the first half of the day: at its maximum the green curve is five times the blue curve. For $p_B$, Long's parametrization works better then ours from 7 AM until the end of the day. It must be pointed out that azimuth parametrization tends to not work well for high solar zenith angles.

For all clear sky days we calculated both the albedo parametrizations using equations 4.4 and 4.8, and consequently the clear sky shortwave upwelling irradiance as

$$F_{\uparrow,SW}^{clear,L} = \alpha^{clear} F_{\downarrow,SW}^{clear} = (a_\alpha \mu^{b_\alpha})(a\mu^b) \quad . \tag{4.9}$$

and

$$F_{\uparrow,SW}^{clear,A} = \frac{A + Bcos(\phi - \phi_0) + Ccos(2(\phi - \phi_0))}{A + B + C}(D + Ecos(\theta) + Fcos^2(\theta))(a\mu^b) \tag{4.10}$$

where ″L″ stands for the Long parametrization and ″A″ stands for azimuth parametrization. Then we computed the differences between the measured and modeled albedo, and measured and modeled upwelling irradiance, for both parametrizations and instruments. Therefore we calculated the mean and standard deviations of these differences to quantify and compare the errors of the two models. Results are shown in the table 4.1.

For the Long parametrization, the maximum relative error on the albedo measured by $p_A$ is the 10%, whereas for $p_B$ is about 8%. As expected, this simplified parametrization works better for $p_B$ instrument, probably because it better matches its albedo daily profile. The mean error on the irradiance for the $p_A$ instrument is almost twice the $p_B$ one.

For azimuth parametrization, results are similar for the two instruments, indicating a certain adaptability of the model to different configurations. Errors and standard deviations are always lower than the ones obtained for the previous parametrization.

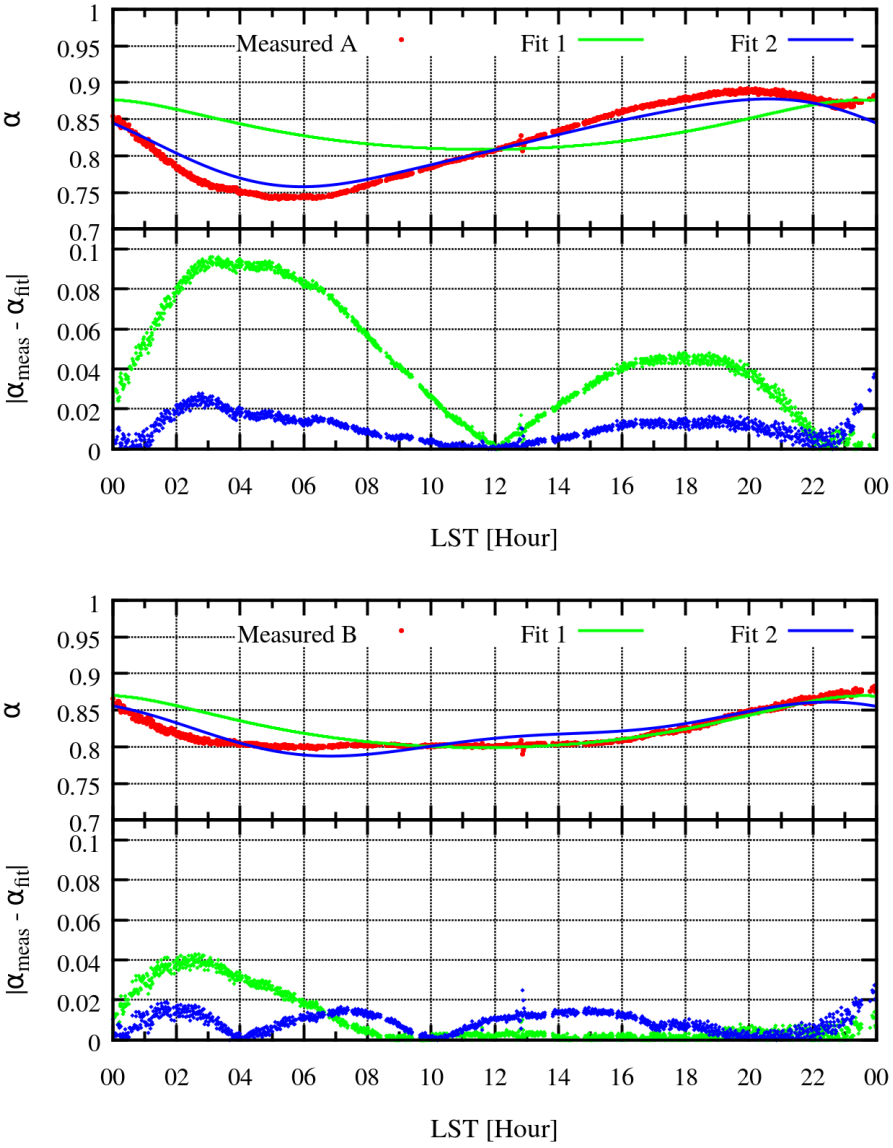


Figure 4.6: Measured and fitted clear sky albedo for data from 05/12/2010. The first plot is for $p_A$, the second one is for $p_B$. The red curve in plots' upper part is the measured albedo, green and blue curves are respectively the functions calculated with equations 4.4 (Long) and 4.8 (Azimuth). In the lower part of the plots, absolute value of model-data differences is shown.

| | $\lvert\alpha^{clear}_{measured}$ - $\alpha^{clear}_{param}\rvert$ | | $\lvert F^{clear}_{\uparrow,SW,measured}$ - $F^{clear}_{\uparrow,SW,param}\rvert$ [W/m$^2$] | |
|---|---|---|---|---|
| | L | A | L | A |
| $p_A$ | 0.032 ± 0.047 | 0.014 ± 0.026 | 10.081 ± 9.904 | 4.785 ± 5.384 |
| $p_B$ | 0.023 ± 0.044 | 0.015 ± 0.026 | 5.896 ± 6.620 | 5.157 ± 5.782 |

Table 4.1: Average and standard deviation of the absolute values of the differences between modeled and measured albedo and shortwave upwelling irradiance, for both the parametrizations.

## 4.3 Cloud forcing calculation

The coefficients needed for equations 4.4 and 4.8 for cloudy days were obtained linearly interpolating the available ones for cloudless days. As usual, the most problematic months were September and March, where few or no clear sky coefficients were available. August and April were eliminated a priori because of the Sun's low elevation.

Once the clear sky upwelling irradiance was computed for all the days in the dataset using 4.9 and 4.10, the cloud forcing was estimated using 4.3. Monthly mean CF is shown in figure 4.7 and 4.8, along with the climatological average.

Figure 4.7 presents the CF evaluated using Long and Ackerman's model for albedo for upwelling irradiance measured by $p_B$ instrument (best fit results). The climatological mean profile corresponds to the mean CF for the global downwelling irradiance (if more/less energy arrives in the system, more/less energy leaves it) but is lower in magnitude, with a relative minimum of -20 W/m$^2$ in January. Values of yearly profiles all fall between -30 W/m$^2$ and -5 W/m$^2$.

Figure 4.7 presents the CF evaluated using our model for albedo for upwelling irradiance measured by $p_A$ instrument (best fit results). The climatological mean is comparable to the one in the previous figure, with values always falling between -20 W/m$^2$ and -5 W/m$^2$, but sloghtly lower in magnitude. In September a difference of about 10 W/m$^2$ is observed. September 2009 and March 2008 and 2009 mean forcing are found to be positive: these are not reliable results, as on the average, the

cloud effect on the shortwave irradiance must be negative. This is probably due to the sensitivity of our parametrization to the uncertainties that arise performing the interpolation of the six coefficient in periods where no clear days are detected. At high solar zenith angles, Long parametrization is more likely to be correct, whereas we are more confident of our results for months from October to February.

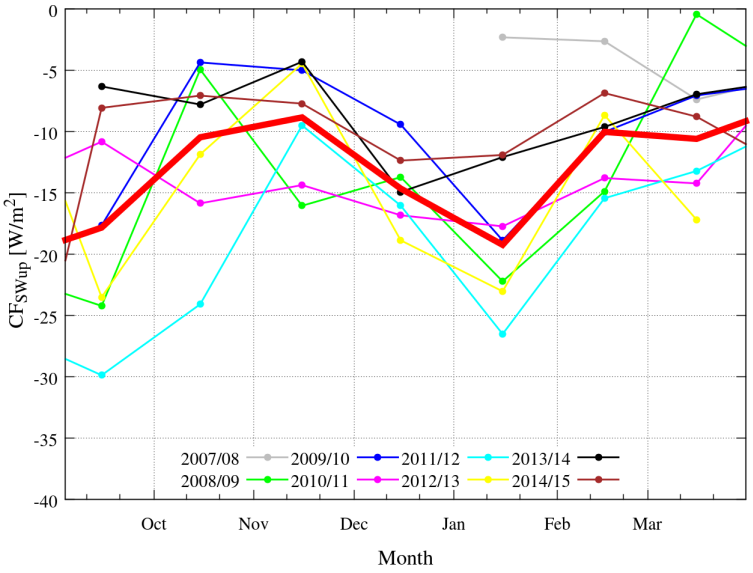


Figure 4.7: Monthly mean of cloud forcing for $p_B$ shortwave upwelling irradiance evaluated using Long and Ackerman's model for albedo. The thick red line is the climatological mean.

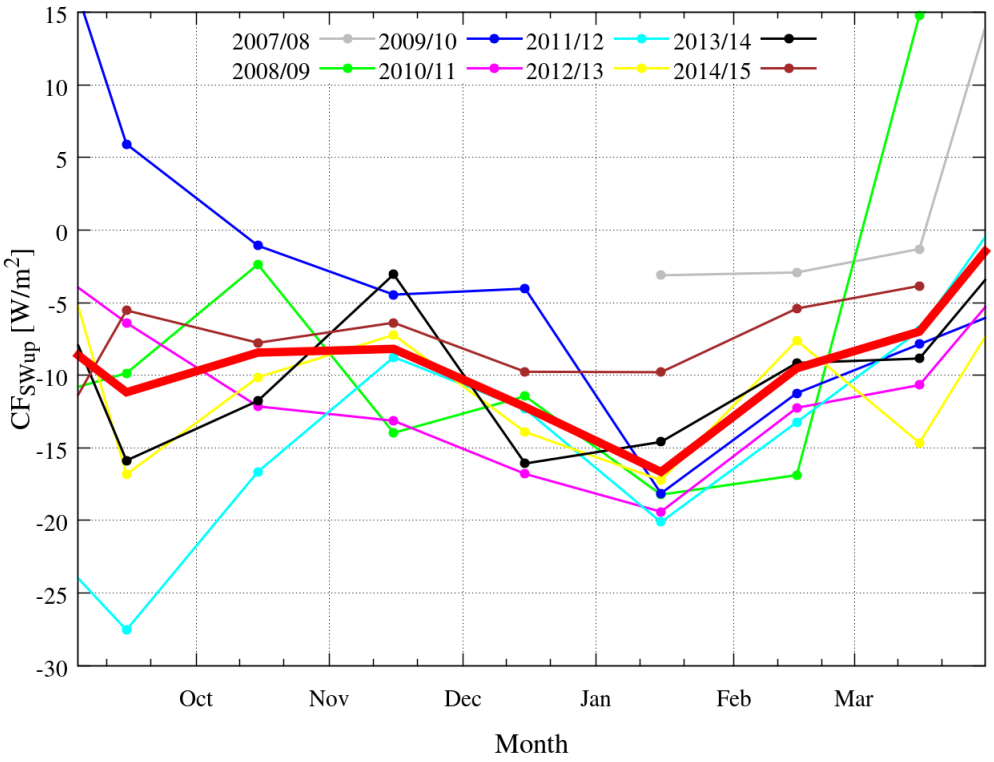


Figure 4.8: Monthly mean of cloud radiative forcing for $p_A$ shortwave upwelling irradiance evaluated using our model for albedo. The thick red line is the climatological mean.

# Chapter 5

# Cloud forcing on longwave irradiance

In this chapter we evaluate the effect of the clouds on longwave irradiance, firstly for the downwelling and then for the upwelling component.

## 5.1 Downwelling irradiance parametrization

Clouds are strong emitters in the mid and far infrared (IR) region of the electromagnetic spectrum: we expect the overall effect to be positive because liquid and solid water emits more in IR than water vapour does.

The CF can be estimated for both daytime and nighttime data.

To compute the cloud forcing we have to parametrize clear sky atmospheric emissivity $\epsilon_{clear}$ to express the longwave downwelling irradiance by means of the Stefan-Boltzmann law

$$F_{LW}^{clear} = \epsilon^{clear}(T)\sigma T^4 \tag{5.1}$$

where where $\epsilon_{clear}$(T) depends on the effective temperature of the emitting layer (T), and then perform the usual operation:

$$CF_{\downarrow,LW} = F_{\downarrow,LW,measured} - F_{\downarrow,LW}^{clear} \quad . \tag{5.2}$$

We applied a methodology developed at ISAC-CNR (see Busetto et al., 2013) to parametrize the clear sky effective emissivity.

From radiosounding data acquired in the period 2005-2009, it has been observed (Tomasi et al., 2012) that atmospheric temperature profile at Dome C presents an inversion for most of the year: under such conditions the warmer air at the top of the inversion layer contributes more to the clear sky atmospheric longwave radiation at surface level than does the colder air near the ground (Gröbner et al., 2009). The inversion is about $20^oC$ during Antarctic Winter while during Antarctic Summer profiles are almost isothermal (Connolley, 1996). During Winter the top of the inversion layer in the lower troposphere is reached at a height of about 400 m above ground level. Therefore it has been decided to relate the clear sky emissivity to the temperature at 400 m ($T_{400}$). Under this assumption equation 5.1 becomes:

$$F_{\downarrow,LW}^{clear} = \epsilon(T_{400})\sigma T_{400}^4 \tag{5.3}$$

where a good correlation has been observed between $\epsilon(T_{400})$ and the measured $T_{400}$.

An issue is represented by the limited number of $T_{400}$ data: only one radiosounding per day is performed at Dome C, at 20:00 LST, so a correlation between $T_{400}$ and $T_g$ has been investigated to relate the emissivity to the available 1-minute measurements of ground temperature. In such a way equation 5.3 becomes:

$$F_{\downarrow,LW}^{clear} = \epsilon(T_{400})\left(\frac{T_{400}}{T_g}\right)^4 \sigma T_g^4 \quad . \tag{5.4}$$

The relation between $T_{400}$ and $T_g$ has been empirically determined for data acquired at 20:00 pm, differentiating cases with and without inversion:

$$T_{400} = \begin{cases} 168 + 0.31T_g & if \quad T_g \leq 244K \\ T_g & if \quad T_g > 244K \end{cases} \tag{5.5}$$

Since $F_{\downarrow,LW}$, and hence $\epsilon(T_{400})$ and $T_{400}$, does not show the same daily cycle of $T_g$, equation 5.5 has to be corrected for the $T_g$ daily cycle, represented by a cosine function:

$$T_{400} = f(T_g(t) - A_d[(cos(\omega_d t + \phi_d) - cos(\omega_d t^{RDS} + \phi_d)]) \tag{5.6}$$

where $t$ is the fraction of the day expressed in hours and $t^{RDS}$ is the radiosounding launch time, and the function $f$ is given by equation 5.5; the amplitude $A_d$ assumes higher values in Summer months and zero values in Winter months to account for the more or less accentuated diurnal cycle of $T_g$.

Using the calculated $T_{400}$ a linear relationship between $\epsilon(T_{400})$ and $T_{400}$ has been derived:

$$\epsilon_m(T_{400}) = -1.41 + 0.0077T_{400} \tag{5.7}$$

Evaluating $\epsilon_m$ as $F_{\downarrow,LW}\ \sigma^{-1}\ T_{400}^{-1}$ and comparing these values with the emissivity calculated with equation 5.7, we have observed a difference between them that follows a cosinusoidal annual trend during the period considered. This trend has been introduced into equation 5.7, so that the final form of $\epsilon(T_{400})$ is:

$$\epsilon_m(T_{400}) = -1.41 + 0.0077T_{400} - A_y cos(\omega_y d + \phi_y) \tag{5.8}$$

where $d$ is the day of the year.

In order to obtain longwave downwelling irradiance as a function of $T_g$ we use equations 5.8 and 5.6 in equation 5.4.

### 5.1.1 Application to our dataset

To verify if the parametrization worked on a dataset different from the one on which it has been tested, we calculated the clear sky irradiance $F_{\downarrow,LW}^{clear}$ with equation 5.4 and computed the differences $F_{\downarrow,LW,measured}^{clear}$ - $F_{\downarrow,LW,param}^{clear}$, where clear measurements are selected using Long and Ackermann's method. The frequency histograms of these differences are shown in the first plot of figure 5.1 and are divided by year to check if any trend is present; yearly mean and standard deviations of the distributions are displayed in the second plot. Data from the period 2008/2011 are shifted towards lower values of the differences compared to 2012/2015 values. This fact clearly appears looking at the mean values in the lower plot: the 2012/2015 averages are almost three times the 2008 one, and twice the 2009 one.

In figure 5.2 the scatter plot between measured (with 2012/13 data corrected) and parametrized irradiance is showed: red points represent clear sky longwave

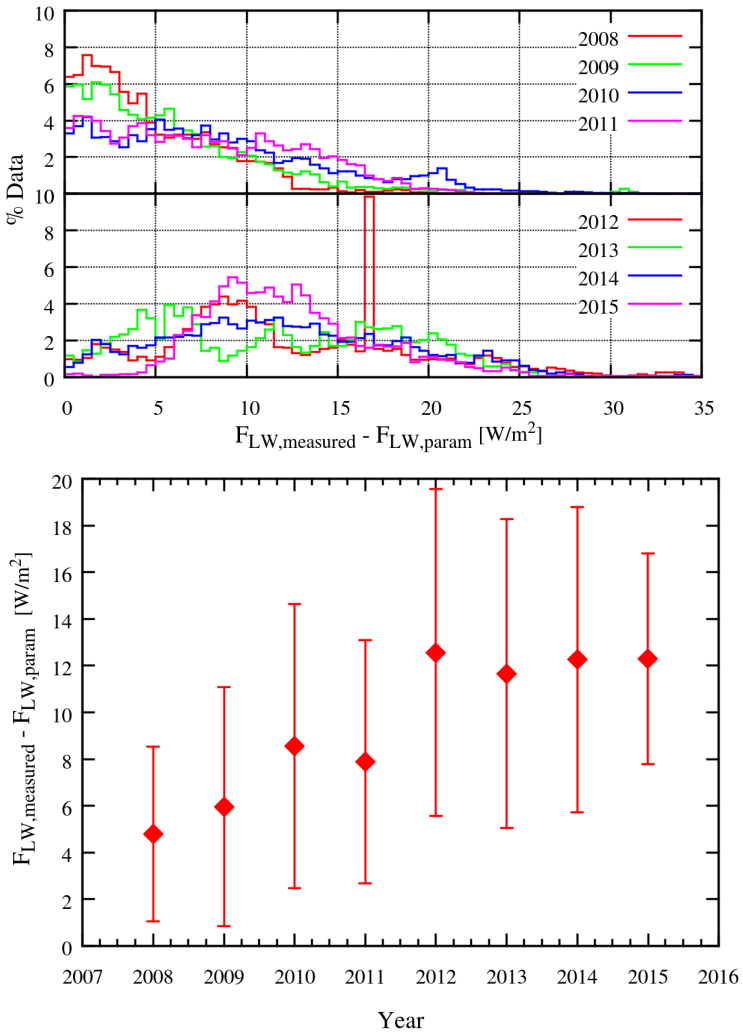


Figure 5.1: Upper plot: frequency histograms of the differences between measured and parametrized longwave downwelling irradiance, divided by year. Lower plot: temporal trend of yearly average and standard deviations of the previous distributions.

downwelling irradiance data, the black line is the bisector and the blue line is the linear correlation between x and y. The x-cut at 60 W/m$^2$ is due to the initial BSRN quality check on longwave irradiance data. It is evident that the parametrization strongly underestimates higher irradiance values (namely higher than 100 W/m$^2$), whereas it works better for lower irradiance values.

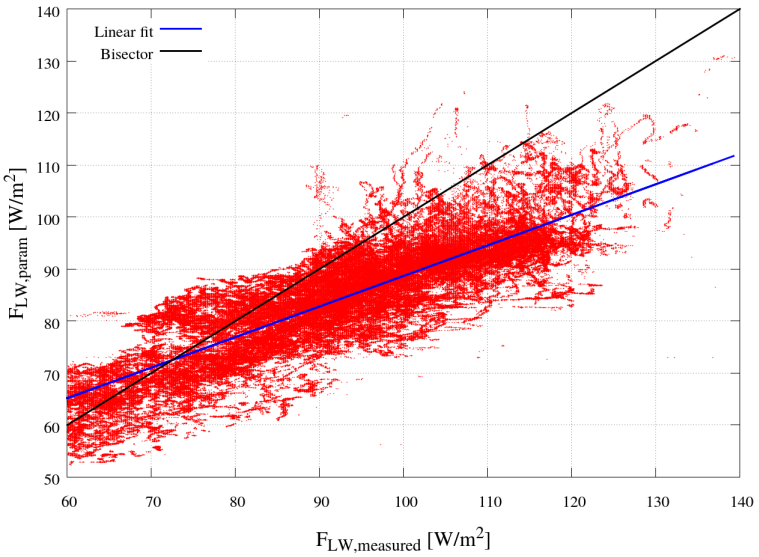


Figure 5.2: Scatter plot between measured and parametrized longwave irradiance (red points), with the bisector (black line) and the linear correlation between x and y (blue line), of equation $y = 0.6x + 30$.

All the constants that appear in equations 5.5, 5.6 and 5.8 have been obtained empirically analyzing 2006/09 data. It is possible that the comparison between $T_g$ and $T_{400}$ for a different period (2007/15) produces a slightly change in coefficients in formula 5.5 and 5.6. So a revised form of parametrization 5.4 is required. The issue is that radiosounding measurements are not available for 2007/15 period. Therefore we adopted an a posteriori correction based on the linear fitting showed in figure 5.2.

The equation of the linear fit of figure 5.2 is (blue line)

$$F^{clear}_{\downarrow,LW,param} = 0.6 F^{clear}_{\downarrow,LW,measured} + 30 \quad . \tag{5.9}$$

We want the new linear fit to be the bisector, hence we define $\hat{F}^{clear}_{\downarrow,LW,param}$ in a way that it equals the measured clear sky longwave irradiance:

$$\hat{F}^{clear}_{\downarrow,LW,param} = \frac{F^{clear}_{\downarrow,LW,param} - 30}{0.6} \quad . \tag{5.10}$$

We used this corrected formula to recalculate the parametrized irradiance for Summer season data from period 2012/2015. We recalculated the model errors,

and we show the results in terms of frequency histograms and averages in figure 5.3: histograms are shifted towards lower values compared to the ones in figure 5.1, and the averages are reduced of about 4 W/m$^2$, becoming comparable with the ones obtained for previous years.

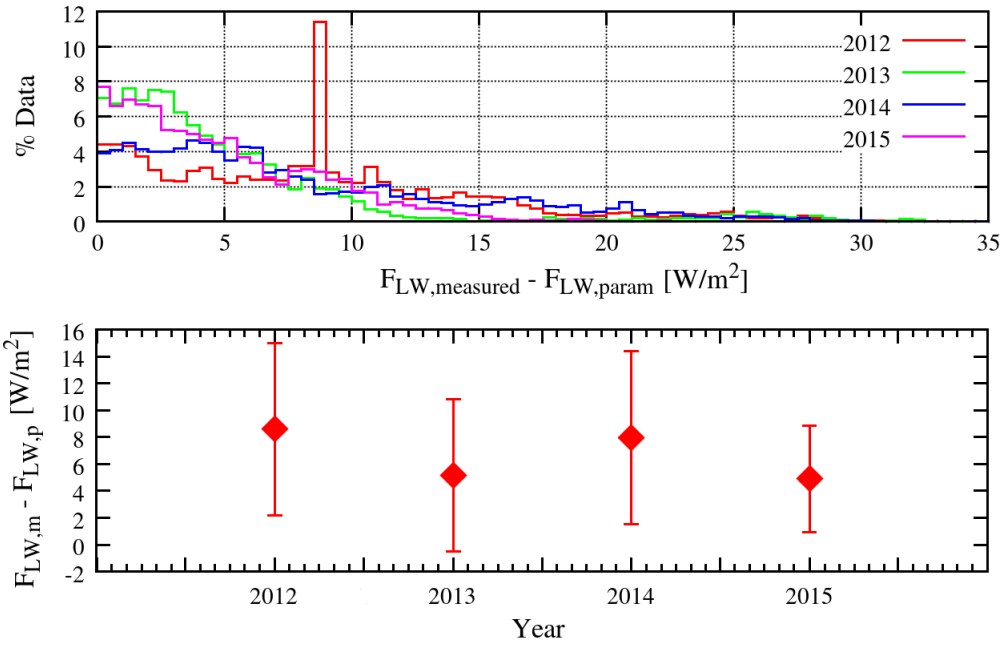


Figure 5.3: Upper plot: frequency histograms of the differences between measured and parametrized (with correction) longwave downwelling irradiance, divided by year. Lower plot: temporal trend of yearly average and standard deviations of the previous distributions.

### 5.1.2 Cloud forcing evaluation

In order to estimate the cloud focing using equation 5.2, we have to evaluate the clear sky irradiance that would be measured by the instruments during a cloudy day, i.e. $F^{clear}_{\downarrow,LW}$. Since the formula expresses the longwave irradiance as a function of temperature we need to know how it would behave in case of clear sky.

### Clear sky identification

Town et al. (2007) developed a methodology to identify clear-sky data based on downwelling indfrared irradiance measurements (hereafter referred to as the scatter plot method). It analyses the scatter plot of the longwave irradiance standard deviation calculated over a 20-minute time interval vs the longwave irradiance itself centered on the same interval; the 20-minute interval is chosen because it is an acceptable compromise between temporal resolution and a meaningful standard deviation. The application of this method requires the determination of a suitable clear sky longwave irradiance limit and associated standard deviation tresholds. For the standard deviation we used the value 0.8 according do Town et al. (2007), while as montly longwave tresholds we used the ones found in Busetto et al. (2013), that were obtained with SBDART (Santa Barbara Discrete Ordinate Radiative Transfer Atmospheric Radiative Transfer) code (Ricchiazzi et al., 1997). In figure 5.4 the January scatter plot is illustrated as an example. The vertical and horizontal lines represent respectively the standard deviation and longwave irradiance tresholds and divide the plot in four quadrants: quadrant I contains all clear-sky measurements (low irradiance and low standard deviation), while higher irradiances are associated to overcast conditions (quadrants III and IV); the standard deviation treshold prevents thin clouds from being classified as clear sky (quadrant II).

This procedure has been applied to the whole dataset in order to distinguish between cloudless and cloudy cases, for both daytime and nighttime.

### Clear-sky temperature computation

As already mentioned, to parametrize the clear sky longwave irradiance during a cloudy day, we need to know how the temperature at 400 m ($T_{400}$) would have been if the day wasn't cloudy ($T_{400}^{clear}$). Using equations 5.5 and 5.6 we can evaluate $T_{400}$ only when $T_g$ is measured. To fill the missing data we took advantage of the fact that $T_{400}$ (temperature at the top of the inversion layer) does not present an accentuated diurnal cycle, as already explained: this fact allows us to linearly interpolate two consecutive values of $T_{400}$ to obtain $T_{400}^{clear}$ for the whole dataset.

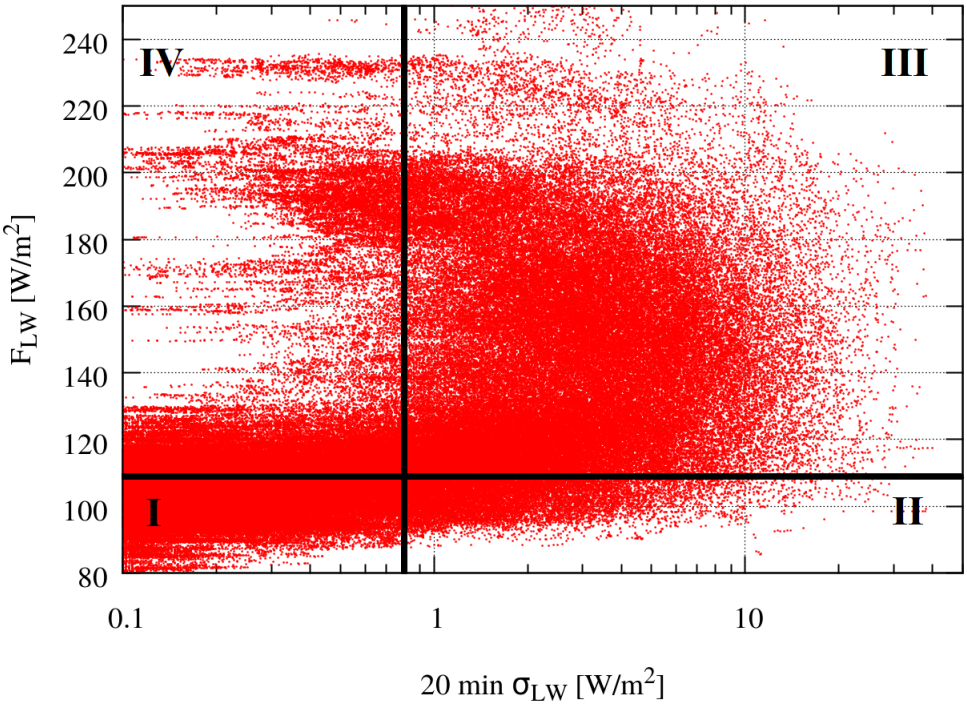


Figure 5.4: Scatter plot of the longwave irradiance standard deviation calculated over a 20-minute time interval vs the longwave irradiance itself centered on the same interval, for January data. The x axis is logarithmic. The vertical and horizontal thick lines represent the standard deviation and irradiance treshold for discriminating between cloudless and cloudy measurements: here they were taken as 0.8 and 109, according to Busetto et al., 2013.

### Cloud forcing calculation

We computed the longwave downwelling clear-sky irradiance $F_{LW}^{clear}$ with equation 5.4, using the interpolated values of $T_{400}^{clear}$ for the cloudy days. For the Summer season data (November, December, January, February) from year 2012 onwards we used the corrected formula 5.10 for the reasons above mentioned. We don't calculate the corrected parametrization for other months' measurements of the same years, because the clear sky longwave irradiance diminishes as temperature falls down with the approaching of Winter season, so that the

underestimation observed for higher irradiance data does not affect the them.

The monthly averages of cloud forcing are showed for all the years in our dataset, along with the climatological mean. All the values are positive, as expected, and fall between 5 W/m$^2$ and 40 W/m$^2$, excepted for the February 2008 value of -5 W/m$^2$. The climatological mean presents a peak of 27 W/m$^2$ in August and two relative maxima of about 20 W/m$^2$ in January and May.

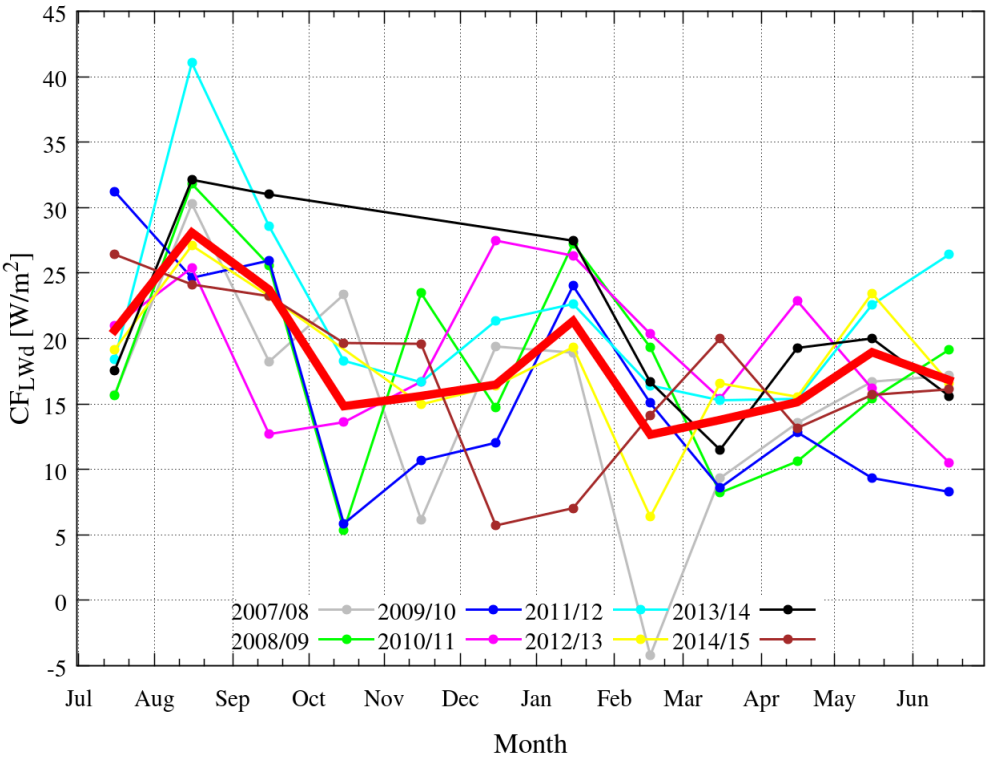


Figure 5.5: Monthly averages of cloud forcing on longwave downwelling irradiance for all the years from 2007 to 2015. The thick red curve is the climatological average.

## 5.2 Upwelling irradiance parametrization

The upwelling irradiance is that emitted by the snow surface. It is given by the formula:

$$F^{clear}_{\uparrow,LW} = \epsilon_{snow}\sigma T^4_{skin} + (1-\epsilon_{snow})F^{clear}_{\downarrow,LW} \tag{5.11}$$

where $T_{skin}$ is the temperature of the snow surface and $\epsilon_{snow}$=0.97 is the emissivity of the snow in the infrared (IR) (King et al., 2007). The second term in the equation takes into account the atmospheric longwave reflected irradiance.

The issue is that we do not have available the snow skin temperature data, but only the temperature of the atmopshere at the ground level $T_g$. Therefore we compared ground temperature and skin temperature (obtained inverting equation 5.11) data for the clear sky days as detected using the scatter plot method described above. During summer $T^{clear}_{skin}$ presents a more accentuated diurnal cycle than $T^{clear}_{g}$, but this differences shoud reduce using daily average values ($\overline{T}^{clear}_{g}$ and $\overline{T}^{clear}_{skin}$). In figure 5.6 these differences are shown: in the upper plot the time series of $\overline{T}^{clear}_{g}$ and $\overline{T}^{clear}_{skin}$ are displayed, in the lower plot the quantity $\overline{\Delta T}^{clear}$=$\overline{T}^{clear}_{g}$-$\overline{T}^{clear}_{skin}$. A slight rise is observed from 2011 (probably related to the increase in summer longwave downwelling irradiance discussed in chapter 2), along with a better defined yearly cycle, with minima occurring in Summer and maxima in Winter. The value of $\overline{\Delta T}^{clear}$ averaged on the entire period is (3.04 $\pm$ 3.60)$^o$C. Using the error propagation formula on equation 5.11 we estimated that an error of 3$^o$C on $T_g$ produces an error $\Delta F_{\uparrow,LW}$=11.5$\sigma T^3_g$ W/m$^2$ on the longwave upwelling irradiance, i.e. 7 W/m$^2$ for $T_g$=-50$^o$C (yearly mean temperature value), that is comparable with instrumental errors. Furthermore, we evaluated the linear correlation coefficient between the skin and ground temperature, and found it to be equal to 0.97: the best linear fit assumes the form $T^{clear}_{skin}$=0.01+1.04$T^{clear}_{g}$. Hence $T^{clear}_{g}$ has been considered a valid alternative to $T^{clear}_{skin}$ in the calculation of clear sky longwave upwelling irradiance.

To obtain $T^{clear}_{g}$ in cloudy cases we employed the interpolated values of $T^{clear}_{400}$ (as obtained in section 5.1.2) and inverted equations 5.5 and 5.6. Then the clear sky longwave upwelling irradiance was obtained from 5.11, and used to compute

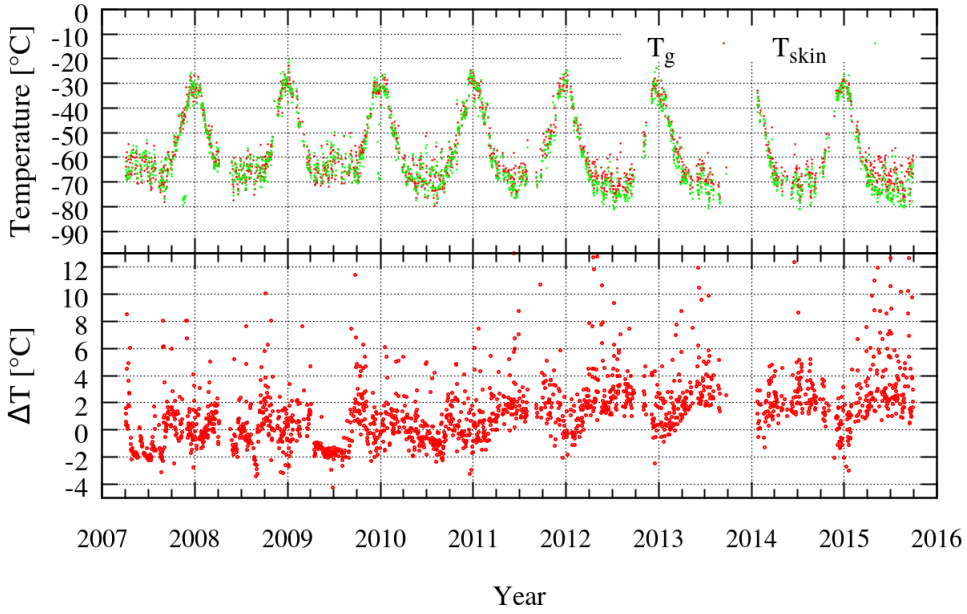


Figure 5.6: Top: time series of daily mean $T_g^{clear}$ (red) and $T_{skin}^{clear}$ (green). Bottom: time series of the daily averaged difference $\Delta T^{clear}$=$T_g^{clear}$-$T_{skin}^{clear}$.

the cloud forcing:

$$CF_{\uparrow,LW} = F_{\uparrow,LW,measured} - F_{\uparrow,LW}^{clear} \quad . \tag{5.12}$$

The monthly averages of cloud forcing are showed for all the years in our dataset, along with the climatological mean in figure 5.7. The climatological average falls between 0 W/m$^2$ and 5 W/m$^2$, except for August: it is lower in magnitude than the effect on the downwelling component, meaning that snow surface emissivity does not vary as much as atmospheric emissivity passing from cloudless to cloudy conditions. The overall effect on irradiance is expected to be positive: in fact snow warming and cooling are principally due to absorption of longwave atmospheric irradiance, so the cloud effect on upwelling component should reflect the downwelling component one. Anyway, looking at monthly averages from the different years, a significative number of data is found to be negative, or near zero. This can be a consequence of the errors committed in the parametrization of the clear-sky upwelling irradiance using $T_g$ rather than the exact $T_{skin}$.

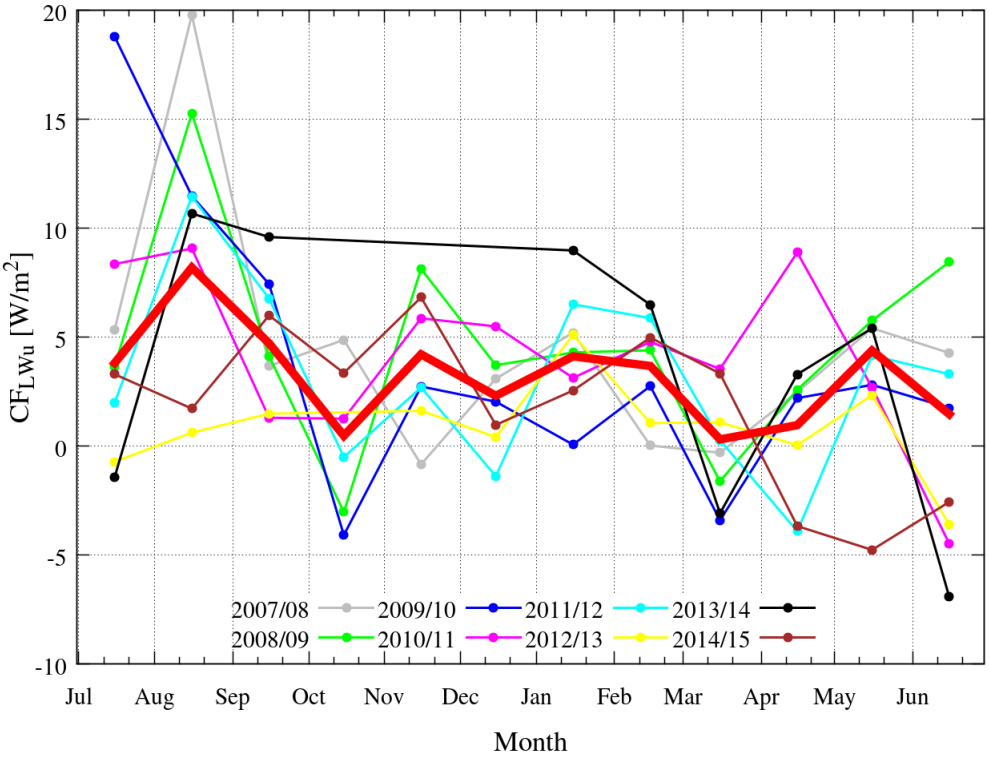


Figure 5.7: Monthly averages of cloud forcing on longwave upwelling irradiance for all the years from 2007 to 2015. The thick red curve is the climatological average.

# Chapter 6

# Final results

Different studies were performed in the Antarctic continent in the past in order to compute the cloud radiative forcing. Since the majority of the stations are located on the coast of the continent, less results representative of the Plateau are available in literature.

In Vitale et al. (2004) four year of broadband radiation measurements were examined in order to estimate how cloud radiative forcing depends on cloud coverage and cloud type characteristics at Terra Nova Bay (TNB) during the summer season: large interannual variability both in cloudy amount and cloud type is observed, mainly as a consequence of high variability of the surface characteristics during the Summer season, and a negative cloud effect on radiation (cooling of the planetary boundary layer during).

In Nardino et al. (2002) surface radiation measurements for Antarctic Summer 2000/2001 were analyzed at Terra Nova bay, in order to calculate the average cloud radiative forcing, that is found to be equal to -45 $W/m^2$ (i.e. clouds cool surface).

In Lanconelli et al. (2007) a comparison between cloudiness characteristics of two Antarctic sites, Terra Nova Bay from 1999 to 2007, and Dome C (DC) from 2006 to 2007, is carried out for Summer months only, analysing shortwave radiation flux measurements: at TNB the cooling effect of clouds ranges between -40 $W/m^2$ and -110 $W/m^2$, being positive cloud effect confined in less than 1% of the cases; ad DC radiative effects are much less intense, not being stronger of -20 $W/m^2$, and

positive effects represent a consistent part of the histogram distribution. Lower variability of cloudiness conditions is found at DC with respect to TNB.

In Town et al. (2005) a study of spectral and broadbad longwave downwelling radiative fluxes is carried out for year 2001 at South Pole station, in order to determine cloud radiative forcing and fractional cloud cover. Main outcomes show that during summer clear-sky fluxes are in the range 110-125 W/m$^2$ and 60-80 W/m$^2$ during winter, and depend on temperature, on the strenght of the surface-based temperature inversion, humidity and the presence of diamond dust (i.e. near-surface ice crystals). The annual mean longwave downwelling cloud radiative forcing is about 23 W/m$^2$ with no apparent seasonal cycle, and its low value (compared to the global mean one) is attributed to small optical depths and low temperatures of Antarctic clouds.

Yamanouchi et al. (2007) estimated the radiation budget at BSRN Syowa station, on the Antarctic coast, for a 13 years period (from 1991 to 2004). Absolute amounts of cloud effect were discussed. Net shortwave, net longwave and net total cloud forcing were -32.1 $\pm$ 8.9, 34.3 $\pm$ 9.3 and -0.6 $\pm$ 9.4 W/m$^2$, respectively, in December and net longwave cloud forcing in June was 38.5 $\pm$ 11.1 W/m$^2$. Cloud radiative forcings at Syowa Station obtained for 1987/1988 (Yamanouchi and Charlock, 1995) were similar, net shortwave, net longwave and net total cloud forcing were -40.8, 43.6 and 2.8 W/m$^2$, respectively, in January and net longwave cloud forcing in July was 14.2 W/m$^2$. These values were close to the results at Reeves Neves (1200 m a.s.l.) reported by Pirazzini et al. (2000).

Pavolonis and Key (2003) have shown, using satellite data, that clouds have a warming influence on the surface over the continent in all months. Over the ocean, clouds only had a warming effect from March to October, whereas during the Antarctic summer, cloud cooled the surface. Similar results were found by Fitzpatrick and Warren (2007) using measurements made on the RSV Aurora Australis.

An attempt to give a climatological characterization of clouds at a Polar site is found in Dong et al. (2010): radiation data collected at Barrow (Alaska) from June 1998 to May 2008 were used. This site presents features similar to the

above-mentioned Antarctic ones, i.e. low temperatures and absolute humidity, large solar zenith angles, presence of highly reflective snow-ice surfaces, persistend temperature inversions. The annual average of shortwave and longwave cloud forcing are opposite in sign and nearly cancel each other, resulting in an annual mean net cloud forcing of 3.5 W/m$^2$ (negative in Summer and positive in Winter).

## 6.1 Cloud radiative forcing at Dome C

Cloud radiative forcing has been estimated as:

$$CRF = CF_{\downarrow,SW} + CF_{\downarrow,LW} - CF_{\uparrow,SW} - CF_{\uparrow,LW} \tag{6.1}$$

where the various terms CF are the ones obtained in the prevoius three chapters.

A quality check procedure has been applied to $\mathrm{CF}_{\uparrow,SW}$ data calculated using the azimuth parametrization, since mid-season points are likely to be erroneous in some cases, as we have already pointed out in section 4.3. This quality check consisted in rejecting all albedo hourly mean data higher than 0.84 and in recalculating $\mathrm{CF}_{\uparrow,SW}$. This treshold is the average value of the albedo at Dome C for Summer months (see section 4.1), so it has been considered the most representative value for Summer months' albedo, i.e. the months where the shortwave irradiance contribution to forcing is most important.

Monthly means of CRFs were computed for the whole dataset. A second quality check has been performed in order to eliminate all data that were not statistically reliable: a minimum has been imposed to the number of hourly measurements-per-month on which the montly means are calculated; wheter this lower limit is not reached, the monthly mean value is rejected.

All these outcomes are shown in figure 6.1: the blue line and the red line are coincident, and represent monthly mean values filtered and not according to the latter procedure; the green line is the number of hourly measurements-per-month on which the monthly average has been computed. Note that the maximum possible number of hourly data-per-month is around 750 (24 hours x 31 days), and a consistent part of our available measurements fall significantly below this upper

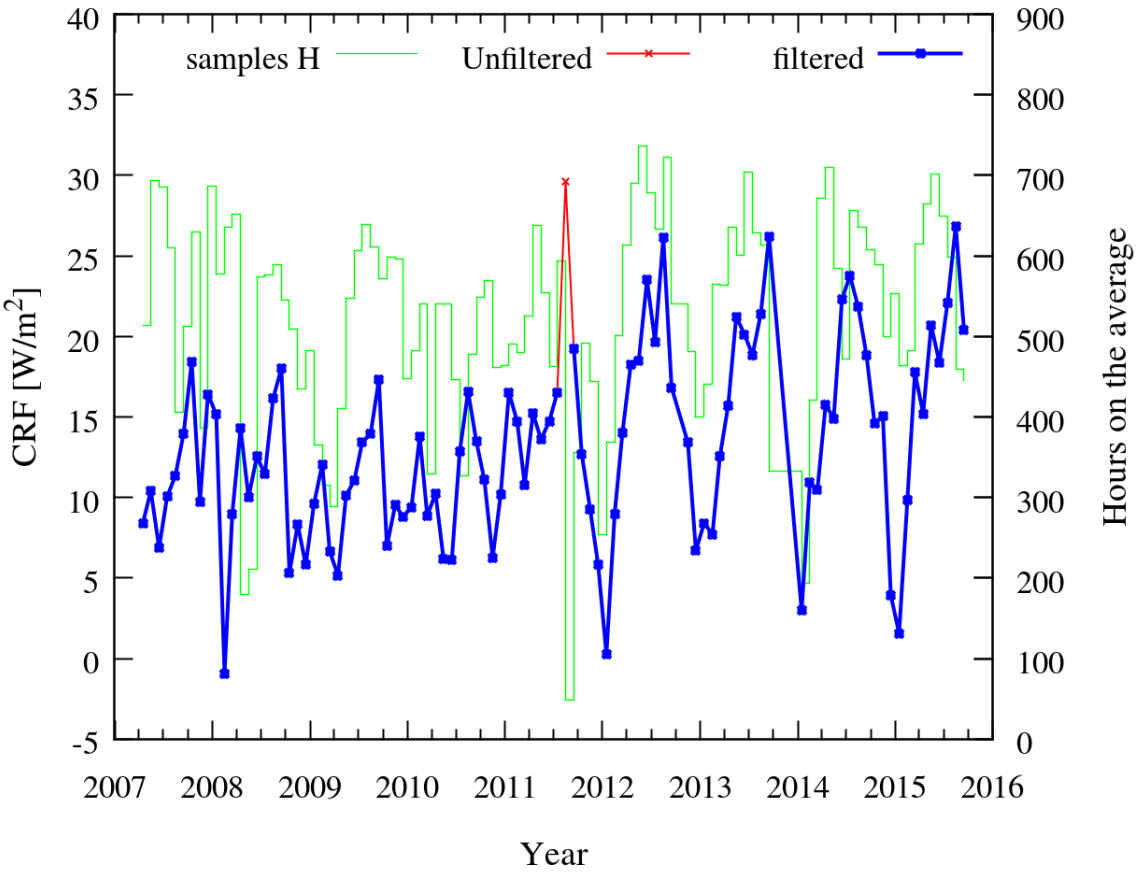


Figure 6.1: Montly mean CRF for the whole dataset, filtered and not according to the procedure explained in the text (blue and red lines), along with the number of hourly CRF data-per-month available (green line).

limit. Only one point from 2011 has been eliminated by our statistical quality check, that corresponded to the maximum monthly mean value obtained. Tipically lower CRFs are observed in summer months, when the negative contribution of the shortwave component is important. A more defined seasonal cycle become visible from 2012 onwards: higher positive peakes in Winter are probably due to the enhancement of the longwave downwelling irradiance that takes place in the last four years of the period (see section 2.3). Further analysis of atmospheric parameters should be perdormed in order to better understand this behaviour.

In figure 6.2 and table 6.1 the yearly averages of the CRF are shown, along

with their standard deviation. The averages have been computed weighting every monthly value on the number of hourly-measurements available. An upward trend is visible from 2011 onwards, but these values also presents the highest standard deviations.

| | Mean ± Std [W/m$^2$] |
|---|---|
| 2007 | 11.87 ± 3.57 |
| 2008 | 10.21 ± 5.14 |
| 2009 | 10.74 ± 3.29 |
| 2010 | 10.47 ± 3.19 |
| 2011 | 13.87 ± 3.58 |
| 2012 | 16.48 ± 7.20 |
| 2013 | 16.87 ± 5.93 |
| 2014 | 15.45 ± 6.42 |
| 2015 | 17.23 ± 7.01 |

Table 6.1: Yearly average and standard deviation (shaded area) of CRF.

The total average value of the CRF at Dome C for the period April 2007/September 2015 has been found to be:

$$13.70 \pm 2.90 \text{ W/m}^2$$

and its positive value accounts for an overall heating effect of clouds at the surface, according to other studies performed in areas climatological comparable with Dome C.

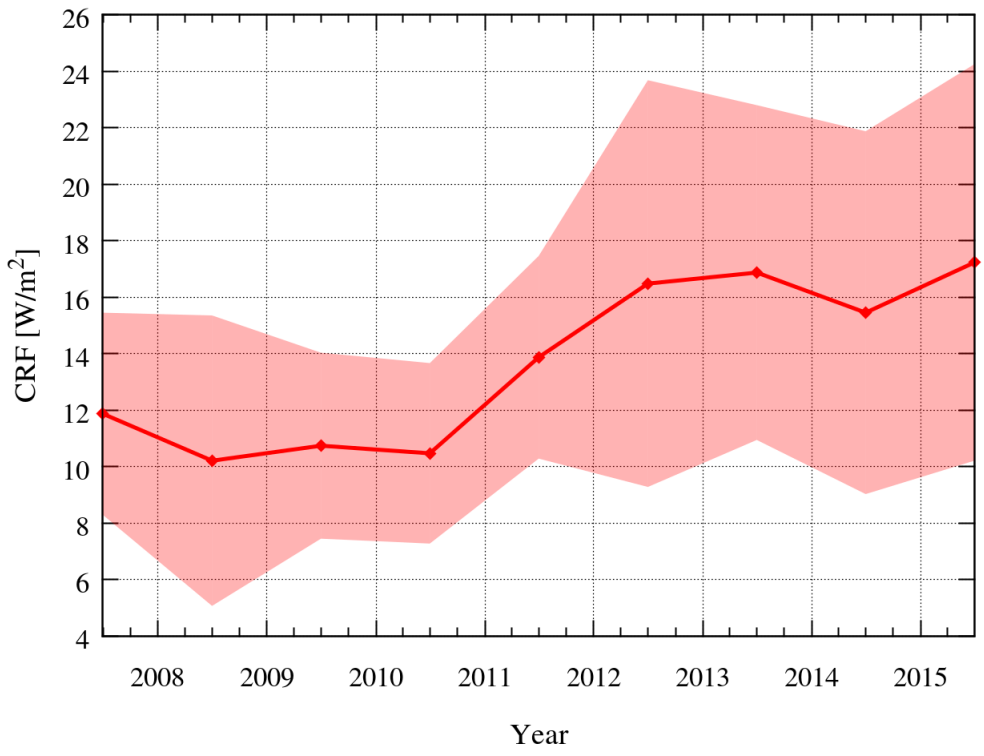


Figure 6.2: Yearly average and standard deviation (shaded area) of CRF.

# Conclusions

The aim of the thesis is to quantify the effect of the clouds on the radiation budget (namely the Cloud Radiative Forcing, CRF) at Dome C, area that is considered representative of the climatic conditions of the East Antarctic Plateau.

A 9-years dataset of broadband radiation measurements recorded at Italian-French station Concordia (BSRN network) has been analysed in order to obtain suitable parametrizations of the four components of irradiance in clear-sky conditions. Different metodologies have been used and developed to reach this goal. The observation of a pronounced diurnal asymmetry in surface broadband albedo during most of the measurement period has required the elaboration of a new model for representing it. A net positive cloud effect has been estimated, with an interannual upward trend and a reinforcement of seasonal oscillations in the last 4 years. The overall average value has been evaluated to be $13.70 \pm 2.90$ $W/m^2$ accordingly to other (few) similar estimations found in literature.

The peculiarity of this work is that it is only based on radiation data, so that every quantity obtained doesn't require the knowledge of additional informations. Considering the harsh conditions of the area that do not alwas allow an accurate measure of atmospheric parameters (such as temperature and humidity profiles), the methodology proposed can be an useful and simple tool to calculate the CRF. Some adjustements are still needed though, in particular for the treatement of low sun elevation data; furthermore, a comparison with other cloud detection methods should be performed for a better tuning of the parametric representations of cloud-free reference.

# Bibliography

[Brock and Richardson, 2001] Brock, F. V. and Richardson, S. J. (2001). *Meteorological measurement systems*. Oxford University Press.

[Busetto et al., 2013] Busetto, M., Lanconelli, C., Mazzola, M., Lupi, A., Petkov, B., Vitale, V., Tomasi, C., Grigioni, P., and Pellegrini, A. (2013). Parameterization of clear sky effective emissivity under surface-based temperature inversion at dome c and south pole, antarctica. *Antarctic Science*, 25(05):697–710.

[Carroll and Fitch, 1981] Carroll, J. J. and Fitch, B. W. (1981). Effects of solar elevation and cloudiness on snow albedo at the south pole. *Journal of Geophysical Research: Oceans*, 86(C6):5271–5276.

[Connolley, 1996] Connolley, W. (1996). The antarctic temperature inversion. *International Journal of Climatology*, 16(12):1333–1342.

[Dong et al., 2010] Dong, X., Xi, B., Crosby, K., Long, C. N., Stone, R. S., and Shupe, M. D. (2010). A 10 year climatology of arctic cloud fraction and radiative forcing at barrow, alaska. *Journal of Geophysical Research: Atmospheres*, 115(D17):n/a–n/a. D17212.

[Dutton et al., 1991] Dutton, E. G., Stone, R. S., Nelson, D. W., and Mendonca, B. G. (1991). Recent interannual variations in solar radiation, cloudiness, and surface temperature at the south pole. *Journal of climate*, 4(8):848–858.

[Fitzpatrick and Warren, 2005] Fitzpatrick, M. F. and Warren, S. G. (2005). Transmission of solar radiation by clouds over snow and ice surfaces. part

ii: Cloud optical depth and shortwave radiative forcing from pyranometer measurements in the southern ocean. *Journal of climate*, 18(22):4637–4648.

[Hahn and Warren, 2003] Hahn, C. and Warren, S. (2003). Cloud climatology for land stations worldwide, 1971–1996. *Numerical Data Package NDP-026D, Carbon Dioxide Information Analysis Center, Department of Energy, Oak Ridge, TN*.

[Lachlan-Cope, 2010] Lachlan-Cope, T. (2010). Antarctic clouds. *Polar Research*, 29(2):150–158.

[Lanconelli et al., 2007] Lanconelli, Agnoletto, Busetto, Lupi, Mazzola, Petkov, Vitale, Nardino, Tomasi, and Georgiadis (2007). Estimation of fractional sky cover, cloud type and cloud forcing effects at mario zucchelli and concordia stations from broadband radiation measurements. *Italian research on Antarctic Atmosphere and SCAR workshop on oceanography*.

[Lanconelli et al., 2011] Lanconelli, C., Busetto, M., Dutton, E., König-Langlo, G., Maturilli, M., Sieger, R., Vitale, V., and Yamanouchi, T. (2011). Polar baseline surface radiation measurements during the international polar year 2007–2009. *Earth System Science Data*, 3(1):1–8.

[Long and Ackerman, 2000] Long, C. N. and Ackerman, T. P. (2000). Identification of clear skies from broadband pyranometer measurements and calculation of downwelling shortwave cloud effects. *Journal of Geophysical Research: Atmospheres*, 105(D12):15609–15626.

[Long and Dutton, 2010] Long, C. N. and Dutton, E. G. (2010). Bsrn global network recommended qc tests, v2. x.

[Long and Shi, 2008] Long, C. N. and Shi, Y. (2008). An automated quality assessment and control algorithm for surface radiation measurements. *The Open Atmospheric Science Journal*, 2(1).

[Nardino et al., 2002] Nardino, Lupi, Vitale, Georgiadis, Calzolari, Evangelisti, Tomasi, Bortoli, and Trivellone (2002). Cloud effects on the radiative balance terms at terra nova bay. *Italian research on Antarctic Atmosphere*.

[Ohmura et al., 1998] Ohmura, A., Gilgen, H., Hegner, H., Müller, G., Wild, M., Dutton, E. G., Forgan, B., Fröhlich, C., Philipona, R., Heimo, A., et al. (1998). Baseline surface radiation network (bsrn/wcrp): New precision radiometry for climate research. *Bulletin of the American Meteorological Society*, 79(10):2115–2136.

[Pavolonis and Key, 2003] Pavolonis, M. J. and Key, J. R. (2003). Antarctic cloud radiative forcing at the surface estimated from the avhrr polar pathfinder and isccp d1 datasets, 1985-93. *Journal of Applied Meteorology*, 42(6):827–840.

[Pirazzini, 2004] Pirazzini, R. (2004). Surface albedo measurements over antarctic sites in summer. *Journal of Geophysical Research: Atmospheres*, 109(D20).

[Pirazzini et al., 2000] Pirazzini, R., Argentini, S., Calzolari, F., Levizzani, V., Nardino, M., Orsini, A., Trivellone, G., and Georgiadis, T. (2000). Study of the cloud radiative forcing at two antarctic sites: Reeves neve and dome concordia. *CONFERENCE PROCEEDINGS-ITALIAN PHYSICAL SOCIETY*, 69:151–162.

[Ramanathan et al., 1989] Ramanathan, V., Cess, R., Harrison, E., Minnis, P., Barkstrom, B., Ahmad, E., and Hartmann, D. (1989). Cloud-radiative forcing and climate: Results from the earth radiation budget experiment. *Science*, 243(4887):57–63.

[Ricchiazzi and Gautier, 1997] Ricchiazzi, P. and Gautier, C. (1997). The effect of surface topography on the radiation environment of palmer station, antarctica. In *CONFERENCE ON ATMOSPHERIC RADIATION*, volume 9, pages 310–314. AMERICAN METEOROLOGICAL SOCIETY.

[Ricchiazzi et al., 1995] Ricchiazzi, P., Gautier, C., and Lubin, D. (1995). Cloud scattering optical depth and local surface albedo in the antarctic: Simultaneous retrieval using ground-based. *Journal of geophysical research*, 100(D10):21–091.

[Salby, 1996] Salby, M. L. (1996). *Fundamentals of Atmospheric Physics,*. Academic Press.

[Shupe and Intrieri, 2004] Shupe, M. D. and Intrieri, J. M. (2004). Cloud radiative forcing of the arctic surface: The influence of cloud properties, surface albedo, and solar zenith angle. *Journal of Climate*, 17(3):616–628.

[Stanhill and Cohen, 1997] Stanhill, G. and Cohen, S. (1997). Recent changes in solar irradiance in antarctica*. *Journal of Climate*, 10(8):2078–2086.

[Tomasi et al., 2012] Tomasi, C., Petkov, B. H., and Benedetti, E. (2012). Annual cycles of pressure, temperature, absolute humidity and precipitable water from the radiosoundings performed at dome c, antarctica, over the 2005–2009 period. *Antarctic Science*, 24(06):637–658.

[Town et al., 2005] Town, M. S., Walden, V. P., and Warren, S. G. (2005). Spectral and broadband longwave downwelling radiative fluxes, cloud radiative forcing, and fractional cloud cover over the south pole. *Journal of climate*, 18(20):4235–4252.

[Town et al., 2007] Town, M. S., Walden, V. P., and Warren, S. G. (2007). Cloud cover over the south pole from visual observations, satellite retrievals, and surface-based infrared radiation measurements. *Journal of Climate*, 20(3):544–559.

[Vignola et al., 2012] Vignola, F., Michalsky, J., and Stoffel, T. (2012). *Solar and infrared radiation measurements*. CRC Press.

[Vitale et al., 2004] Vitale, V., Lanconelli, C., Lupi, A., Nardino, M., and Georgiadis, T. (2004). Estimation of fractional sky cover, cloud type and cloud forcing effects at terra nova bay from broadband radiation measurements. *Italian research on Antarctic Atmosphere*.

[Yamanouchi and Charlock, 1995] Yamanouchi, T. and Charlock, T. P. (1995). Comparison of radiation budget at the toa and surface in the antarctic from erbe and ground surface measurements. *Journal of climate*, 8(12):3109–3120.

# Acknowledgements

Ringrazio innanzitutto Angelo, per il tempo che mi ha dedicato seguendomi assiduamente in questi mesi, Christian e Maurizio per il contributo fondamentale alla riuscita della tesi.

Ringrazio il prof. Tiziano Maestri per la revisione lavoro e i preziosi consigli che mi hanno permesso di migliorare i risultati.

Come non ringraziare Angelo e Rossana, che dopo tutto questo tempo ancora non si sono stancati di me: finalmente ce l'abbiamo fatta! Grazie anche ai miei brothers Giuseppe e Franzuppo e a tutti i familiari, in particolare zia Elena.

Infine un ringraziamento speciale va agli amici che in qualche modo hanno segnato questi anni: Pepi, Irena, Costi, Anto, Diego, Caco, Eleo, Giacomo, Davide, Carlo, Comma, Guido, Giorgio, Luca, Gio, Ali, Eli, Brigno, Agne, Benni, Smilly, Pippi, Christian, Mauri, Maggie, Nino, Ica, Ale, Mary, Mire, Mani, Vani, Vins, Alessia, Rossella, Stefano, Andrea, Sandra, Monica, Paola, Alessio, Trita, MaryC, Slemi, Vic, Antonella, Fabrizio e B.